MEASUREMENTS OF LOW ENERGY PROTONS IN A PULSATING AURORA

A

DISSERTATION

Presented to the Faculty of the

University of Alaska in Partial Fulfillment

of the Requirements

for the Degree of

DOCTOR OF PHILOSOPHY

by

Alan David Johnstone B. A. (Hons) M.Sc.

College, Alaska

May 1970

MEASUREMENTS OF LOW ENERGY PROTONS IN A PULSATING AURORA

APPROVED:

Gerald J. Romick

Wallace B. Mursray

Daniel Sings

T. Neil Davis

Chairman

Roger Sheridan

Department Head

APPROVED: _____ DATE: June 9, 1970

Dean of the College of Mathematics,
Physical Sciences and Engineering

_____

Vice President for Research and Advanced Study

PLEASE NOTE:

Some pages have indistinct print. Filmed as received.

UNIVERSITY MICROFILMS.

ABSTRACT

A Nike Tomahawk rocket carrying particle detectors was launched into a display of pulsating aurora in the recovery phase of a large auroral substorm. The proton energy spectrum between 3 kev and 30 kev was measured in greater detail than had been achieved before and it was found that the differential energy spectrum had the form AE^{-r} with r varying from 2.1 to 2.9. Above the atmosphere the pitch angle distribution was flat i.e. the greatest intensities were at pitch angles of 90°. Below an altitude of 200 kms the protons were scattered considerably in collisions with atmospheric molecules. Below 160 kms the pitch angle distribution was essentially isotropic. There were time variations in the proton count-rate too fast to be attributed to spatial variations in the proton flux when spreading of the beam by charge-exchange cycling is taken into account. The variations correlate with changes in the electron flux such that the proton spectrum softens and the electron spectrum hardens during the event. The precipitated flux of both electrons and protons increases. It is suggested that the effect is caused by the operation of a mechanism described by Swift which energizes electrons at the expense of ring current proton energy. This may be the reason that electron precipitated fluxes are greater than proton fluxes although the trapped proton energy is 2 to 3 times greater than the trapped electron energy. The electron energy flux was 10 times the proton energy flux with a total of more than 10 ergs cm^{-2} sec^{-1} being precipitated continuously. It is estimated that, during the substorm, nearly 10^{21} ergs were precipitated into the northern and southern auroral

zones. Comparing the data collected with known ring current morphology it is suggested that proton energy is being injected into the ring current in the tubes of force which connect to the substorm.

ACKNOWLEDGEMENTS

Every time a rocket is launched many people contribute to the success of the operation. The launch of this rocket depended more than usual on the goodwill and skill of the people involved. It was launched by Joint Task Force Eight under the command of Col. W. Ramsey of the U.S. Army. Especial thanks are due to Col. F. Holder who coordinated the effort at the launch site and to Mr. John Mester, Mr. Harold Zancanata and their colleagues from the Ballistic Research Laboratories who handled the telemetry reception and collected the data without a single blemish. The Sounding Rocket Branch of the Goddard Space Flight Center made a big contribution to the success of the project with their design, construction and testing of the payload and I would like to mention especially D. W. Andrews, J. Lipiner, R. Walker and O. Brack for the hard work they did under difficult conditions at a new launch site.

I would like to thank Mr. Lou Baim, not only for the considerable personal effort he put into the construction of the payload but also for his courage and initiative. At T-3 minutes the umbilical plug was accidentally knocked out of the rocket before the payload had been switched on. Mr. Baim immediately ran to the elevated launcher, climbed it, stood on the end and replaced the umbilical. If he had not done this the opportunity to launch the rocket would have been missed. I also thank Mr. Jim Parry and the machine shop, and Mr. Dick Siegrist and the electronics shop for aid in constructing the payload.

I am indebted to many of my colleagues at the Geophysical Institute who spent many weary nights in March 1969 operating the four ground stations, waiting for the weather to improve and the aurora to build up. Some of the data they collected has been used in this dissertation.

The chairman of my committee Dr. T. N. Davis played a major role in the execution of the work as well as providing me with complete support and encouragement throughout. He initiated the project and was responsible for the extablishment of the launch site near Fairbanks which enabled us to fire the rocket into a pulsating aurora. I have also been fortunate that the other members of my committee Dr. G. Romick, Professor W. Murcray and Professor D. W. Swift are experts in the three major facets of the work; the interaction of particles with the atmosphere, rocketry and plasma physics. I appreciate the support and encouragement of Dr. A. Opp, NASA Scientific Representative on the project and thank Mr. J. R. Holtz, NASA Explorers and Sounding Rockets Manager for permission to launch the rocket from the Fairbanks site.

I thank all those who have helped to produce this dissertation for their prompt and conscientious attention; Mrs. Helen Linde in the steno pool, Jim Strandberg and Hiroko Horiuchi in the drafting shop, the Photographic services and Russell Wertz for helping with data analysis.

Finally I apologize to my wife and family for leaving them to face the rigors of one of the coldest Alaskan winters while I worked on the payload in a warmer climate.

The rocket work performed here was supported by The National Aeronautics and Space Administration, Contract No. NSR-02-001-025.

Ground observations were supported by The Atmospheric Sciences Section National Science Foundation, NSF Grant Nos. GA-1514 and GA-11937.

TABLE OF CONTENTS

LIST OF ILLUSTRATIONS

LIST OF TABLES

CHAPTER 1

INTRODUCTION

The first evidence to show that auroras were caused by particle precipitation into the upper atmosphere was the observation of Doppler shifts in the hydrogen emission lines in the auroral spectrum (Gartlein 1950, Meinel 1951). The protons emitting the light were observed to be traveling towards the observer with velocities of the order of 5×10^7 cms sec^{-1}, equivalent to an energy of a few kiloelectron volts (kev). Some authors attempted to ascribe all auroral excitation to proton precipitation (Chamberlain. 1958) but without great success. The first measurements of auroral particles from rockets (McIlwain 1960) found that the dominant precipitating particles were electrons with energy between 1 kev and 10 kev, although it is not until recently that protons in the same energy range have been measured directly. After McIlwain's measurement, interest in auroral protons waned until it was shown by Evans et al (1966) from satellite measurements that, although peak electron fluxes were higher, the integrated energy flux from protons was a significant fraction of the total energy input to the atmosphere because the zone of proton precipitation was more extensive in latitude. Two other results obtained from satellites measurements have demonstrated the importance of protons in the physics of the magnetosphere. The solar wind protons carry 95% of the total energy in the solar wind, and second, within the magnetosphere the greatest reservoir of trapped particle energy is the ring current consisting mainly of 5-50 kev protons (Frank 1967). The electron trapped energy is less than half the proton energy.

Many workers have made measurements of high energy (E > 100 kev) protons in auroras from rockets since 1960 (Davis et al 1960, Mozer and Bruston 1966, Soraas and Trumpy 1966, Whalen et al 1967) but it is only recently that the low energy (E < 10 kev) protons have been measured. The measurements have been made in a prebreakup hydrogen arc (Chase 1968) and in post breakup aurora (Reasoner et al 1968, Bernstein et al 1969). All the rockets were launched from Fort Churchill in Canada at a geomagnetic latitude of 68.7°. The measurements reported here are the first made at a lower latitude and into pulsating aurora; also the measurements were made with greater spectral resolution.

All measurements made from spacecraft are very limited in spatial and temporal extent and can only be related to the large scale events statistically, as is done with satellite measurements, or by simultaneous observation from the ground of the extent and morphology of the precipitation. Recently Montbriand (1969) completed the first detailed study of the morphology of hydrogen emissions in the auroral substorm. A brief summary of his description of the proton substorm is as follows. Before the breakup hydrogen emissions are seen in a band along the auroral oval. In the evening sector the band is south of the oval,at midnight it crosses the oval and when it is seen in the morning it is north of the oval. The band is up to 8° wide and is narrowest in the evening midnight sector. After the breakup hydrogen emissions are seen everywhere in the polar bulge of the aurora but they are not seen in the westward traveling surge (Akasofu et al 1969). Montbriand (1969) also reports observing a patch of hydrogen aurora at the equatorward boundary break away and drift westwards - the direction protons drift in the gradient of the magnetic field.

The situation as it appears today is somewhat paradoxical. Most of the energy is trapped as protons and precipitated as electrons. The data presented in this dissertation show one way the paradox may be resolved. The features of the precipitation indicate that a mechanism proposed by Swift (1968) which accelerates electrons at the expense of ring current proton energy, may be operating.

The measurements were made from a Nike Tomahawk rocket, payload NASA 18.15, which was launched from Chatanika,(geomagnetic latitude 65°, near Fairbanks Alaska, at 1238 UT on March 17th 1969.

At 12.10 UT there was a breakup almost in the zenith at College, Alaska. The region of precipitation spread rapidly north, east and west to cover the whole sky accessible to the network of all-sky cameras being operated (Figure 1.1). Hydrogen emissions were seen throughout this region. At the time the rocket was launched pulsating aurora were seen over most of the sky. The pulsating patches were generally small; their periods were usually less than one second and each event lasted only a few periods. The electron flux measurements made from the rocket show that many of the pulsations were nearly monoenergetic implying that resonant wave-particle interactions were responsible. The average precipitation remained uniform over the sky. To give some idea of the extent of the aurora in Figure 1.2 all-sky camera photographs taken almost simultaneously from the four ground stations at the time the rocket was at apogee are shown. Figure 1.3 shows the magnetometer records from College and Bar I, and Figure 1.4 show riometer records from College, Fort Yukon and Bar I.

The substorm occurred during the main phase of a small to moderate magnetic storm which began at 0030 UT on March 17, with a sudden commencement. The maximum depression of the Earth's equatorial magnetic field was 32 γ reached

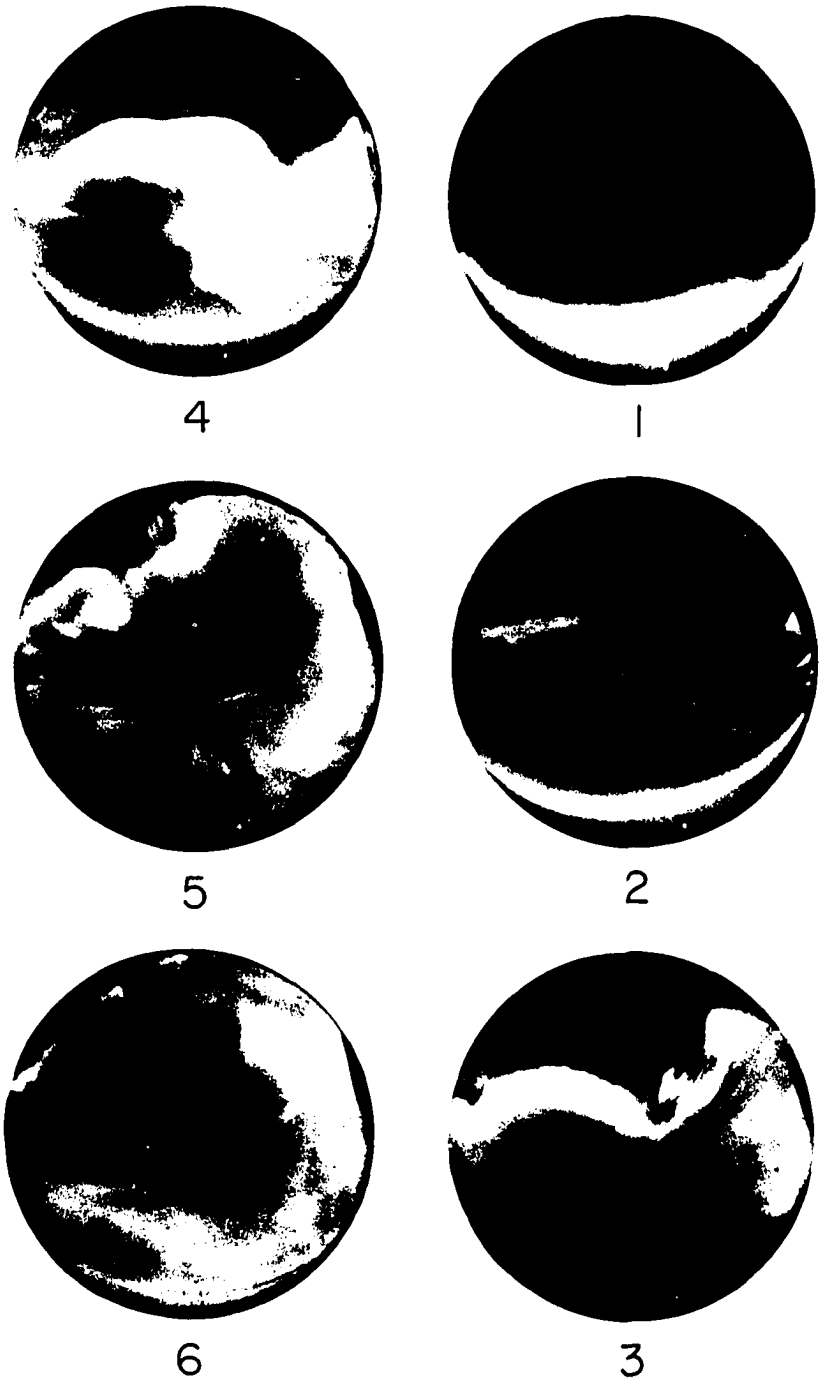

Figure 1.1 All-Sky camera photographs taken at 1 minute intervals from College during the auroral breakup and poleward expansion at 1210 U.T. March 17, 1969. The sequence is from 1 to 6.

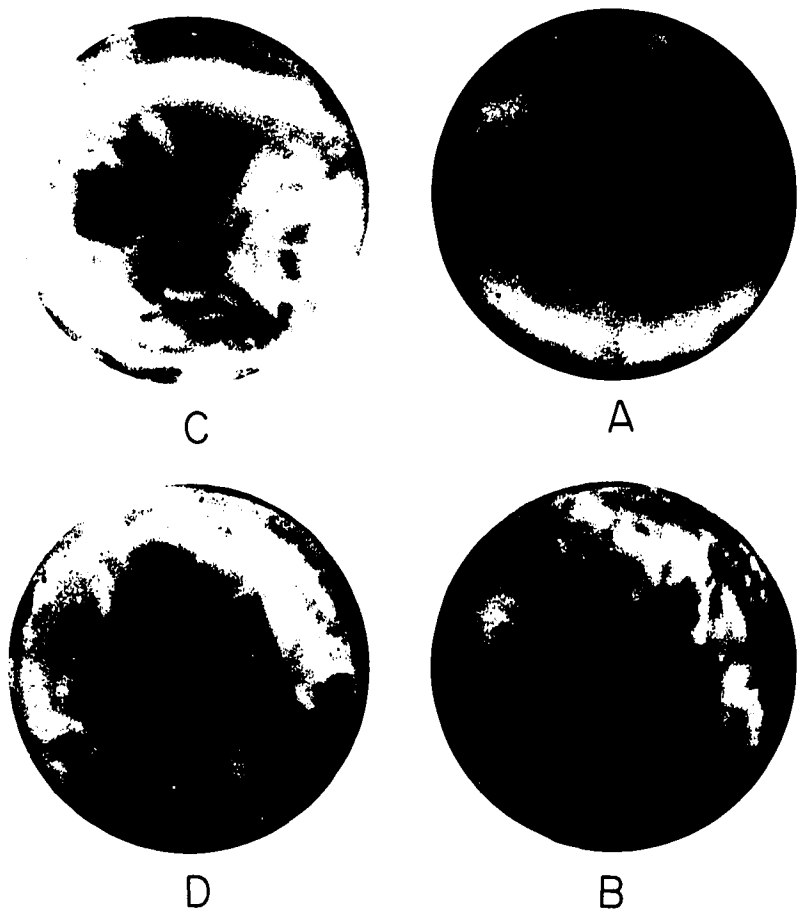

Figure 1.2 All-Sky camera photographs taken at 1242.00 U.T. from the four ground stations at Bettles, Fort Yukon, College and Tok. The map shows the location of all stations mentioned.

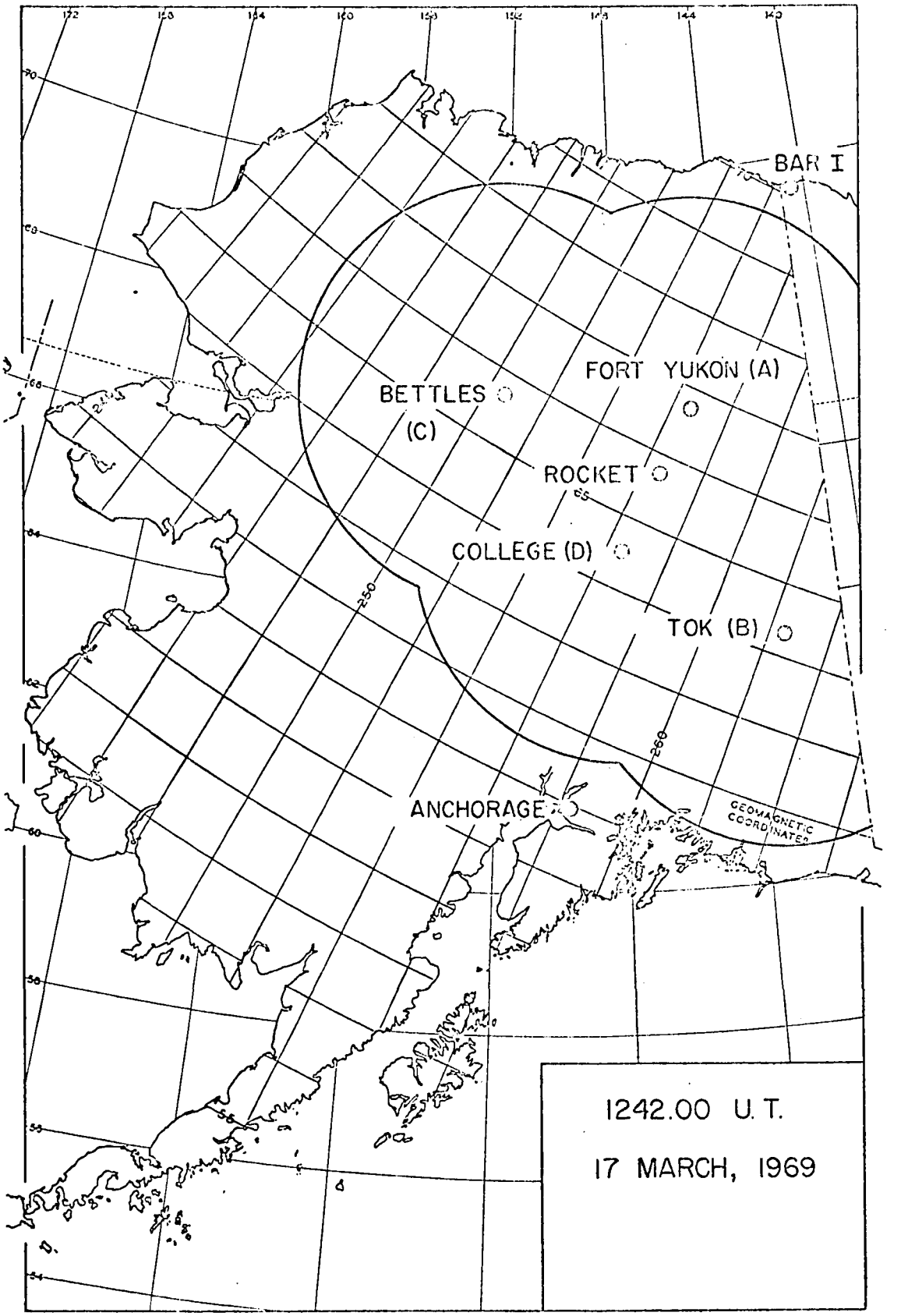

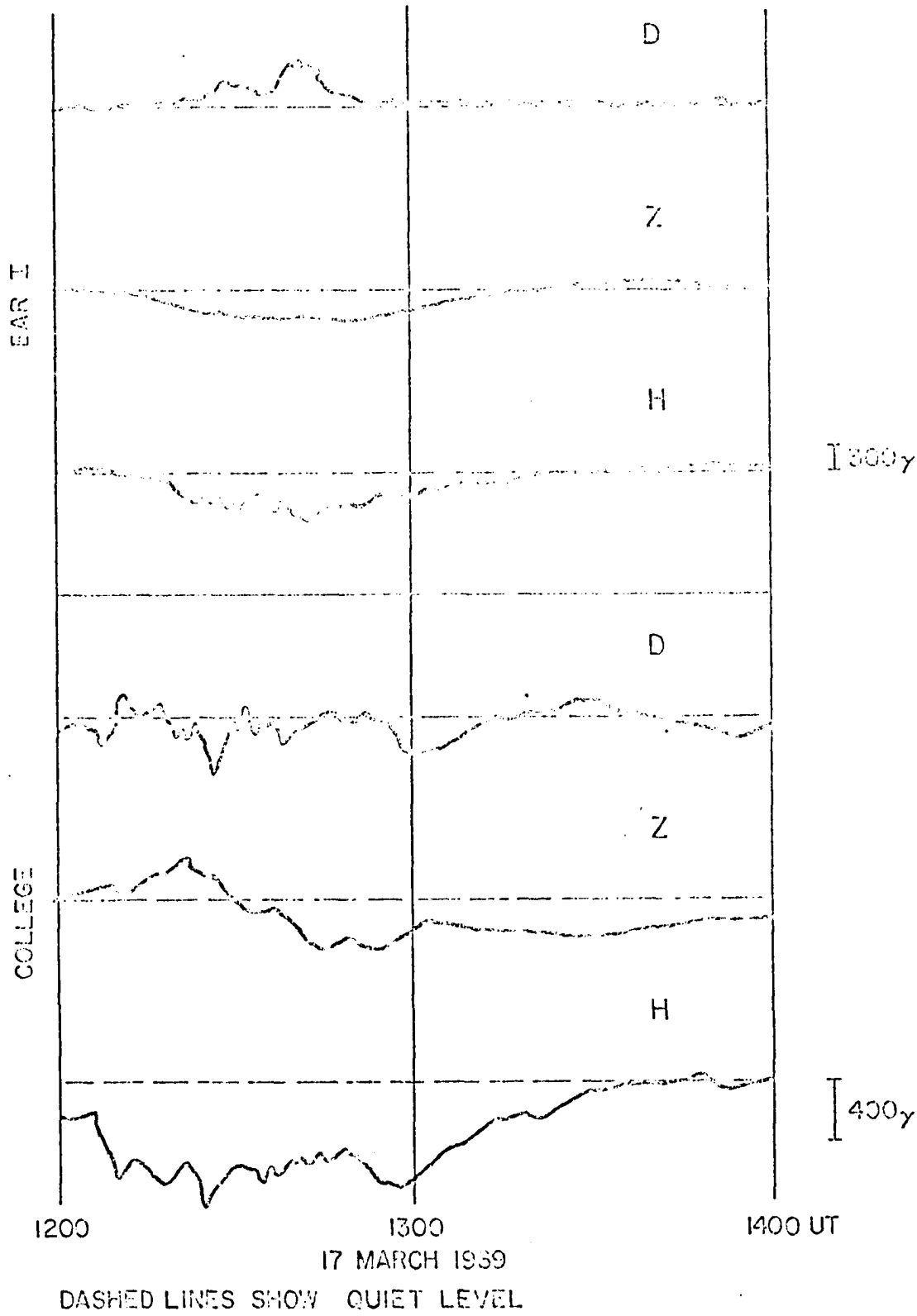

Figure 1.3 Three-component magnetograms from Bar I and College for the duration of the substorm.

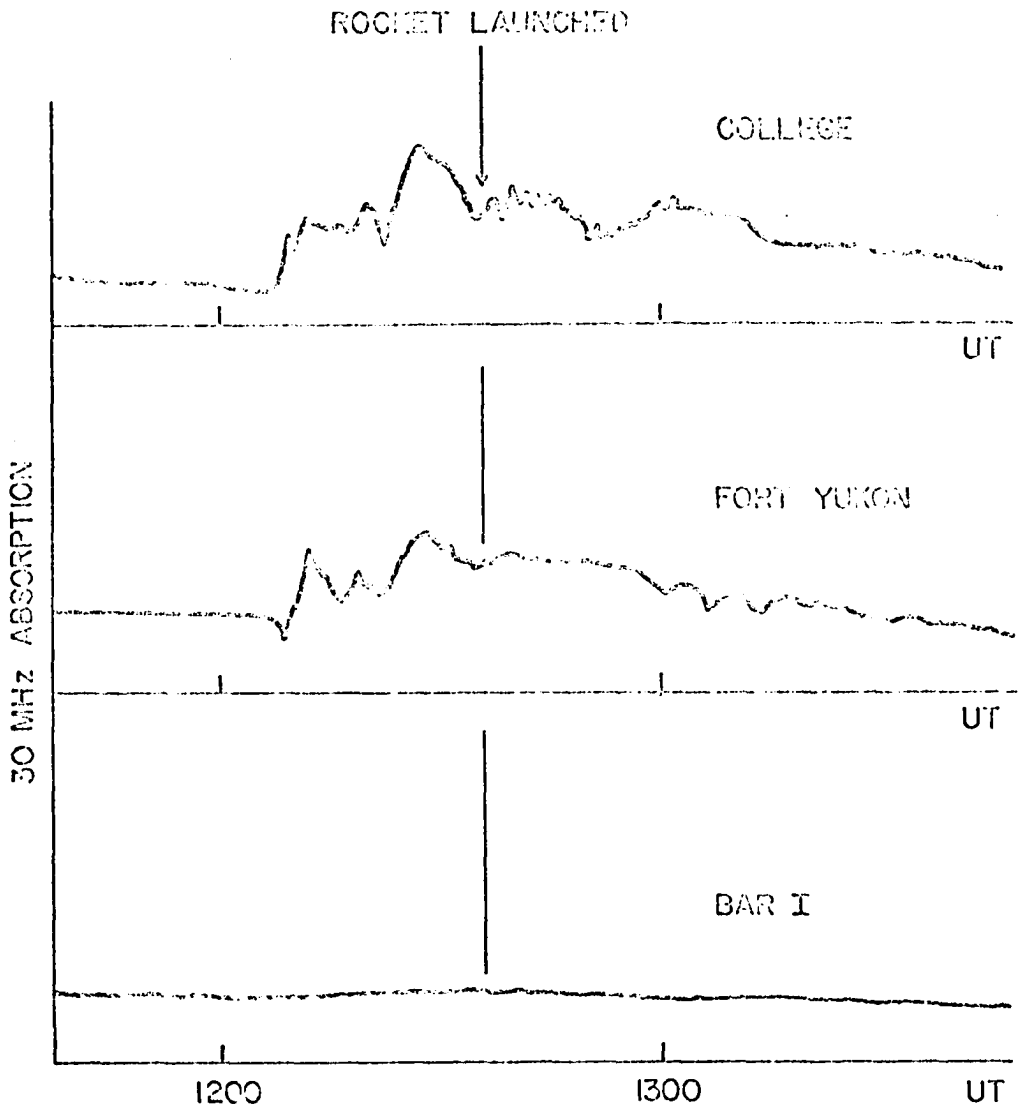

Figure 1.4 Absorption of cosmic noise measured by riometers at College, Fort Yukon and Bar I during the substorm.

between 0300 and 0900 UT (Fig. 6.2). A small substorm was observed in Alaska at 0915 UT with a maximum depression in the horizontal component of 150 γ. This substorm preceded the large one at 1210 UT which had a maximum horizontal magnetic depression of 840 γ.

The proton data were collected by one particle detector out of a total of eight in the payload. The detector was originally designed to detect electrons and therefore had a geometric factor that was really too small for counting protons. As a result the proton counting rates were always low. In fact, in all, some 8,850 protons were recorded. During the substorm approximately 10^{27} protons were precipitated over Alaska. It is pertinent to ask how representative of the total precipitation the observed particles were. The problem is akin to that faced by the political pollster who hopes that interviews with a few thousand people show the way tens of millions will vote. His method is to select them at random from the whole population. His techniques may be biased but he is able to sample every part of the country. The particle detector certainly selects randomly but only from a very restricted region in space-time. There is no way of knowing whether the measurements are representative of the whole proton population except from the optical measurements. The light intensity was fairly uniform along the magnetic meridian which indicates qualitatively that the proton precipitation did not change greatly. Although further investigations will probably uncover systematic variations with latitude and longitude, the measurements are likely to be typical of the region in which they were made.

In Chapter 2 the experimental techniques, the methods of analysis and the performance of the rocket are discussed in detail. In Chapters 3 and 4

the gross features of the proton beam, its spectrum and pitch angle distribution, are determined. Some special events during the flight in which proton fluxes correlate with electron fluxes are described in Chapter 5 and the precipitated energy is calculated in Chapter 6. Chapter 7 is concerned with the results of the study and their significance for optical measurements, a possible precipitation mechanism, and the relation of these measurements to the substorm.

CHAPTER 2

INSTRUMENTATION AND ROCKET PERFORMANCE

2.1 Design of the Particle Detectors

The basic sensitive element in each particle detector was a channel electron multiplier operated in the gain-saturated mode, (Adams and Manley 1966, Bryant and Johnstone 1965, Schmidt and Hendee 1966 and Evans 1965). In this mode an output pulse with height independent of particle energy is produced whenever an incident particle initiates an electron cascade in the tube. Channel multipliers are especially suitable for measurements of auroral particles because they have no entrance window to impede the low energy particles and the sensitive surface is stable enough to be exposed to the atmosphere for long periods of time without degradation. They have now been used many times in rockets and satellites. Energy discrimination in the detector was achieved with a cylindrical plate electrostatic analyzer in front of the channel multiplier. A diagram of a detector is shown in Figure 2.1, and the high voltage circuit is shown in Figure 2.2.

The main consideration in the high voltage circuit is to keep the noise level low. Any pulse at the anode of the channel multiplier greater than 10 mv will trigger a count. There are two main sources of noise, ripple in the applied voltage of 3600 v and high voltage noise. The ripple is easily reduced below 1 mv by the RC filter chain shown in Figure 2.2. It also prevents pulses from one multiplier coupling to another multiplier using the same high voltage source. High voltage noise is generated by the breakdown of insulation or by the formation of tracking paths across

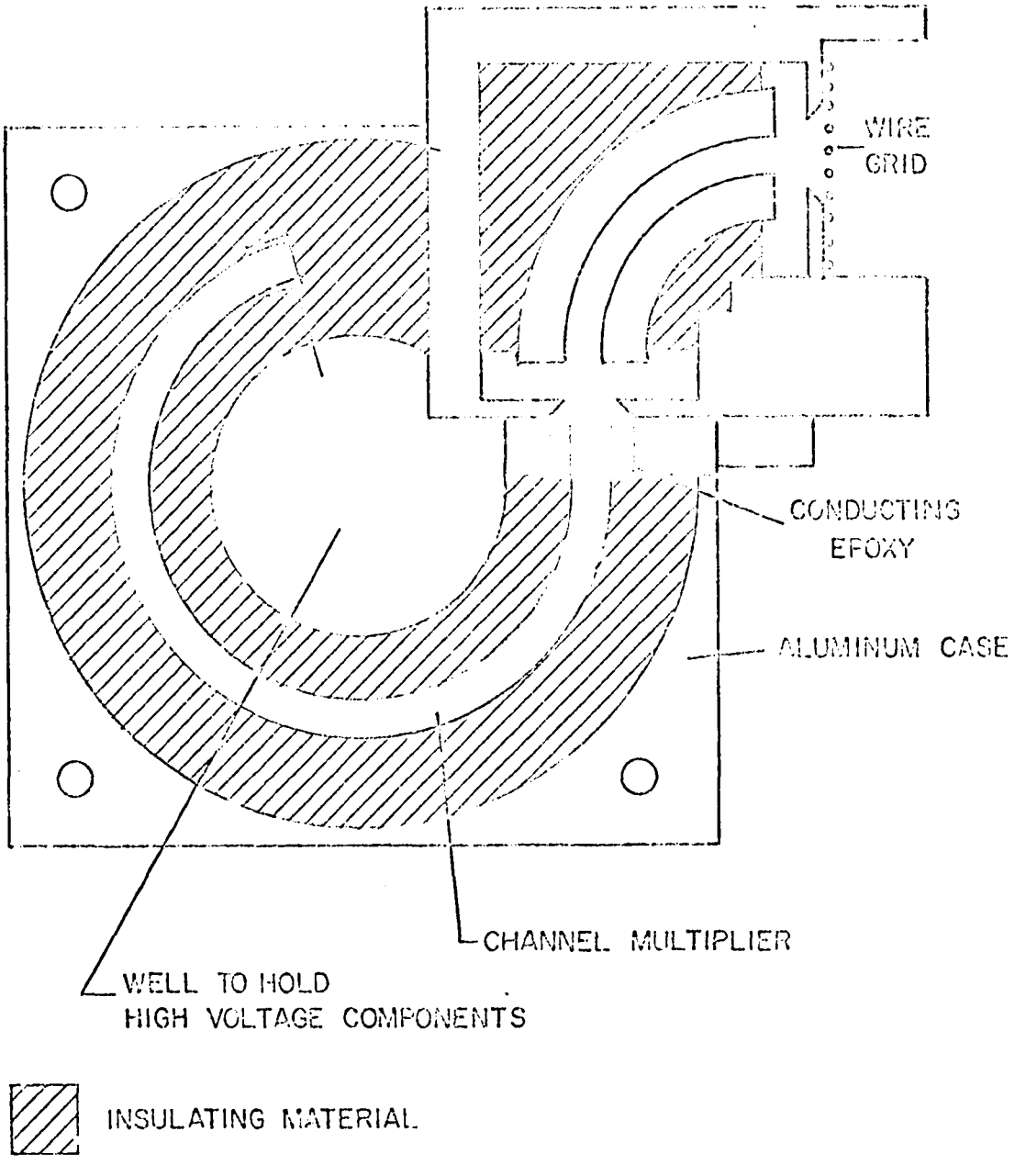

Figure 2.1 A sketch of the layout of the particle detector. High voltage components are encapsulated in the central well and the amplifier is mounted over the top of the channel multiplier. Wiring connections have been omitted for clarity.

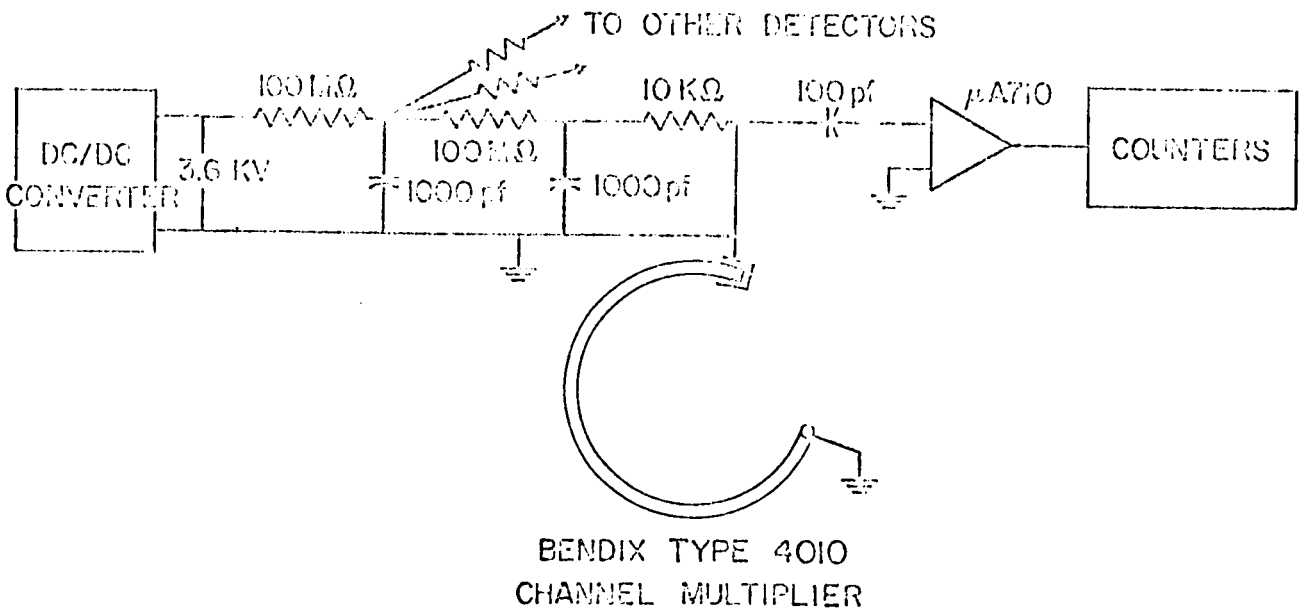

Figure 2.2 The high voltage circuit used to operate the channel multipliers. The R-C network is to reduce ripple from the DC/DC converter and decouple the detector outputs from each other. The output pulse length is controlled by the 10KΩ resistor and the amplifier is a

surfaces. To prevent both effects all the high voltage circuitry was encapsulated in an epoxy resin, Eccobond 45C, which is clear and flexible. It also served as a rigid mounting for the channel multiplier. The slight flexibility of the resin prevents thermal stresses from breaking the glass of the tube. It was the first time this method of mounting had been used. Other experimenters who have mounted tubes in epoxy used resins with coefficients of thermal expansion matched to that of the glass of the tube. The mounted tubes were cycled in temperature from -40°C to +70°C without showing any signs of damage. Before encapsulating the channel multiplier, the anode was sealed with conducting epoxy, Eccobond 57C, to form an electron collector. It was also used to fix the open end of the tube in place because if the entrance to the tube were surrounded by an insulating surface, charge would build up and deflect particles away. The signal was extracted through a 100 pf DC blocking condenser and amplified by a Fairchild μA 710 differential comparator integrated circuit. It produces an output pulse of 3 v for any input pulse greater than 10 mv. The output pulse height of a channel multiplier decreases with pulse rate (Schmidt and Hendee 1966, Adams and Manley 1966) so that to any discrimination level there corresponds a maximum counting rate. The maximum counting rate was near 5×10^5 counts/sec, well above the maximum capacity of the counting circuits.

There have been many investigations of the degradation of channel multiplier performance with use (Frank, Henderson, Swisher 1969, Reed et al. 1968, Klettke et al. 1969). After an initial "cleanup" period when the gain drops by 50% while 5×10^7 counts are accumulated, the gain remains constant until after 10^{10} counts have been accumulated. It then begins to decrease again. The channel multipliers used in a rocket experiment are unlikely to

register as many as 10^{10} counts so that this irrecoverable loss of gain is of no concern here. The initial "clean-up" period is important because it is observed whenever the tube has been exposed to the atmosphere. It has been attributed (Klettke et al.1969) to the adsorption of gas to the walls of the tube. The gas is released under bombardment by electrons during the normal operation of the tube. The effect was noted during laboratory tests on the channel multipliers. The pulse shape during the "clean-up" phase is long and ragged (Fig. 2.3) compared with a normal pulse. The shape is similar to that observed with straight channel multipliers where it is caused by positive ions generated by collisions between atmospheric molecules and the electron cascade and which move towards the cathode to start a new cascade. The effect was removed by curving the tube (Evans,1965). Ion after-pulsing has also been noticed by Wolber et al. (1969) in the "cleanup" phase of curved channel multipliers. The behavior of a channel multiplier in the cleanup phase is important because in flight the detector operates immediately after a long exposure to the atmosphere. There is reason to believe (section 2.9) that spurious data were generated in flight by ionic after-pulses.

All the calibration and testing of the channel multipliers was done in a vacuum system pumped by an oil diffusion pump. It has been reported that contamination from the organic compounds in vacuum oils, causes deterioration of the channel multiplier performance (Klettke et al. 1969). However, the contamination is not serious for short term use. To minimize the contamination an oil (Convalex 10) with a very low vapor pressure and high resistance to thermal decomposition was used in the pump.

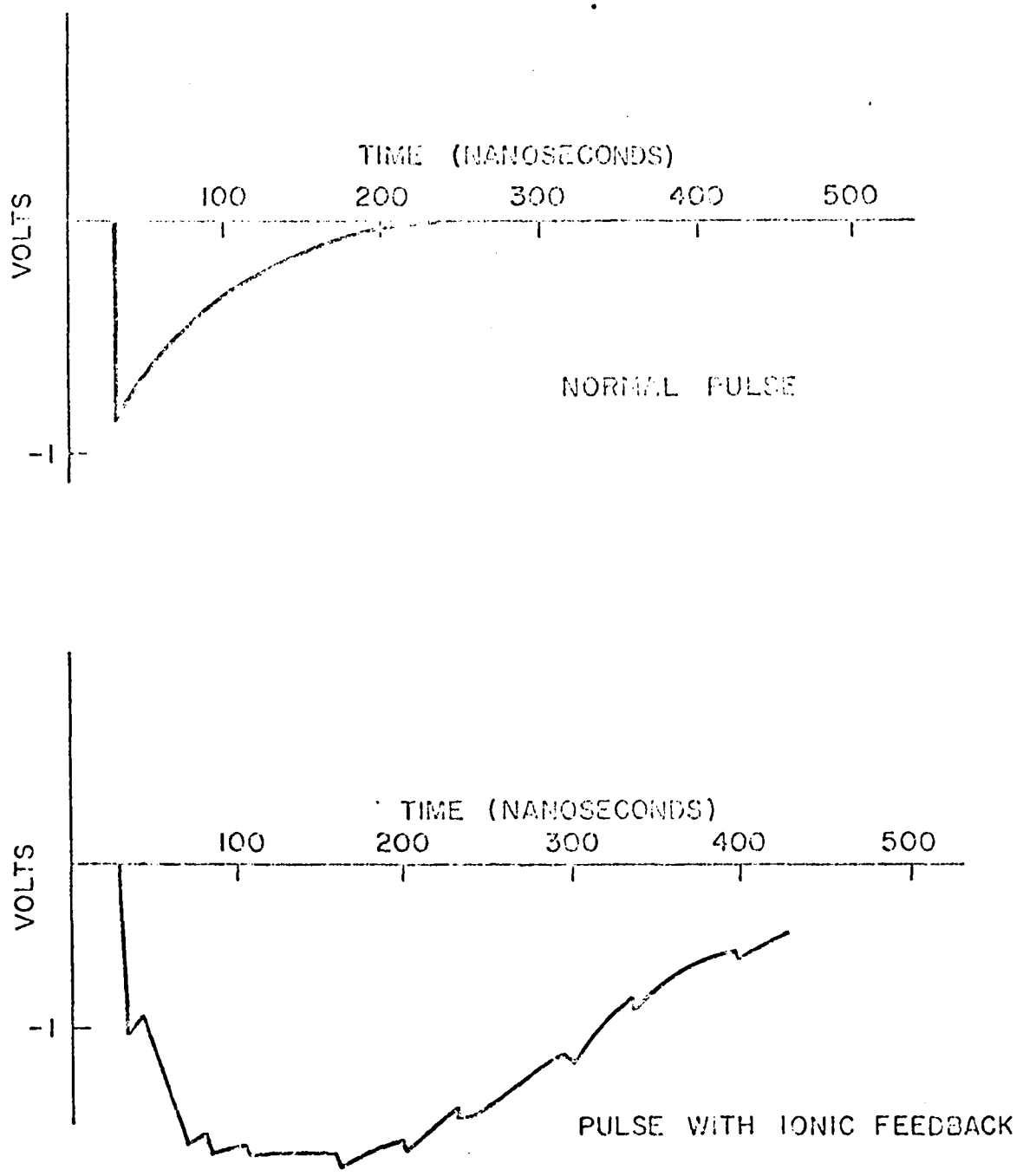

Figure 2.3 A comparison of output pulses from the channel multiplier. During the "cleanup" phase the pulse is long and ragged indicating ionic feedback. When the cleanup is complete a single short burst of electrons creates the pulse.

The design of the cylindrical analyzer is shown in Figure 2.1. The cylindrical plates are 0.075" apart, and the radius of the surface midway between the plates is 0.75". Equal voltages with opposite polarity are applied to the plates so that the midsurface remains at zero potential. Assuming the plate spacing d is small compared with the radius r of the midsurface, the condition for a particle to have a circular orbit in the analyzer is

$$\frac{mv^2}{r} = \frac{eV_d}{d} \quad \text{or} \quad V_p = V_d \frac{r}{2d} \qquad 2.1.1$$

v - particle velocity

V_p - particle kinetic energy in electronvolts

V_d - potential difference between analyzer plates

The analyzer of Figure 2.1 has its energy pass band centered at V_p, which is five times the applied voltage V_d.

The principal features of the analyzer design are as follows:

(a) There is no insulating surface exposed to the beam of particles so that it is not possible for charge to build up and modify the electric field in the analyzer.

(b) There is no collimation at the entrance because this would affect the accuracy of the calculation of the geometric factor of the analyzer. This point is discussed in detail in section 2.4. In order to prevent the electric field extending out through the wide entrance aperture the aperture was covered with a coarse wire mesh grounded to the frame.

(c) The cylindrical plates were made from magnesium, and the surfaces were sandblasted to reduce the effect of particles scattered from the

plates. It is not expected to be important in a proton detector, but, in an electron detector, scattered particles can make an important contribution to the total counting rate in some circumstances.

The energy of the passband of the proton detector and one of the electron detectors was varied continuously through the spectrum from 3 kev to 24 kev by varying the voltages applied to the cylindrical plates. The voltage wave-form is shown in Figure 2.4. It was monitored in flight to obtain correct timing for the particle spectra and as a measurement of the voltage on the analyzer plates.

The output pulses were counted by a 9 bit binary counter. After counting for 3 milliseconds the accumulated count was converted to a 5 bit number. The first 3 bits indicated the position of the first non-zero bit and the remaining two gave the value of the next two bits. A digital-to-analogue converter changed the 5-bit number to one of 32 analogue levels which was presented to the telemetry input for the 3 msec following the counting period. Meanwhile the counter reset and continued counting. The counts corresponding to the thirty-two levels are given in Table 2.1.

Once the maximum count has been accumulated in any 3 msec period it is held until the end of the period. The maximum counting rate is therefore

$$\frac{1000}{3} \times 448 \approx 149{,}000 \text{ counts per second.}$$

The features of the counting circuit are

(a) It has 3 msec time resolution

(b) It is compatible with IRIG Standard FM/FM telemetry although it requires a channel with a minimum bandwidth of 600 Hz.

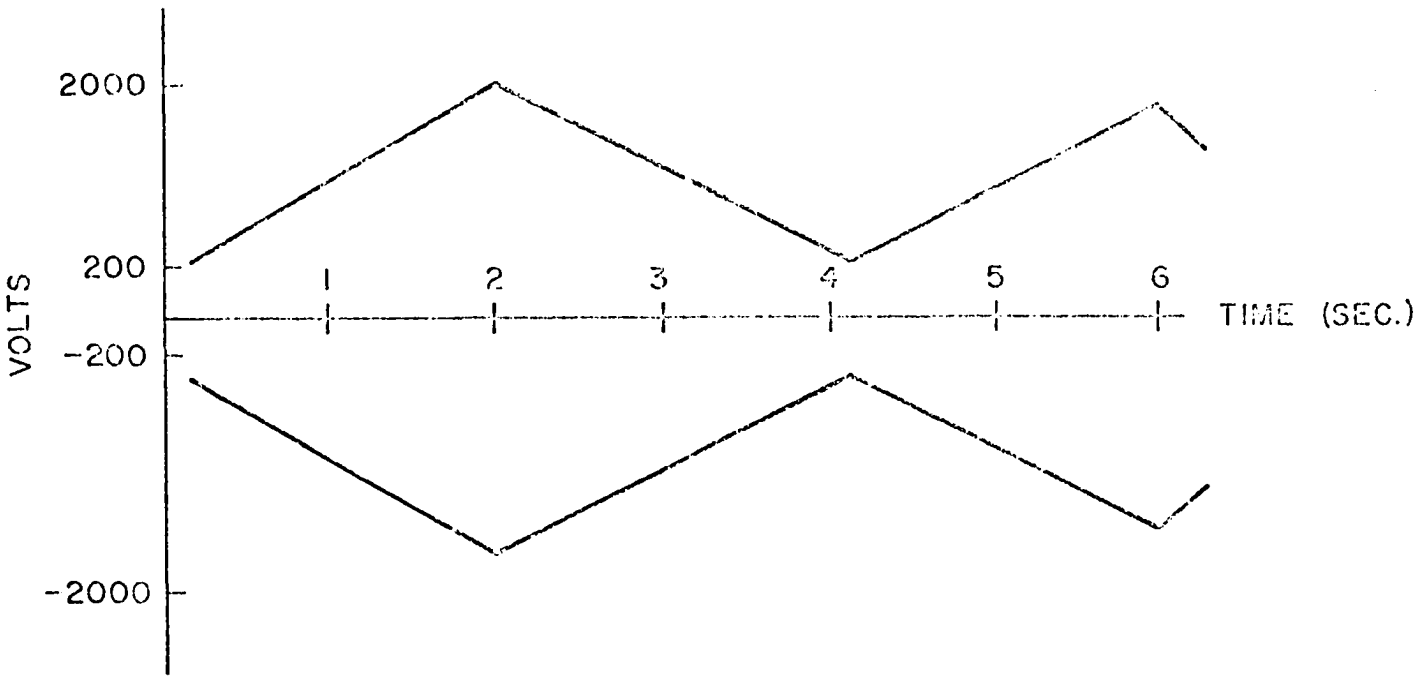

Figure 2.4 Output waveform of the swept high voltage power supply. There are two output lines, positive and negative, sweeping from 200 volts to 2000 volts nominally.

Table 2.1

Output Levels of the Counter

Level	Counts	Level	Counts	Level	Counts	Level	Counts
1	0	9	8	17	32	25	128
2	1	10	10	18	40	26	160
3	2	11	12	19	48	27	192
4	3	12	14	20	56	28	224
5	4	13	16	21	64	29	256
6	5	14	20	22	80	30	320
7	6	15	24	23	96	31	384
8	7	16	28	24	112	32	448

(c) It has a wide dynamic range for counting, from less than 1 cps to greater than 10^5 counts per sec.

(d) At high enough count rates the output is equivalent to that from a logarithmic count-rate meter but with a very fast time response. Quick look data are readily interpreted and interesting features can be analyzed with digital accuracy.

Every 60 seconds a calibration routine stepped the output through all the levels in 30 msec.

2.2 Testing and Calibration

All the tests and calibrations of both proton and electron detectors were done with an electron beam. It would have been better to have used a proton beam to calibrate the proton detectors but it was not possible in the time available. The electrons were obtained from a hot tungsten wire and accelerated through cylindrical electrodes. A collimator mounted on the anode of the electron gun produced a parallel beam of electrons approximately 0.25" in diameter. The beam current was constant over most of its cross section. The current intercepted by the collimator was monitored as an indication of beam current. At any fixed energy the current was proportional to the beam current. By maintaining the collimator current constant, the beam current could be kept steady. The detectors were mounted on a table that could be moved horizontally in two perpendicular directions from outside the vacuum chamber. The beam was fired vertically downwards into the detector aperture at normal incidence for all tests. The detector position was adjusted until it was in the uniform part of the beam.

The channel multipliers were subjected to the following tests:

(a) The maximum counting rate with the flight amplifier was measured. To pass the test a count rate of $2\ 10^5$ cps had to be achieved.

(b) The noise count rate had to be less than 1 count per sec.

(c) The detector was exposed to an intense beam which was then switched off. The subsequent count rate was observed in an attempt to detect after-pulsing which in some tubes has persisted for up to ten seconds. No after-pulsing was detected in any of the tubes. It could not have been detected on the very short time scale of after-pulsing occurring in the "cleanup" period: one or two microseconds.

(d) The counting rate of the detector in a set beam current was measured at three energies, 2 kev, 5 kev and 10 kev. This provided an approximate measurement of channel multiplier efficiency for electron detection at these energies.

The cylindrical analyzers were checked by measuring the detector counting rate as a function of beam energy for a normally incident beam. An identical voltage was applied to the plates of all the analyzers tested to give an intercalibration. The measurement does not give the geometric factor of the analyzer; this would require a much more extensive series of measurements. A typical curve is shown in Figure 2.5. The effect of electron scattering is indicated on the diagram. The proton scattering should be much less important.

After the detector package had been assembled it was tested again. The proton detector which now had the correct polarity voltage on its analyzer plates was tested by firing in a very intense beam of electrons. The detector did not respond at all, showing that it had a high degree of rejection to electrons.

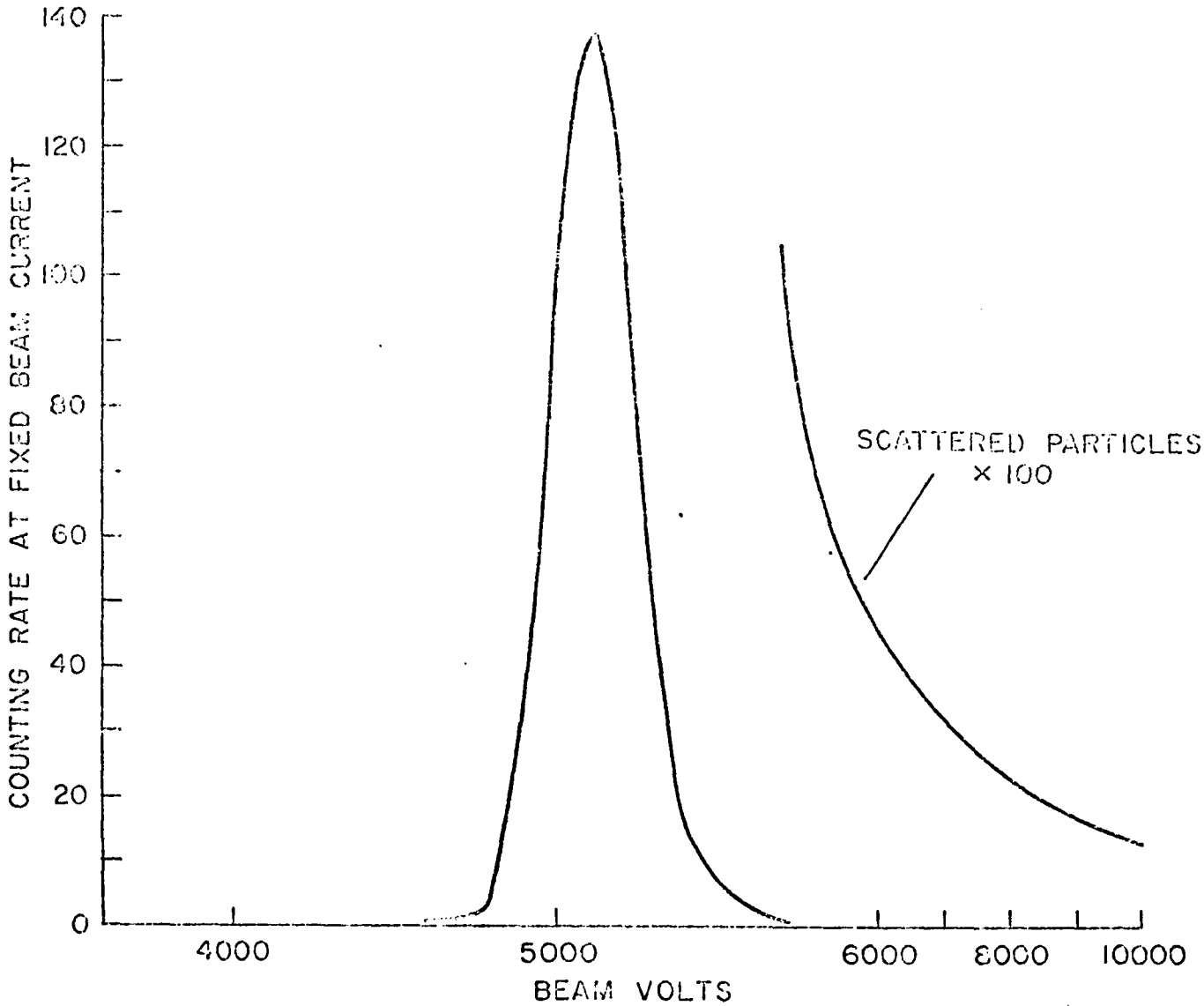

Figure 2.5 Experimental response curve of the detector to an electron beam of fixed current and varying energy at normal incidence. The contribution from scattered

In preflight tests the detector operation could not be checked directly. The high voltage was switched on and the counter output observed. A series of about 50 pulses in the second after switching on, followed by a very low noise level, was taken as indicating the detector was in a satisfactory condition. It is thought that the pulses originate in polarization currents in the high voltage capacitors. The existence of the pulses confirmed high voltage operation, circuit continuity and the operation of the counters.

2.3 Efficiency of Channel Multipliers

The efficiency of a channel multiplier is defined as the fraction

$$\epsilon = \frac{\text{output count rate}}{\text{number of particles incident per second}}$$

In general it is a function of particle species and energy. Since the detector response to protons was not measured, the value for the efficiency has been taken from published data. There is good agreement between different workers (Burrous et al. 1967, Sharber et al. 1968, Shea et al. 1967, and Tatry et al. 1969) that above 3 kev the efficiency for protons is independent of energy and lies between 60% and 80%. The data are plotted in Figure 2.6. In calculations in this work the value of ϵ is 0.70. There is less agreement on the efficiency for counting electrons. The data for electrons are given in Figure 2.7 (Frank, 1965, Bosqued, 1967 and Egidi et al. 1969). The selected average values used here are also indicated. The data of Egidi et al. (1969) have been treated as a measurement of relative rather than absolute efficiency. Absolute measurements have been made on similar channel multipliers since the flight reported here and are in agreement with the values selected.

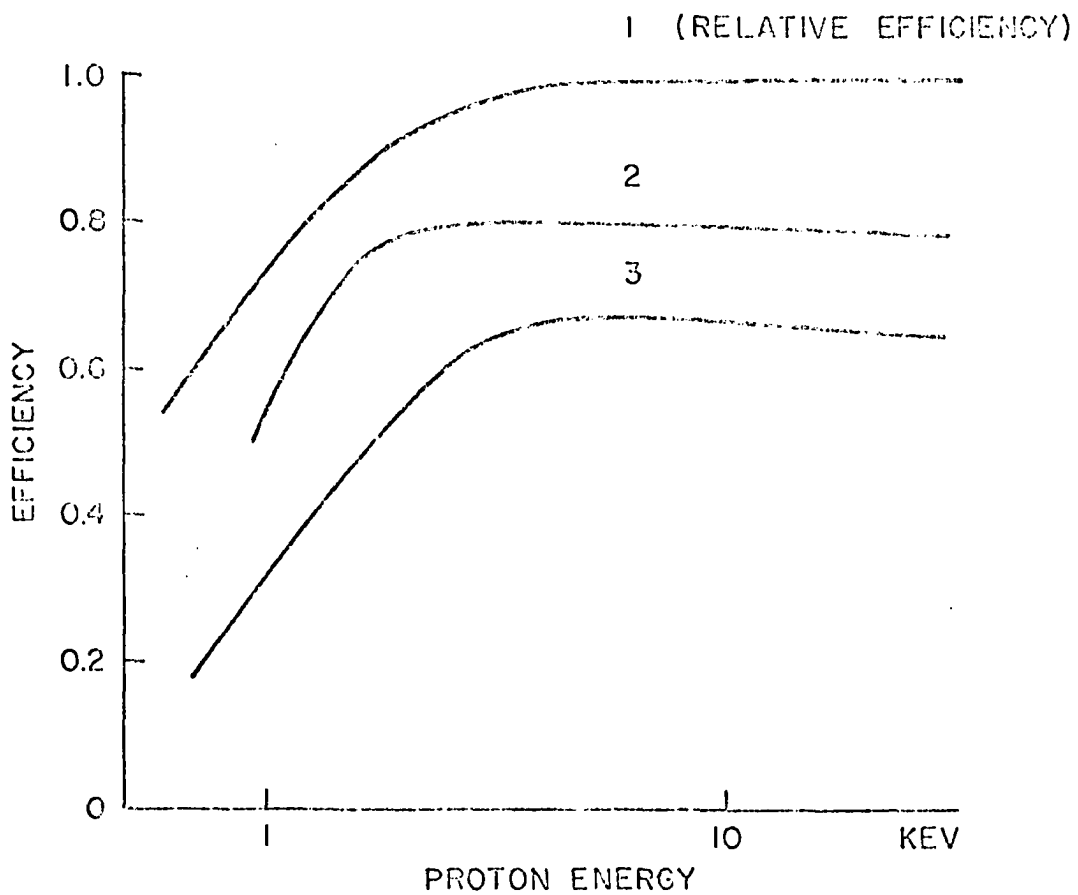

Figure 2.6 The efficiency of channel multipliers for detecting protons. Curve 1 obtained by Burrous et al. (1967) is a measurement of relative efficiency only. Curves 2 and 3 obtained by Tatry et al (1969) and Sharber et al (1968) respectively are absolute efficiency.

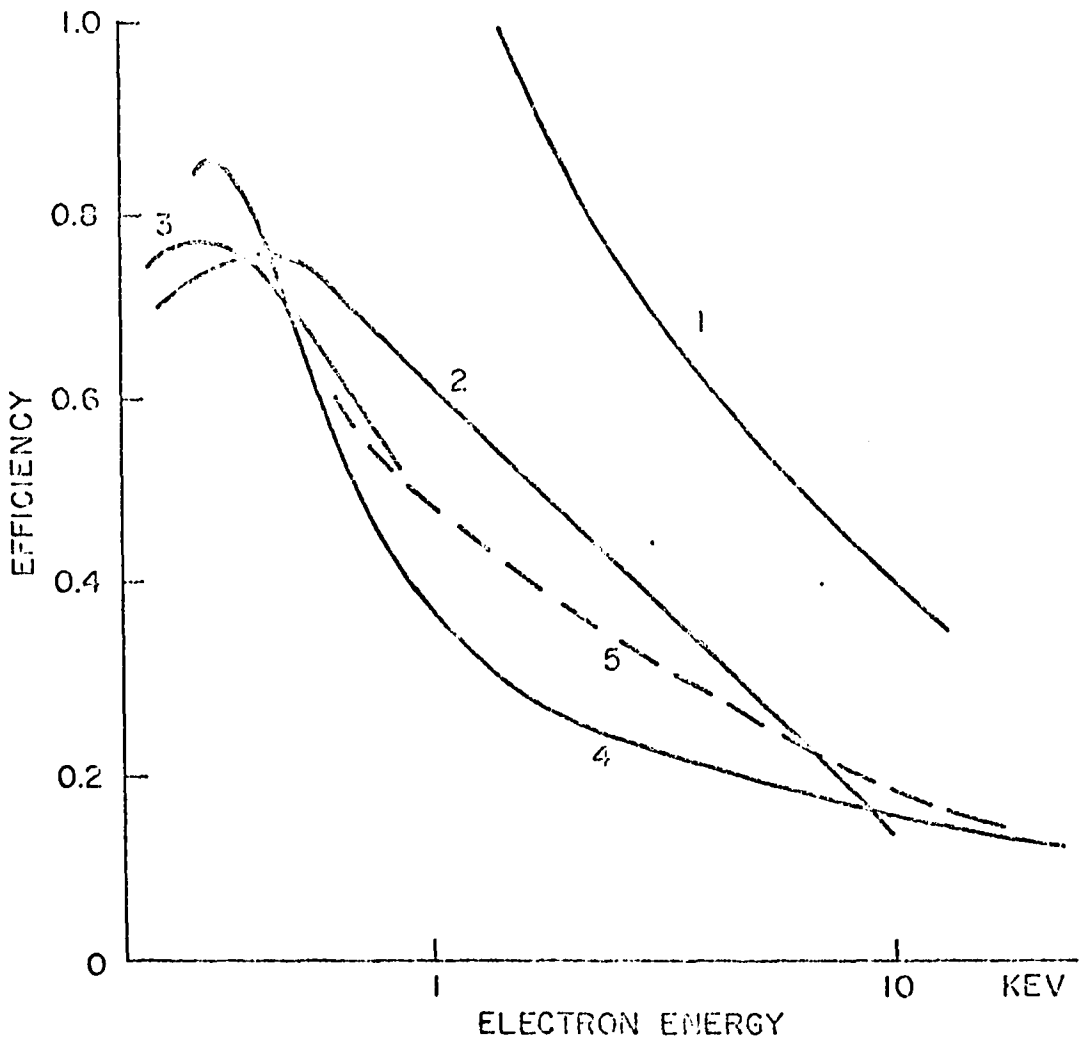

Figure 2.7 Efficiency of channel multipliers for detecting electrons. Curve 1 obtained by Egidi et al (1969) is relative efficiency. Curves 2,3, and 4 by Sharber et al (1968), Bosqued (1967) and Frank (1965) respectively are absolute efficiency. Curve 5 gives the

2.4 Geometric Factor of Cylindrical Analyzer

The geometric factor g(E) of the analyzer and channel multiplier is defined by

$$\text{detector counting rate} = \int_0^\infty g(E)\, n(E)\, dE$$

$n(E)$ is particle intensity in units of particles cm^{-2} $steradian^{-1}$ sec^{-1} kev^{-1} and is assumed to be uniform and isotropic. The dimensions of g(E) are cm^2 steradian. It can be measured or calculated. It is more accurate to measure the geometric factor because it is essentially an empirical factor. In any calculation geometrical idealizations must be made. The calculations are unable to account for inaccuracies in the alignment of the analyzer plates or for fringing field effects. The measurement requires an extensive and careful series of observations of the response of the detector to an electron beam at all energies, entrance positions and angles of incidence. The geometric factors used here have been calculated by a method described elsewhere (Johnstone,1970). The discussion here is limited to the errors involved and the precautions taken to minimize those errors.

It is impossible to calculate the trajectory of a particle through the fringing field at the entrance to and exit from the analyzer plates. However the effect of the fringing field at the entrance aperture can be allowed for completely by an application of Liouville's theorem if it is known that all the trajectories which pass between the plates and strike the channel multipler do not intersect an obstruction in the entrance aperture. The fringing field accelerates some particles, decelerates others and must deflect all of them to some extent. Any collimator placed in the entrance aperture can obstruct some of these trajectories. For

this reason in the design of the analyzers the entrance was left unobstructed by a collimator. Particles could enter the space between the plates at angles up to $\pm$ 16° from tangential. The size of the angle of acceptance is approximately 6° so that no trajectories should have been obstructed. It is harder to allow for the fringing field at the analyzer exit. The end of the channel multiplier was placed as close to the end of the plates as possible. The particles are within a few degrees of being tangential at the exit so that few should be deflected away from the channel multiplier. The main source of error was the misalignment of the analyzer plates. It was found to be difficult with this design to align the plates accurately. The problems were overcome in a later design. A quantitative estimate of the error is impossible but, qualitatively, the error may be as great as 20% in the geometric factor and may be shifted in energy. The accuracy of a particular analyzer is checked in the calibration which allows an estimate of the energy shift. The calculated geometric factor of the cylindrical analyzer $g(E/E_o)$ is shown in Figure 2.8. E_o is the kinetic energy of a particle in a circular orbit in the analyzer.

The wire mesh grid placed over the entrance aperture reduces the geometric factor by an amount which is independent of energy. The optical transmission of the grid is h where

$$h = (1-nd)^2$$

n - number of squares per inch in the mesh = 30

d - diameter of the wires forming the mesh = 0.006"

Therefore h = 0.67

The total geometric factor is then hg(E).

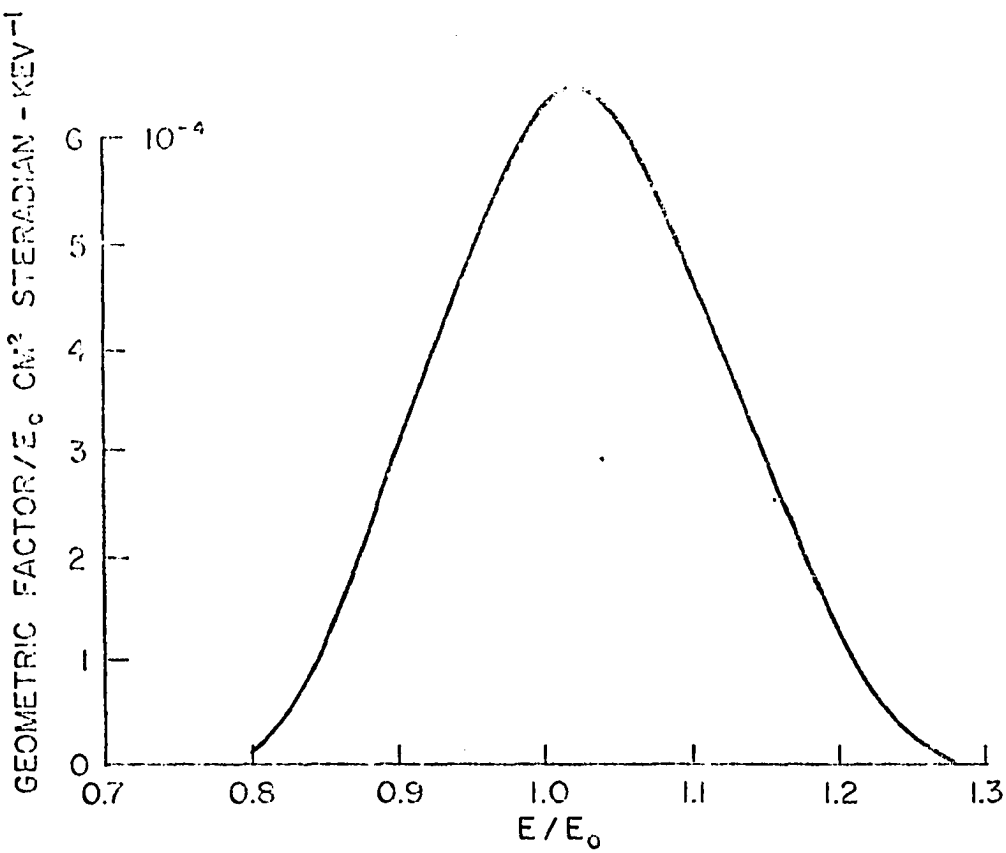

Figure 2.8 The calculated geometric factor of the cylindrical plate electrostatic analyser. Eo is the kinetic energy of a particle in a circular orbit in the analyser.

In the analysis of the proton data, each sweep of the analyzer voltage is divided into ten equal segments of time and the counts occurring in each segment are recorded separately. This enables the spectrum to be calculated. The segments are called energy bins for convenience. To estimate the particle intensities from the counts per bin the quantity geometric factor x time must be calculated. Let N(I) = the number of counts in bin labeled I; then

$$N(I) = \int_0^\infty N(E)\, dE \int_{t_1}^{t_2} g(E/E_o)\, dt$$

E_o is a linear function of time.

Therefore

$$N(I) = \int_0^\infty n(E)\, dE \frac{dt}{dE_o} \int_{E_1(I)}^{E_2(I)} g(E/E_o)\, dE_o$$

where $E_1(I)$ and $E_2(I)$ are the values of E_o at the edges of the bin (I)

Put $T = E/E_o$ then

$$N(I) = \int_0^\infty n(E)\, dE \frac{dt}{dE_o} E \int_{T_2(I)}^{T_1(I)} \frac{g(T)}{T^2}\, dT$$

$$= \frac{dt}{dE_o} \int_0^\infty n(E)\, \tau_I(E)\, dE$$

where $\tau_I(E) = E \int_{T_2(I)}^{T_1(I)} \frac{g(T)}{T^2}\, dT$

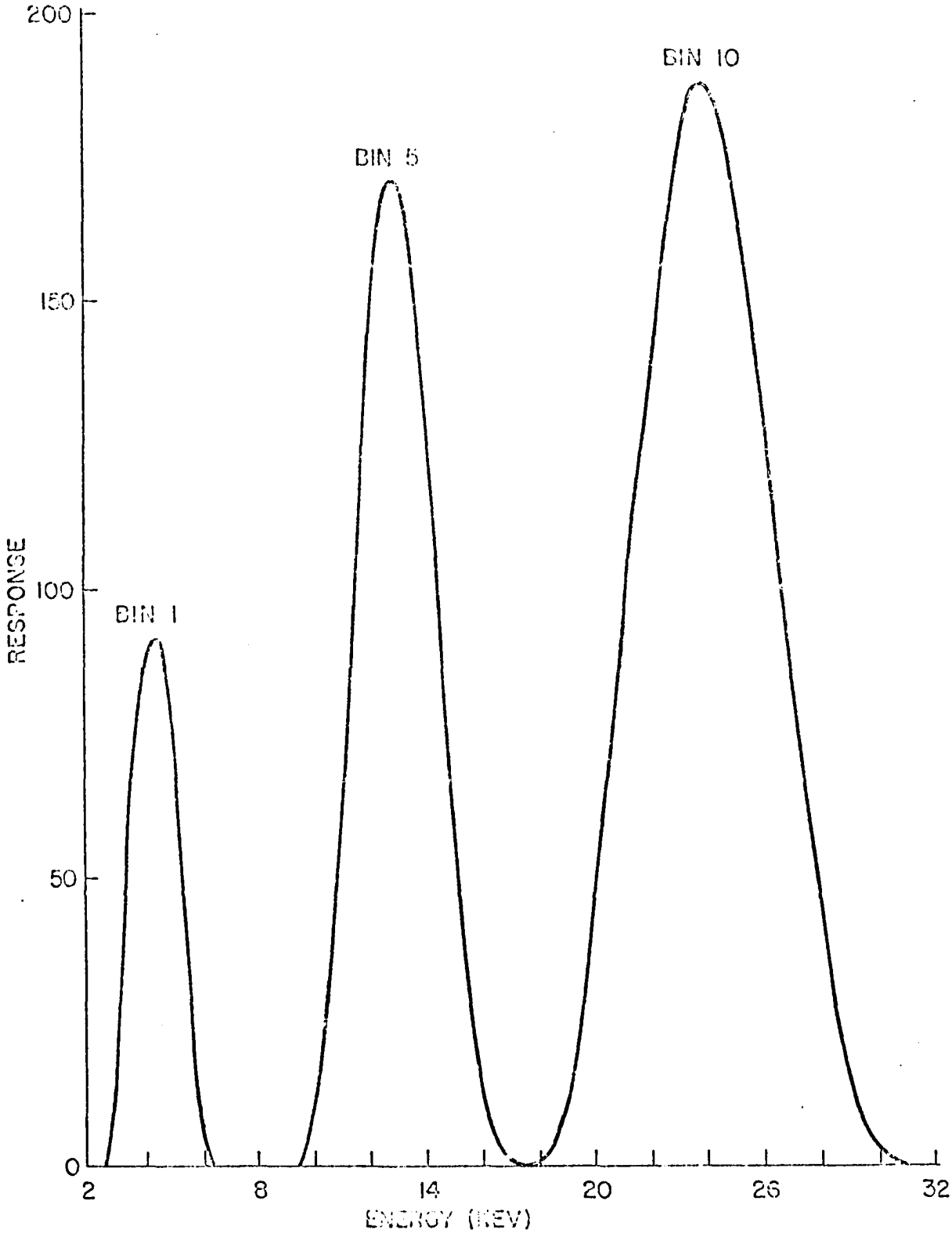

Figure 2.9 The energy response of three of the ten energy bins.

The function $\tau_I(E)$ is plotted in Figure 2.9 for bins 1, 5, 10 to illustrate the energy response of the bins. The higher energy bins obviously are very wide.

2.5 Payload Instrumentation

Six particle detectors, differing only in the voltage applied to the analyzer plates, were carried in the payload. The energy passband on the proton detector was varied continuously from 3 kev to 24 kev. An electron detector swept through the same energy range. Three electron detectors were set at fixed energies of approximately 2.5 kev, 5 kev and 10 kev. The sixth detector had both analyzer plates grounded and was intended as a control detector to measure the effects of scattered particles, penetrating particles, ultraviolet light, high voltage noise and high voltage corona effects. The six detectors were mounted together and all pointed in the same direction, at 65° to the spin axis of the rocket, Figure (2.10). They were supplied from a single high voltage supply and each was connected to its own telemetry channel. The detectors looked through a port in the side of the rocket which was covered by a hatch until T + 53 secs (reckoning T + 0 to be the instant of launch). The high voltage was switched on at T + 120 secs when the rocket was at an altitude of 160 kms. At this altitude the ambient pressure is well below the pressures at which high voltage breakdown or discharge occur. The payload also had time to outgas through the hatch prior to switching on the high voltage. All external surfaces in the neighborhood of the detectors were metallic and grounded to the rocket frame except the outer covers of cables. All the cables carrying high voltages were coaxial with the outer conductor grounded. Therefore all surfaces near the

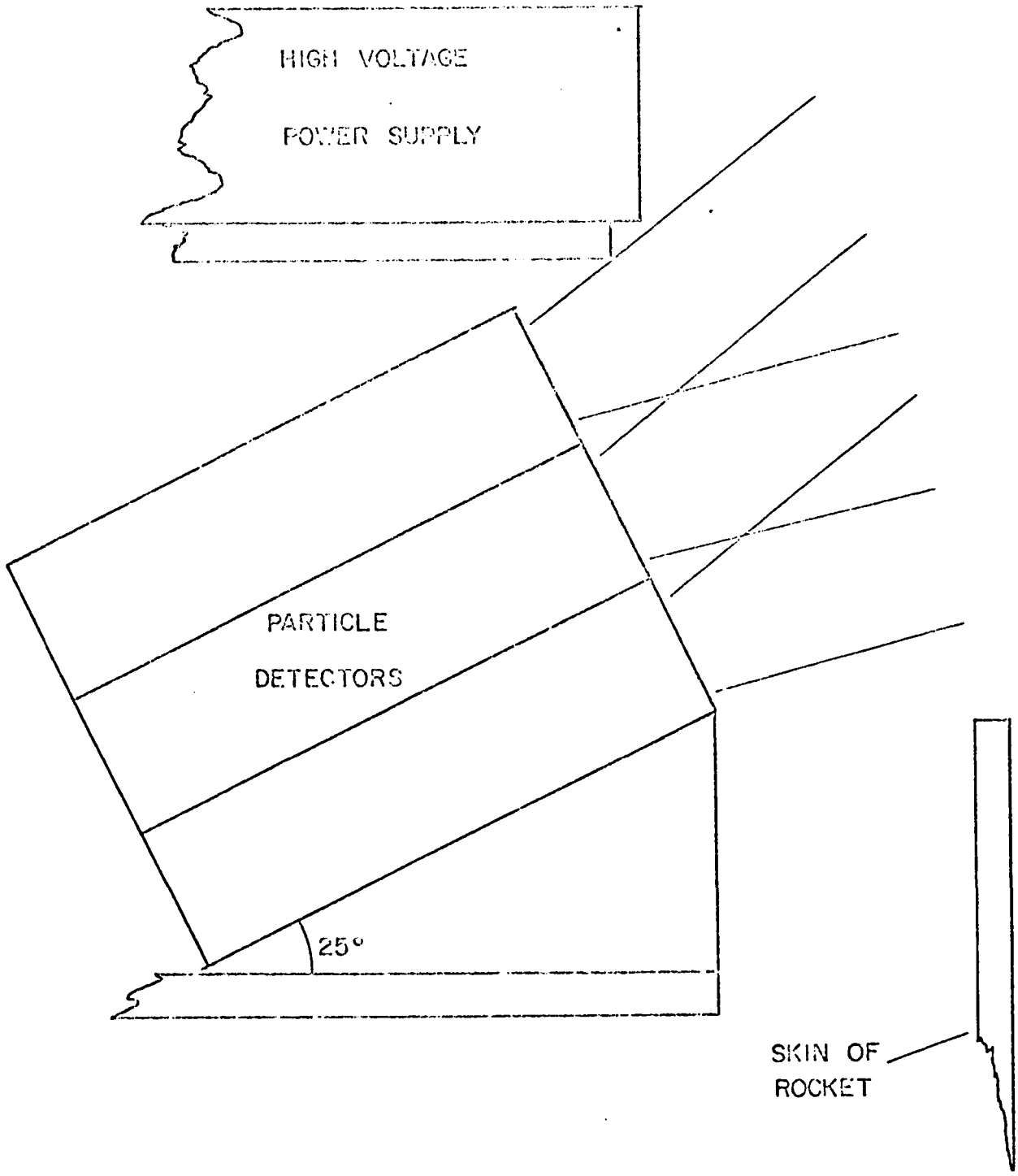

Figure 2.10 The position of the particle detectors with respect to the skin of the rocket. They are mounted in two groups of three, side-by-side. The angle of acceptance is indicated.

detectors were at well-defined potentials and were unaffected by the presence of energetic or thermal plasma.

The payload also carried two photometers, two attitude magnetometers and two flashing lights. The photometers consisted of 1P21 photomultipliers with interference filters and collimators made from bundles of aluminum tubes 2.5" long, 0.050" internal diameter. The sensitive area of each was approximately 0.75" diameter, and the cone of acceptance had a full angle of 5.8°. The filter characteristics were as follows. The transmission curve at half maximum extended from 4260Å to 4298Å for one and from 4850Å to 4878Å for the other. The former covered the N_2^+ first negative band which is excited by precipitating particles, both electron and proton. The latter covered the beta line in the hydrogen Balmer series and was thus a measurement of proton precipitation. The photometers were designed by W. Murcray and have been flown by him many times. They were mounted next to the particle detectors and looked out through the same hatch at 90° to the rocket spin axis.

The attitude magnetometers were type MFM designed and built by the Goddard Space Flight Center Sounding Rocket Branch. One magnetometer was aligned with the spin axis of the rocket and the other was mounted perpendicular to it. The magnetometers were not calibrated in the payload and were in a position where payload magnetic fields were quite high. The data are to be used with caution. Later, in another identical payload, the magnetometers were calibrated and the magnitude of some of the disturbing effects was measured. Where possible these corrections have been applied to the data from this rocket.

The flashing lights were Xenon flash tubes mounted on doors on opposite sides of the rocket. The doors opened at T + 56 secs. The energy consumed in each flash in each tube was 7 joules and the flash frequency was 1Hz. The lights were observed by television cameras at two ground-based locations to find the position of the rocket.

2.6 Trajectory of the Rocket

The analysis of the television observations has not been completed and so an approximate trajectory has been calculated. The accuracy is adequate for the purposes of this work. The positions of two particular flashes, seen simultaneously at both ground stations, have been measured relative to the star background. The altitude on these two occasions was then calculated. These two altitudes and the time difference between them were compared with a sample altitude/time profile for a rocket in drag-free ballistic flight. The two points fit the curve if the altitude at apogee is 227 kms. The Nike Tomahawk performance handbook (Thiokol, 1966) predicts an apogee of 227 kms for a payload 120" long, 240 lbs weight launched at an effective launch elevation angle of 86°. These parameters are very close to the actual values for rocket number 13.15. Predicted impact time is T + 459 seconds. The actual time of the loss of the telemetry signal was T + 463 seconds. The payload did not have a clean aerodynamic configuration on the flight downleg and that easily accounts for the difference between prediction and observation. The predicted time to apogee is 233 secs. The predicted times at the two altitudes of the flashes were calculated and compared with the times of the observations. The predictions were two seconds earlier than the observations. One second was then added to the predicted times to give the altitude time

profile used in later calculations. The accuracy should be within ± 3 kms at any time,

Table 2.2

Observations of Two Flashes

Time	Altitude
T + 120	164 kms
T + 183	214 kms

Table 2.3

Altitude Time Profile

Altitude (kms)	Time (secs)	Altitude (kms)	Time (secs)
170	123	220	275
180	133	215	285
190	144	210	295
200	157	205	303
205	164	200	310
210	172	190	323
215	182	180	335
220	192	170	345
225	209	160	354
227	234	150	363
225	258	140	371
		130	378

2.7 Attitude of the Rocket

The attitude of the rocket must be known to calculate the pitch angles of the particles and to interpret photometer data. For the first, all that is needed is a knowledge of the angle between the spin axis of the rocket and the direction of the Earth's magnetic field. This information is given by the magnetometer mounted perpendicular to the spin axis together with knowledge of the magnitude of the Earth's magnetic field. To use the photometer data the angle between the spin axis and the zenith is required. It is necessary to make further assumptions to obtain this value.

The magnetometers in payload 18.15 were subject to a number of errors. These were

(a) permanent magnetic fields from relays and commutators mounted nearby,

(b) electromagnetic fields from currents in the payload wiring,

(c) the magnetic field of eddy currents induced in the skin and frame of the rocket by its spin.

The error from (a) was quite severe. This was evident from the fact that the lateral magnetometer did not oscillate about zero as the rocket spun. Twice per revolution the magnetometer was perpendicular to the Earth's magnetic field and should have measured zero field. The actual offset was measured at 175 milligauss. The offset in the longitudinal magnetometer cannot be determined, nor can measurements on another payload give its magnitude. The information from this magnetometer cannot be used, and the magnitude of the Earth's field must be obtained another way. The errors from (b) and (c) can be estimated

by use of measurements made on another payload. The effect of payload currents is negligible but eddy currents cause a noticeable reduction in the amplitude of the spin modulation. At a spin rate of 5.7 Hz the reduction is by a factor of 0.93. The amplitude of the spin modulation is the value of the component of the Earth's magnetic field perpendicular to the rocket spin axis. Its measurement is unaffected by stray magnetic fields from components in the rocket.

The spin axis of the rocket precessed around a cone with a period of 38.6 secs. The amplitude of the spin modulation goes through a sinusoidal modulation with this period. The amplitude has been measured at successive maxima and minima of this modulation up to apogee and recorded in Table 2.4. The value of the Earth's magnetic field at these times has been calculated from the following data:

(a) Quiet level of the magnetic field at ground level at College for the month of March 1969,

Vertical component Z = 553.21 milligauss

Horizontal component H = 129.06 milligauss

(provided by H. Olsen). $\therefore |B| = 568.06$ milligauss

(b) The trajectory given in section 2.6 is used to make an inverse cube correction to the field strength ie

$$\frac{|B|(170 \text{ kms})}{} = \frac{|B|(\text{ground})}{} \frac{r^3}{(r+170)^3}$$

The value of r is 6360 kms.

The angle α between the spin axis and the magnetic field is given by

$$\alpha = \sin^{-1} \left| \frac{\text{spin amplitude}}{\text{field strength}} \right|$$

Table 2.4

Rocket Attitude Data

Time secs	Altitude kms	Amplitude milligauss	Angle α degrees
92.5	130	212	23.4
110	155	175	19.3
127.5	174	207	23.3
150	195	167	18.8
169	207	202	23.0
187	218	165	18.8
206	225	205	23.6
225	226	167	19.0

Mean values 23.3°coning maximum

19.0°coning minimum

The spin frequency of the payload was 5.68 Hz

To get the relation between the zenith and the axis about which the spin axis precesses, it is assumed that the axis lies in the plane of the trajectory. The flight azimuth was 021.1° and the declination of the magnetic field near apogee was 029.5°. The data are summarized in Figure 2.11. The dip angle at the mid point of the trajectory is estimated to be 77.0°.

2.8 Pitch Angle Coverage

The detectors accept particles within a finite range of pitch angles. As the rocket spins, this range varies. If any quantitative estimates of the pitch angle distribution are to be made it is necessary to know the relative coverage of pitch angles during one spin of the rocket.

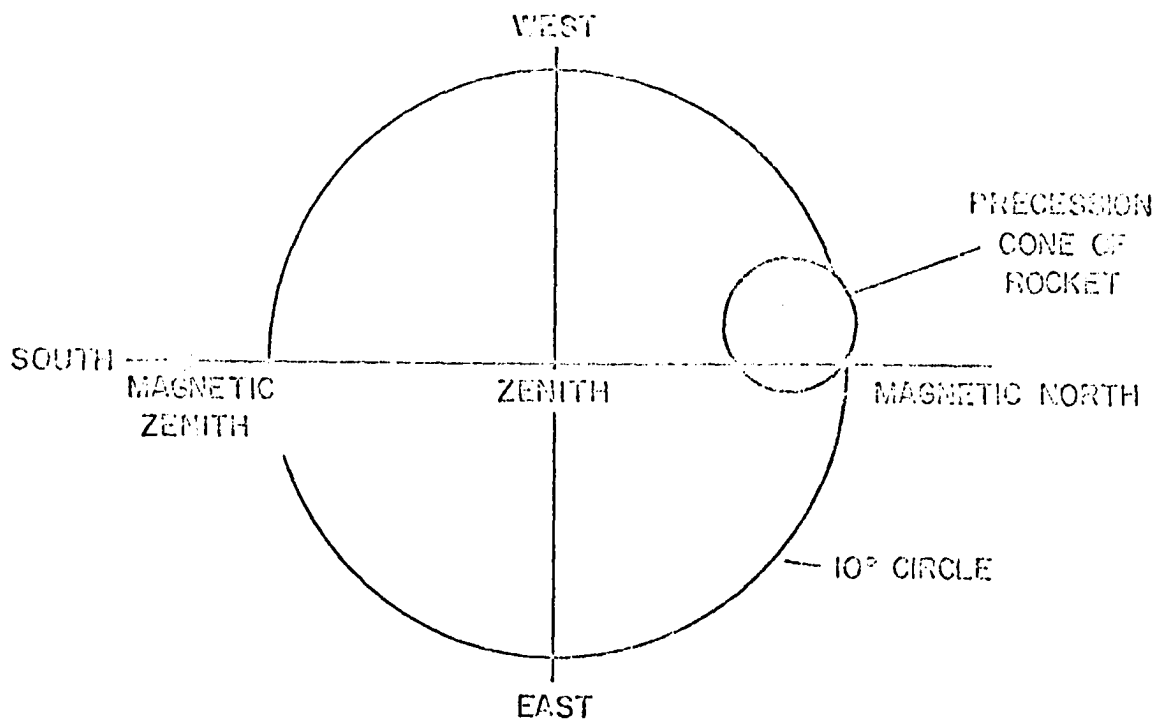

Figure 2.11 A polar plot summarising the attitude data. The spin axis of the rocket precesses around the cone of directions indicated with a period of 38 seconds.

Consider first an elementary part of the solid angle of acceptance of the detector with dimensions $\delta\ \theta$ in the plane containing tne spin axis, perpendicular to this at an angle θ to the spin axis. In one spin the detector sweeps through a range of pitch angles. With reference to Figure 2.12a the solid angle within the range $d\lambda$ at λ is

$$\delta\sigma = 2\sin\theta\, d\theta d\phi\ , \qquad 2.8.1$$

where ϕ is the angle specifying the azimuthal position of the rocket in its spin. The relation between λ and ϕ is (Figure 2.12b)

$$\cos\lambda = \cos\theta\cos\alpha + \sin\theta\sin\alpha\cos\phi$$

$$+ \sin\lambda\cdot d\lambda = \sin\theta\sin\alpha\sin\phi d\phi. \qquad 2.8.2$$

where α is the angle between the spin axis and the magnetic field.

The detector has a finite width ψ along the ring, and the amount of time during each spin that the element within $d\lambda$ is in the detector angle of acceptance is γ

$$\gamma = \frac{\psi}{2\pi\sin\theta} \times \frac{2\pi}{\dot{\phi}} = \frac{\psi}{\dot{\phi}\sin\theta} \qquad 2.8.3$$

$$\times \frac{2\pi}{} =$$

Combining equations 1, 2, 3 the pitch angle coverage function $C(\theta,\alpha,\lambda)$ is given by

$$C = \frac{2\psi}{\dot{\phi}} \frac{\sin\lambda}{\sin\alpha} \int_{\theta_1}^{\theta_2} \frac{d\theta}{\sin\phi\sin\theta} \qquad 2.8.4$$

where θ_1, θ_2 are the limits of the detector aperture. The units of C are radian seconds per spin. Substitute for $\sin\phi$ from equation 2 to evaluate the integral. It is elliptical and so has been computed numerically. The result is shown in Figure 2.13. The most curious features are the cusps at $\lambda = \theta_1 - \alpha\ ,\ \theta_2 + \alpha$.

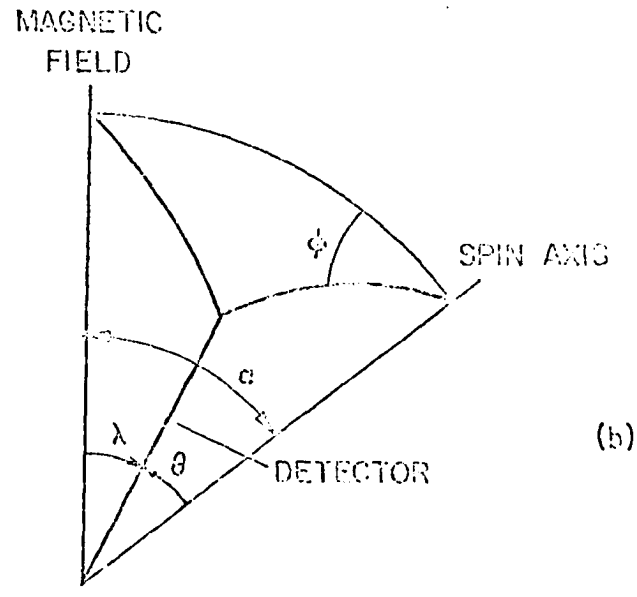

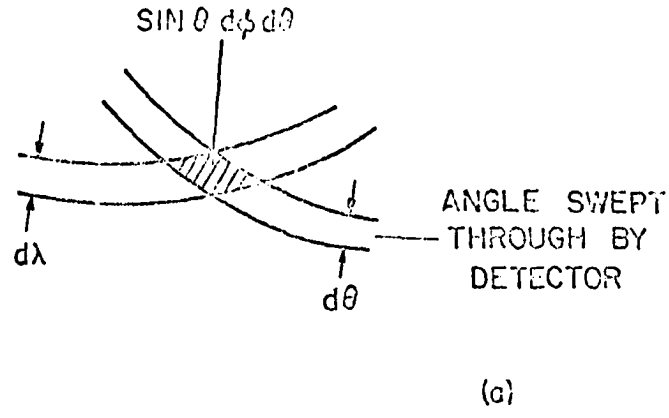

Figure 2.12 Diagram defining the angles used in the calculation of the pitch angle coverage function.

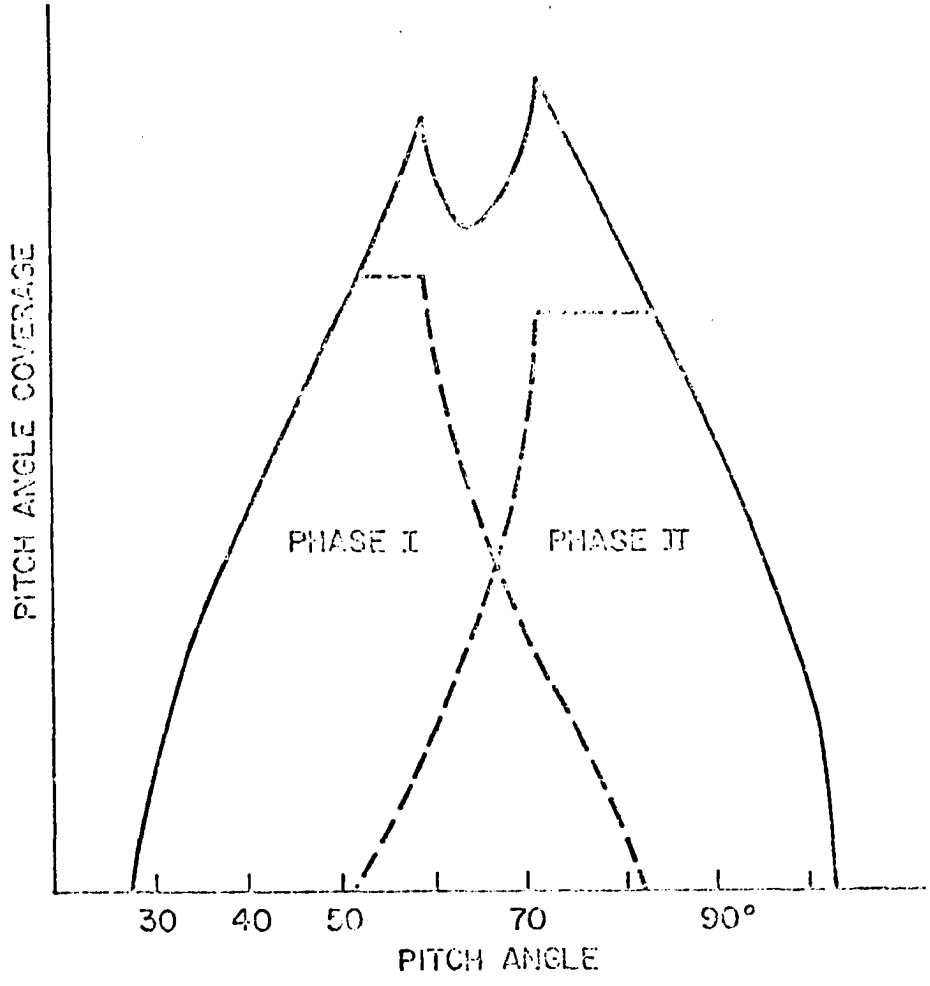

Figure 2.13 The pitch angle coverage as a function of pitch angle. In the analysis of pitch angle distributions the pitch angle ratio is the ratio of the counts received in Phase I to those in Phase II.

In the data analysis each spin was divided into two equal segments corresponding to the times when the detectors were looking at (1) the smallest pitch angles and (2) the largest pitch angles. The pitch angle coverage function for these two spin phases is also shown in Figure 2.13.

2.9 Statistics of the Proton Counting

The proton counting rate during the flight of payload 18.15 was very low, averaging 30 counts per second. During most of the 3 msec counting periods no counts were registered. Under these circumstances it is expected that in a very small fraction of the periods more than one count would have been registered. In fact, the raw data showed as many double and triple as single counts; in some periods as many as six pulses were recorded. Clearly, not all these pulses could have been caused by separate protons. The question to be answered is whether any of the pulses were related to protons. To decide the question the data are examined for systematic variations and compared with the variations expected for protons or noise.

The most likely cause of spurious or multiple pulsing is high voltage noise originating either in the analyzer or in the voltage applied to the channel multiplier. If it originated in the channel multiplier and the associated circuitry, one of the following effects is expected.

(a) A continuous pulsing independent of time though probably sporadic if caused by faulty wiring,

(b) A decrease in the count rate with altitude if the pulsing is related to ambient pressure in the multiplier,

(c) A steady decrease in counting rate with time if it is caused by slow outgassing.

If the noise originated in the analyzer then the maximum counting rate is expected when the voltage between the plates is a maximum, that is at apparently high proton energies.

In fact the data show a variation at the frequency of the sweep with the maximum counting rate at the lowest proton energies. There is a variation with altitude but with the maximum counting rates occurring at the highest altitudes. As the rocket reentered the atmosphere, the counting rate dropped to a very low level before obvious high voltage breakdown started just below an altitude of 90 kms. In the 9 seconds before breakdown there were 11 counts, some of which were certainly caused by protons. Therefore it seems very unlikely that high voltage breakdown was the cause of the spurious pulsing, although it is the only explanation found so far which accounts by itself for all the pulses. The other possibilities depend on one original proton pulse being registered in the counter as more than one pulse. It is possible that reflections in the coaxial line between the preamplifier and the counting circuit could have led to extra pulses. Tests were made with identical circuits using pulse generators to find out if this was the cause. The effect could not be reproduced.

Other sources of spurious counts do not generate pulses in sporadic bursts. For example, cross talk from neighboring counters, ultra violet light and penetrating radiation all could have generated spurious counts. Cross talk can be eliminated as a major effect because the counting rate does not correlate at all with the neighboring counters, the control detector and the 2.5 kev electron detector, but it does show some correlation with the 10 kev electron detector and the electron

sweep detector. Also, when an especially high level was recorded in the proton detector the other detectors were checked to see if they recorded a high count. None was found. Ultra violet light should have most effect at low altitudes because the detectors look upwards, and penetrating radiation would be unaffected by the high voltage sweep on the analyzer.

The remaining explanation which can account for all the observed features and which has been substantiated experimentally by other workers is that the extra pulses are caused by ion after-pulses in the "clean-up" period of the channel multiplier (section 2.1). The data from a later flight in which the counting rates were low in all channels also show the same effect. In that payload great care was taken to match the amplifiers to the counters and avoid spurious counts from reflections in the line. That this is the cause will not be certain until definitive tests have been performed. However, it seems that the data are reliable, and, if corrections are made, the intensities can be calculated. The data should have a Poisson distribution of counts. An inspection of the data suggested the following scheme of correction; one, two, or three counts in a single period would be recorded as one proton; four, five and six as two protons; and more than this as three. The highest level recorded was eight. The number of ones, twos, and threes recorded was compared with the number expected for a Poisson distribution.

The Poisson distribution is

$$P(n) = e^{-\nu} \frac{\nu^n}{n!}$$

where P(n) is the probability of observing n counts in a set time interval, and ν is the average number of counts expected in that interval. Thus

$$P(2)/P(1) = \nu/2$$

The time interval is the counting period of 3 msec. In a long period, when many protons have been recorded, the number of twos can be predicted from the number of ones recorded. This was done and the predicted number compared with the observed number. There were always more observed than predicted. The distribution of the excess twos is given in Table 2.5.

Table 2.5

Distribution of Excess Twos

	Energy Bin									
Sweeps	1	2	3	4	5	6	7	8	9	10
1-41	18	19	8	6	2	10	10	5	6	11
42-80	-6	9	6	7	18	6	9	1	8	11
81-119	11	-2	1	1	5	8	2	4	6	5
Total	23	26	15	14	25	24	21	10	21	27
Actual No. of twos	110	93	55	55	60	55	47	33	44	46

From Table 2.5 it can be seen that

(1) in 28 out of 30 samples the excess is positive,

(2) the actual number of twos was much greater for the lower number energy bins where the count rate was also higher,

(3) the distribution of excess twos is independent of energy bin.

The rate of recording excess twos is a function of time, see Table 2.6.

Table 2.6

Time Variation of Excess Twos

Sweeps	No. of excess twos per sweep
1-41	2.3
42-80	1.76
81-119	1.05
120-131	0.92

The correction procedure gives fewer twos than occur in reality because a three may be a combination of a one and a two.

These features suggest that the excess twos are caused by some noise effect such as those discussed at the beginning of this section. The count rates have been corrected for this small amount. It is only of importance in the spectral analysis because the same correction must be subtracted from all energy bins. The source of this noise is not necessarily related to the effect causing the after-pulsing.

As a check on the effectiveness of the correction for after-pulsing the ratio of counts/sweep before correction to after correction has been calculated as a function of time in Table 2.7. It is not a function of time or counting rate.

Table 2.7

Correction Ratios

Sweeps	Ratios	No. of Counts
13-15	1.96 $\pm$ .15	258
21-23	2.10	202
30-32	1.98	247
42-44	1.92	239
54-56	2.01	283
66-68	1.92	261
78-80	1.97	209
90-92	1.96	190
102-104	1.89	148
114-116	1.84	151
126-128	1.81	74

The conclusion is that the correction is valid and that protons are being detected. The intensity values are uncertain by a small amount as a result of uncertainties in the correction procedure.

CHAPTER 3

ENERGY SPECTRUM OF THE PROTONS

3.1 Introduction

In Figure 3.1 the counting rate of the proton detector is plotted as a function of time for the entire flight. Energy bins 1 through 5 corresponding to energies 3 kev to 14.5 kev and bins 6 through 10 (energies 13 kev to 26 kev) have been totaled together and plotted separately to give some idea of the changes in the proton spectrum throughout the flight. There are obvious time and spectral changes on several occasions. These changes are intrinsically interesting and are discussed in detail in Chapter 5. In this chapter the gross features of the proton spectrum are discussed. The next chapter is concerned with the pitch angle distribution.

The main purpose of this chapter is to find the form of the proton spectrum above the atmosphere. The atmosphere distorts the spectrum in several ways, and the spectrum measured at the rocket must be corrected for these effects. In the next section the theory of the interaction of a proton beam with the atmosphere is reviewed briefly before the actual numerical corrections are discussed.

Each energy bin covers a fairly wide range of proton energies so that it is not sufficient to take the counting rate in a particular bin as being representative of the proton spectrum at the energy at the mid point of the bin. This means that the proton spectrum cannot be obtained directly from the counting rates of the energy bins. It is necessary to assume a spectral shape, combine it with the geometric factor of the bins and then compare it with the observations. This

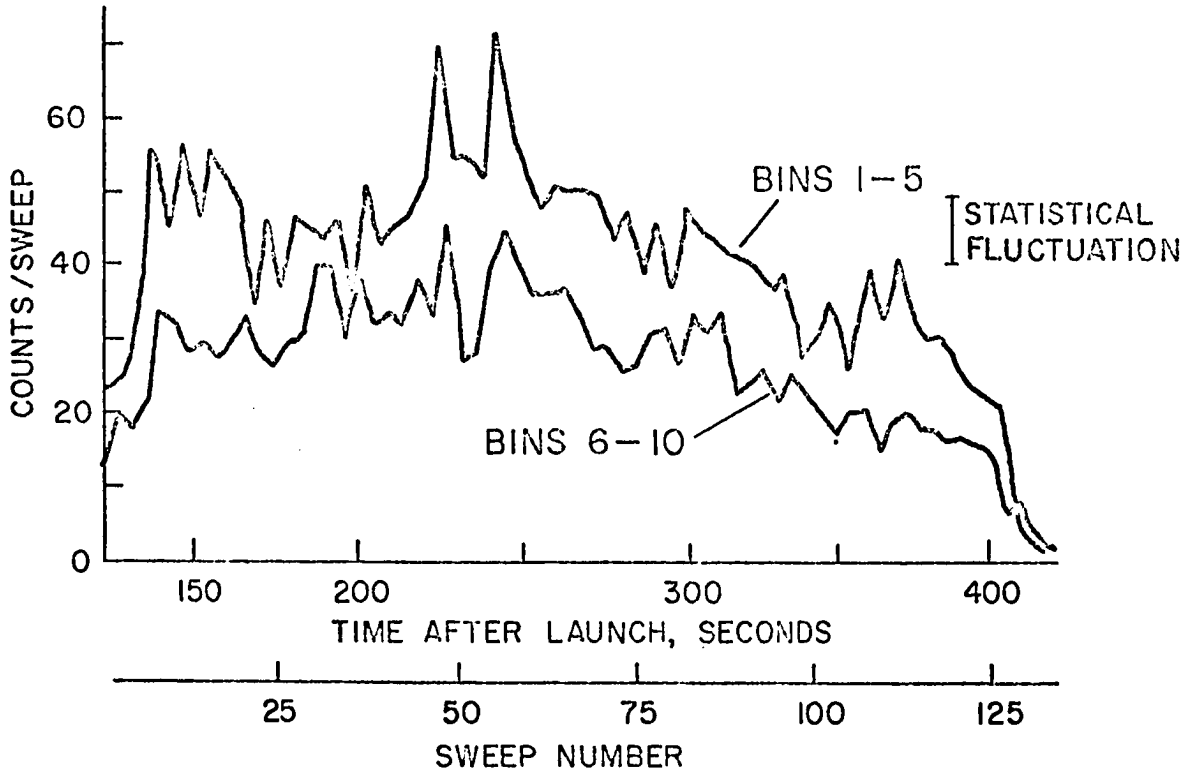

Figure 3.1 Proton data for the complete flight. Low energy (3-14 kev) and high energy (14-26 kev) protons have been totalled separately.

This approach is followed in making all the corrections. The primary proton spectrum is assumed to have either a power law form $n \sim E^{-\nu}$ or an exponential form $n \sim \exp(-E/E_1)$. After allowing for atmospheric effects the counting rate in each energy bin is calculated. Effectively the experimental data are synthesized theoretically. The input parameters are varied until a close match is obtained. The method is quite accurate enough to distinguish clearly between the two forms of spectrum. The proton spectra were also calculated simply by taking the count rate of a bin as being representative of the spectrum at its mid energy. Precisely the same results were obtained, even to the extent of having the same value for the spectral parameters.

3.2 The Interaction of a Proton Beam with the Atmosphere

A proton with less than 100 kev energy has a strong probability of collecting an electron from an atmospheric molecule and becoming a neutral hydrogen atom. In a subsequent collision it loses the electron and becomes a proton again. The chain of reactions is as follows.

$$H^+ + X \longrightarrow X^{+(*)} + H^* \qquad 3.2.1$$

$$H^* \longrightarrow H + h\nu \qquad 3.2.2$$

$$H^* + X \longrightarrow H^+ + X^{(+)(*)} + (2)\, e \qquad 3.2.3$$

The charge-exchange cycle, as it is known, is important because the neutral hydrogen atoms are able to cross magnetic field lines and are not detected by the proton detector on the rocket. The photon emitted in reaction 2 is Doppler-shifted in wavelength when observed at the ground because it is emitted by a moving hydrogen atom. The profile of

the hydrogen emission lines seen at the ground is broadened by this effect. The shape of the profile depends on the pitch angle distribution and energy spectrum. The proton loses energy in charge-exchange and non-charge-exchange collisions.

A primary beam of protons incident on the atmosphere soon becomes a beam of protons and hydrogen atoms. The fractional composition of the beam reaches an equilibrium which is maintained although individual particles are still cycling from protons to hydrogen atoms and back. Some even become negatively charged hydrogen ions. The fraction $F_{i\infty}$ of the beam in charge-state i (1 for protons, 0 for hydrogen atoms and $\bar{1}$ for negative ions) is called the equilibrium fraction. $F_{\bar{1}\infty}$ is less than 2% above 3 kev (Allison 1958) and is ignored here, hence

$$F_{i\infty} = \frac{\sigma_{ji}}{\sigma_{ij} + \sigma_{ji}},$$

where σ_{ij} is the cross-section for charge-exchange form state i to state j. The equilibrium fraction may be regarded as either the fraction of the beam in a charge state or the fraction of time a particle spends in that charge state. The approach to charge equilibrium of a proton beam is given by

$$F_1 = F_{1\infty} + F_{0\infty}\, e^{-\pi(\sigma_{01}+\sigma_{10})} .$$

π is the atmospheric thickness traversed in atoms cm^{-2} (Eather 1967).

The altitude at which a proton beam has reached 90% of its equilibrium fraction has been calculated for a model atmosphere by Eather (1967). For primary energies below 30 kev the beam is essentially in equilibrium by the time it reaches an altitude of 290 kms. In the

moderation of the proton beam for energies below 30 kev the proton goes through 10 charge-exchange cycles for every kev of energy lost.

3.3 Numerical Synthesis of the Data

To synthesize the data at a particular depth in the atmosphere, an assumed primary proton spectrum is modified by the effects of energy loss in the atmosphere as a function of pitch angle and energy. The fraction of the beam in the proton state is calculated and the spectrum is then integrated over the pass bands of the energy bins. Since the channel multipliers have less than perfect efficiency, only a fraction ϵ (section 2.3) of these protons are counted. The numerical data on which these calculations are based are discussed in the following paragraphs.

3.3.1 Atmospheric model. The independent variable in the calculations is the atmospheric depth. For the purposes of the calculation only the atmospheric composition need be known so that the correct equilibrium fractions and range-energy relations can be used. Figure 3.2 shows the principal constituents of the atmosphere as a function of altitude. In the height region of interest the most important constituent is atomic oxygen. If the calculations are to be related to measurements made from the rocket, the atmospheric depth must be calculated as function of altitude. The atmospheric model used to make these calculations is the U.S. Reference Atmosphere (1962). The depth has been obtained by a simple numerical integration from the published tables. The units of atmospheric depth and proton range are equivalent cms of the gas at 1 mm of mercury pressure and 15°C temperature. Here they are called standard cms.

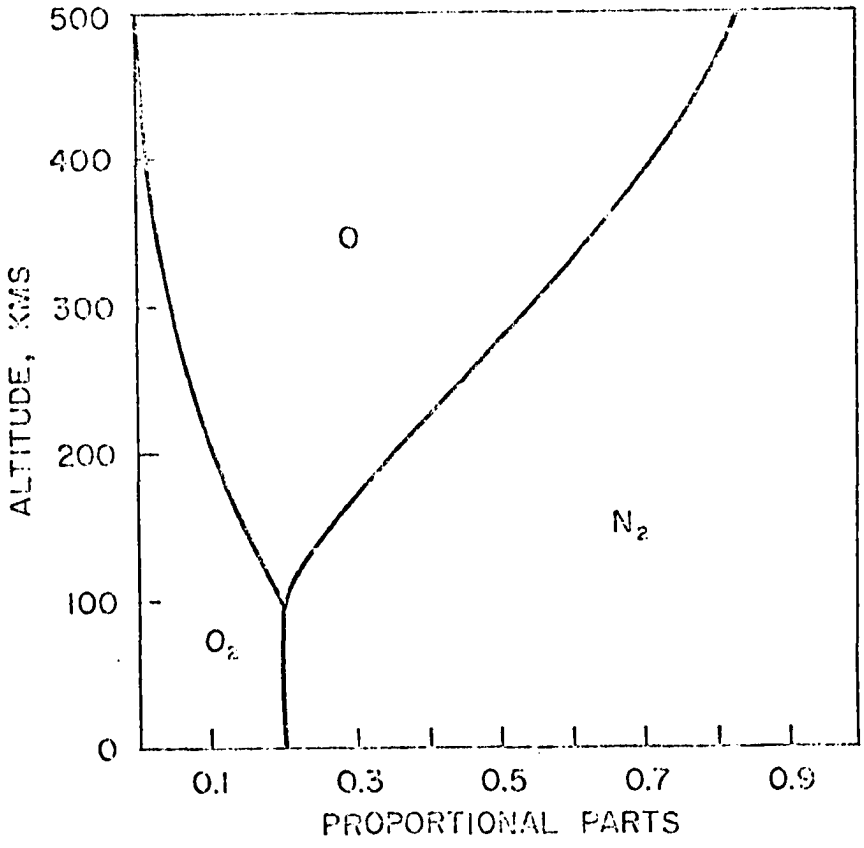

Figure 3.2 Relative proportions of the major atmospheric constituents in the height range of the proton interaction with atmosphere from the Handbook of Geophysics (1957).

3.3.2 Equilibrium fraction. In Figure 3.3 equilibrium fraction data for various target gases, tabulated by Allison (1958), are plotted. However, no experimental data are available for atomic oxygen the principal atmospheric constituent. The best that can be done is to hope that the equilibrium fraction of atomic oxygen does not differ greatly from that of molecular oxygen. Since such a sweeping assumption must be made, there is little point in making detailed corrections for the equilibrium fraction by including such refinements as a mixture of the values for different gases according to the correct atmospheric composition. A straight line has been fitted to the data for molecular oxygen and nitrogen and is indicated in Figure 3.3. The numerical values are

$$F_{1\infty} = 0.0138E(\text{kev}) + 0.093 \qquad 3.3.1$$

It has been assumed that the proton beam as measured is in equilibrium even at apogee of the rocket. In the light of Eather's (1967) calculations quoted in section 3.2 this is quite reasonable. It is assumed further that as the energy of the protons is degraded they maintain equilibrium at the value expected for their current energy. The data of Allison have been extrapolated from 3 kev down to 2.4 kev to cover the range of the measurements.

3.3.3 Energy loss of protons. Several workers have made measurements of the extrapolated range of protons in various gases as a function of energy. The data of Cooke et al (1953) have been used here. They expressed their results in terms of the empirical relation

$$R = kE^n \quad \text{for} \quad E < E_o$$

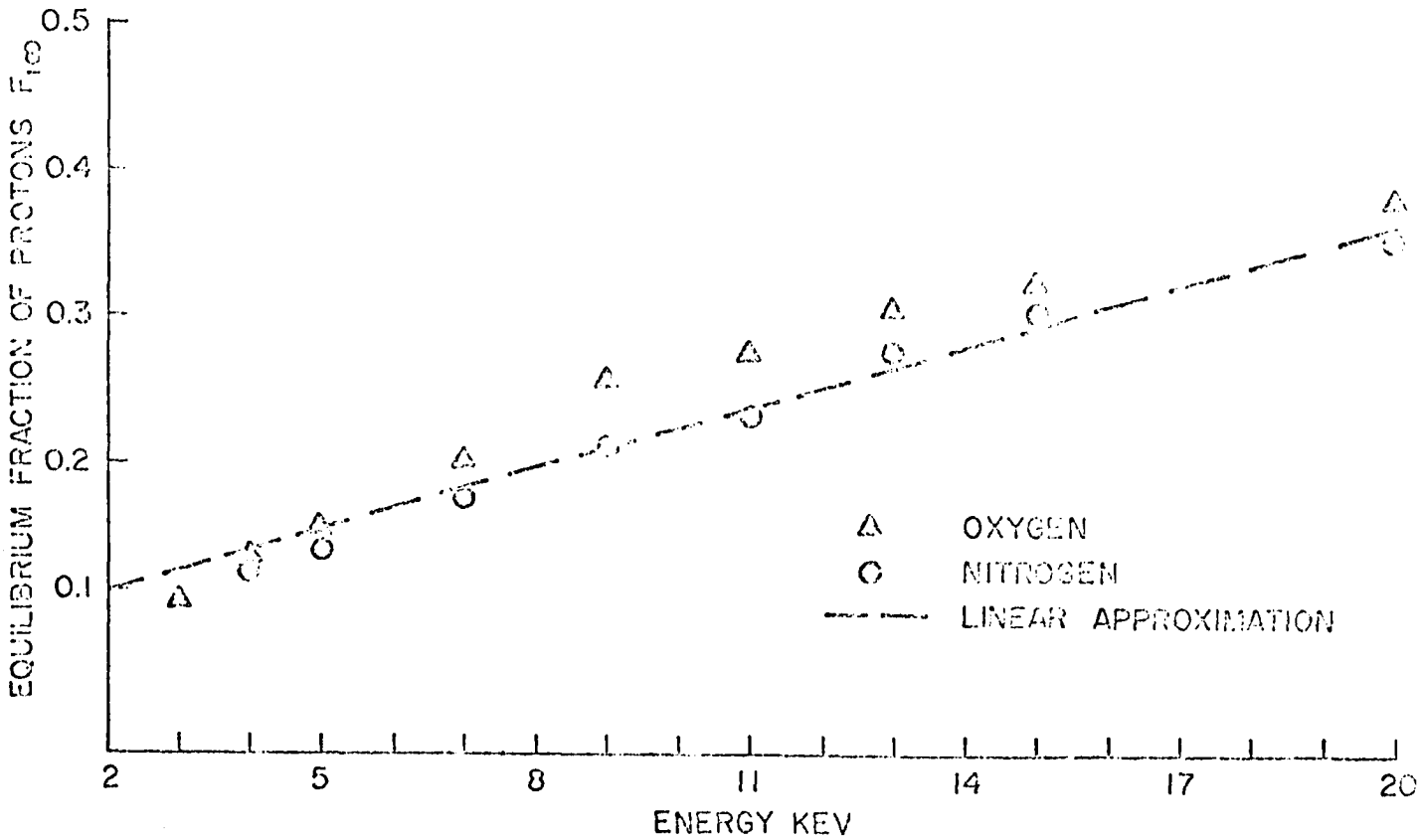

Figure 3.3 Equilibrium fractions of protons in oxygen and nitrogen tabulated by Allison (1958). The dashed line is the linear approximation used to correct the data.

where R is the extrapolated range in standard cms, and k and n are empirical constants. The fit to the experimental data is within 2% except near E_o; some values are shown in Table 3.1.

Table 3.1

Proton Range Energy Relations

Target Gas	k $cm/(kev)^n$	n	E_o(kev)	E_{min}(kev)
Oxygen	3.90	.71	79.0	13.0
Air	3.26	.73	76.5	6.66
Nitrogen	3.34	.71	62.9	6.66

E_{min} is the lowest energy at which a measurement was made. Some extrapolation is required whichever numbers are used. There is no reason to prefer any particular set of these values because none corresponds to the true atmospheric composition. For most of the calculations the values for air have been used. Comparative calculations have been done with the oxygen values.

In the calculations a proton with energy E and pitch angle α at a depth D is related to its primary energy E^1 by the expressions

$$E^1 = (E^n + D/k\cos\alpha)^{1/n} \qquad 3.3.2$$

and

$$dE^1 = (E/E^1)^{n-1}\, dE \quad .$$

These expressions are strongly dependent on α particularly for values near 90°. It is assumed that the pitch angle of an individual particle does not change during its moderation in the atmosphere. This is not strictly valid. The pitch angle changes with altitude because the

magnetic field strength changes. This effect is weakened because the proton spends most of its time as a neutral hydrogen atom. The particle is also scattered in charge-exchange collisions. Some authors (Eather 1967) have argued that the mean scattering angle is only of the order of 0.2°. However, experimental data (Wax and Bernstein 1967) and data presented in Chapter 4 show that protons are scattered more than this. Above an altitude of 200 kms the scattering is apparently not important. Where scattering is important equation 3.3.2 is not valid because the thickness of atmosphere traversed by the particle is no longer given by $(D/\cos\alpha)$.

3.3.4 The calculation. The number of counts per sweep in a particular energy bin I is N(I)

$$N(I) = \epsilon h \frac{dt}{dE_o} \int_o^\infty E\, \tau_I(E)\, A\, (E^n + D/k\cos\alpha)^{-r/n}\, \frac{E}{E^1}^{n-1}\, dE$$

where results from sections 2.3, 2.4 and this section have been used. The assumed primary spectrum has the form

$$n(E) = AE^{-r}$$

and a spectrum of the form

$$n(E) = A\exp(-E/E_1)$$

has also been used. A, r and E_1 are parameters to be varied to fit the data. The integration is performed numerically in steps of 200 ev in energy.

3.4 Results of the computation

3.4.1 The pitch angle distribution is strongly modified by energy loss in the atmosphere combined with a spectrum that decreases in

intensity with increasing energy. Figure 3.4 traces the development of a pitch angle distribution for energy bin 1, initially proportional to $\sin\alpha$, as the beam penetrates the atmosphere. Even at a depth of 0.9 standard cms, corresponding approximately to an altitude of 225 kms, the pitch angle distribution decreases monotonically from 35° to 85°. The result of this is that the correction for atmospheric depth is a sensitive function of pitch angle, and the deduced values of the spectral parameters will depend on the pitch angle distribution assumed.

3.4.2 Exponential and power law spectra produce entirely different forms of the counts versus bin number diagram. Figure 3.5 shows counts/bin for exponential spectra and Figure 3.6 is the comparable plot for power law spectra; the pitch angle is 70°. Also plotted on each diagram is a representative sample of data. It is obvious that no value of the exponential parameter E_1 makes the exponential spectrum fit the experimental data. On the other hand the power law spectrum fits the data well. This result is confirmed if the data are analyzed in the simplified way described in section 3.1 and the spectrum plotted on logarithmic graph paper. The data points lie very close to a straight line.

3.4.3 The calculations were repeated with different values for the parameters in the range-energy relation and the equilibrium fraction to check their effect on the spectral form.

Figure 3.7 compares power law spectra obtained assuming the values of the range-energy relation for oxygen and air. There is a change in intensity but little in the spectral shape. This is expected because

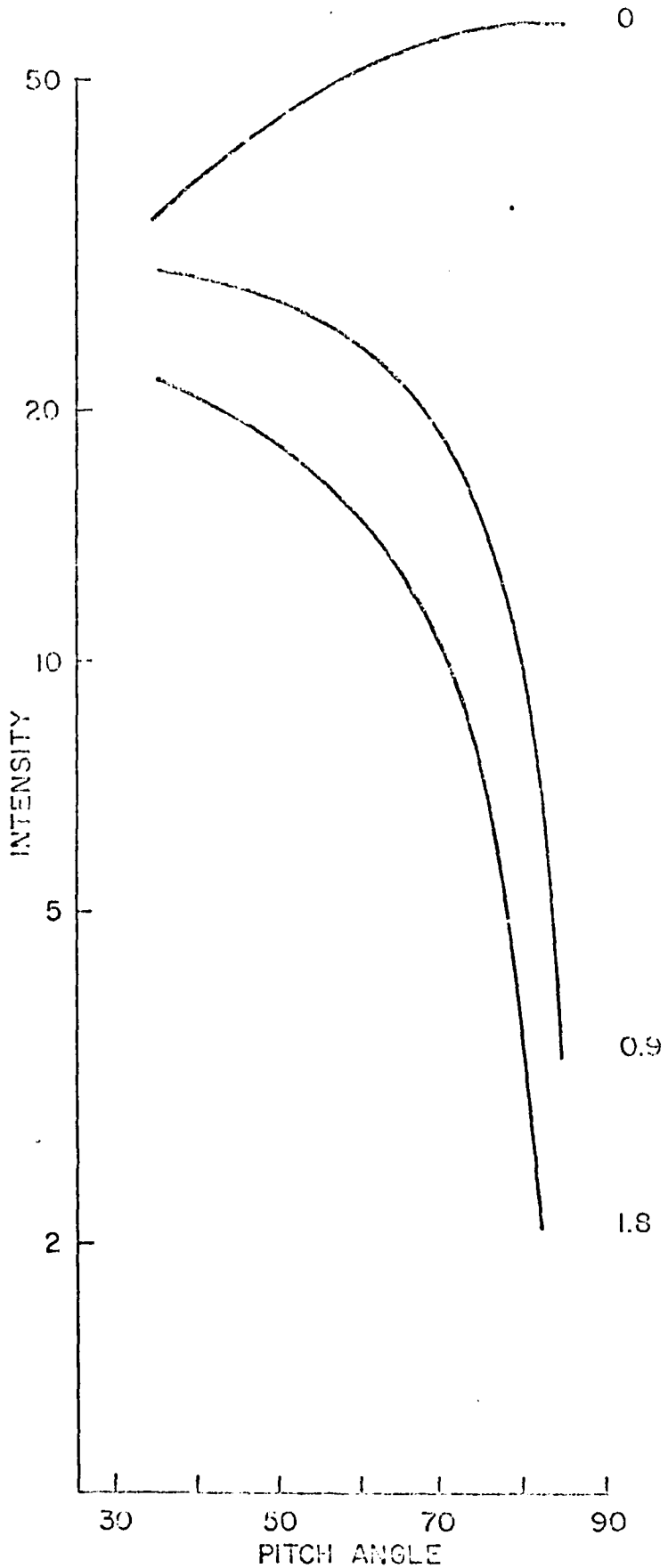

Figure 3.4 A diagram illustrating the variation of a pitch angle distribution as a function of atmospheric depth. [illegible] the atmosphere the intensity is proportional

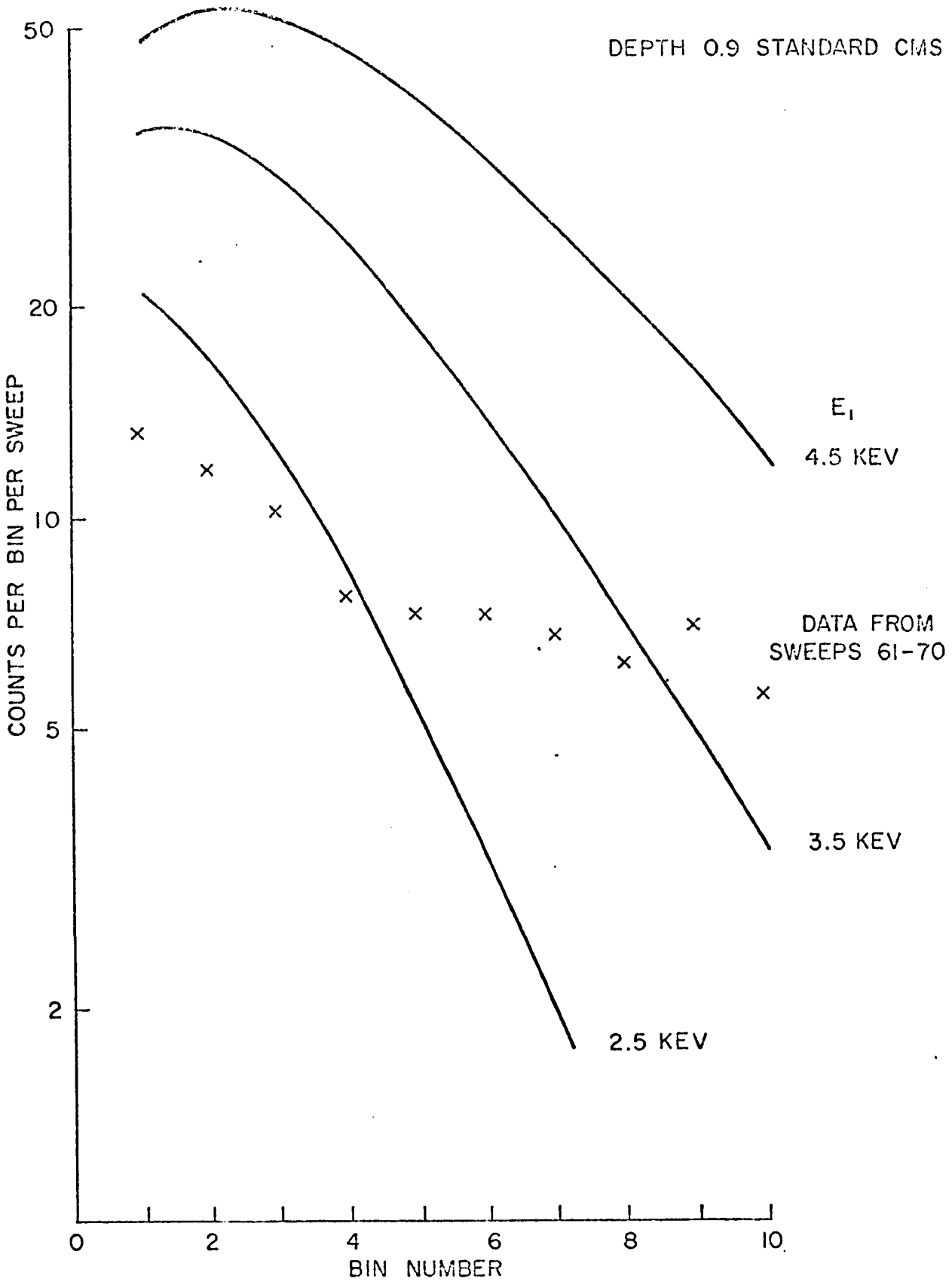

Figure 3.5 Counts per bin for three exponential form spectra compared with a data sample.

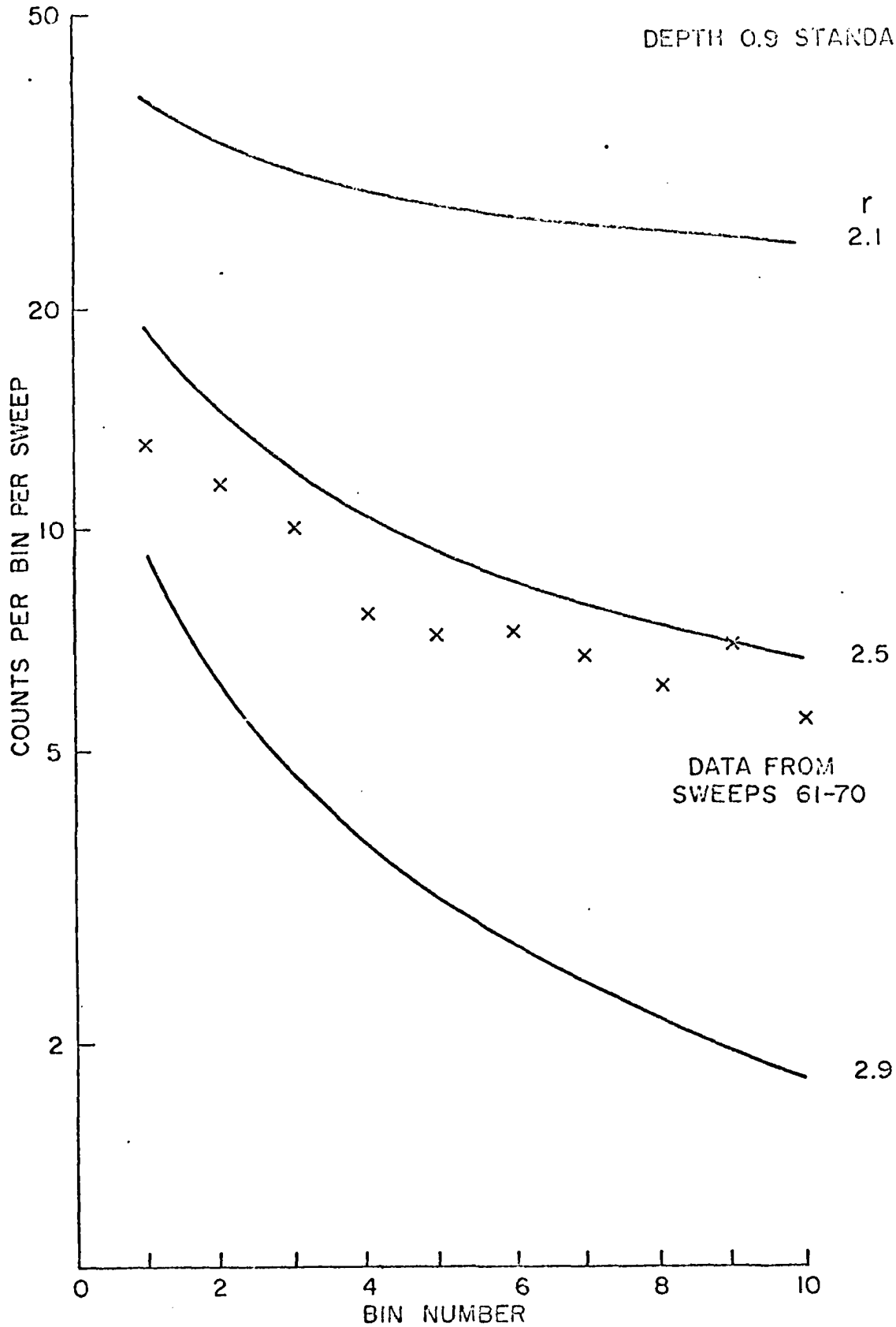

Figure 3.6 Counts per bin for three power law form spectra compared with a data sample.

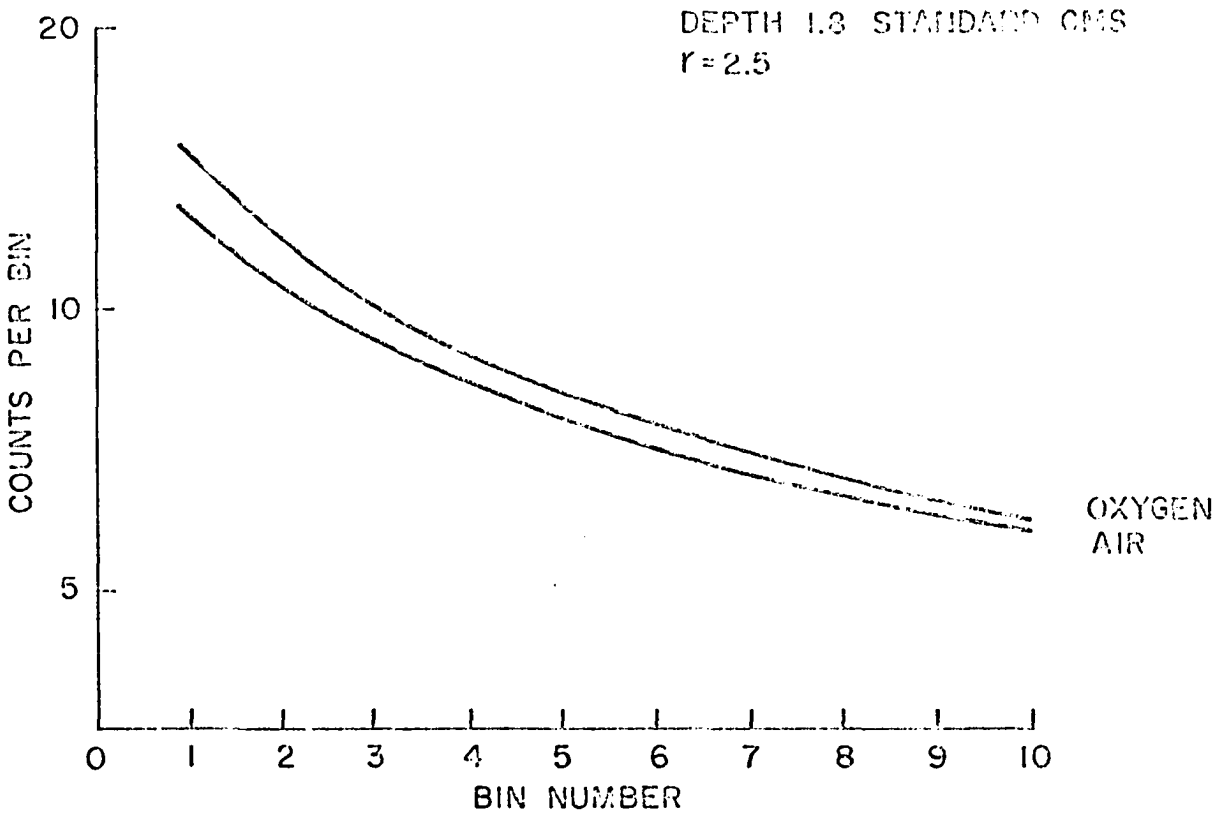

Figure 3.7 Counts per bin for a power law spectrum assuming range-energy relations for oxygen and air.

the range-energy relation has a power law form and there is very little difference between the exponents for the two gases.

Figure 3.8 compares the power law spectra obtained using the equilibrium fraction with the values given in Eq. 3.3.1 and with the equilibrium fraction independent of energy. The spectral exponent is changed considerably but the power law form is still apparent. Again this is obvious because of the quasi-power law form assumed for the equilibrium fraction.

The basic assumptions do not affect the conclusion that the spectrum has a power law form but do introduce some uncertainty in the values of the spectral parameters.

3.5 Values of the Spectral Exponent

A fit parameter has been generated to allow a numerical value to be assigned to the closeness with which the data fit a particular theoetical curve. The curve and the data points are plotted on separate pieces of transparent semilogarithmic graph paper and then overlaid until a close fit is apparent. The distance in millimeters of each point from the line is measured, being reckoned positive if the point is above the line. This distance is proportional to the logarithm of the factor by which the point must be multiplied to make it lie on the line. The relative positions of the data and line are adjusted until the sum of the deviations is zero. Then the deviations are multiplied by a number proportional to their distance from the center of the line. For example the point for bin 1 is -9 units from the center and bin 8 is +5 units away. The fit parameter is the algebraic sum of these moments and is very sensitive to any relative tilt between the points and the theoretical curve. Doing this for several curves near the one that fits best

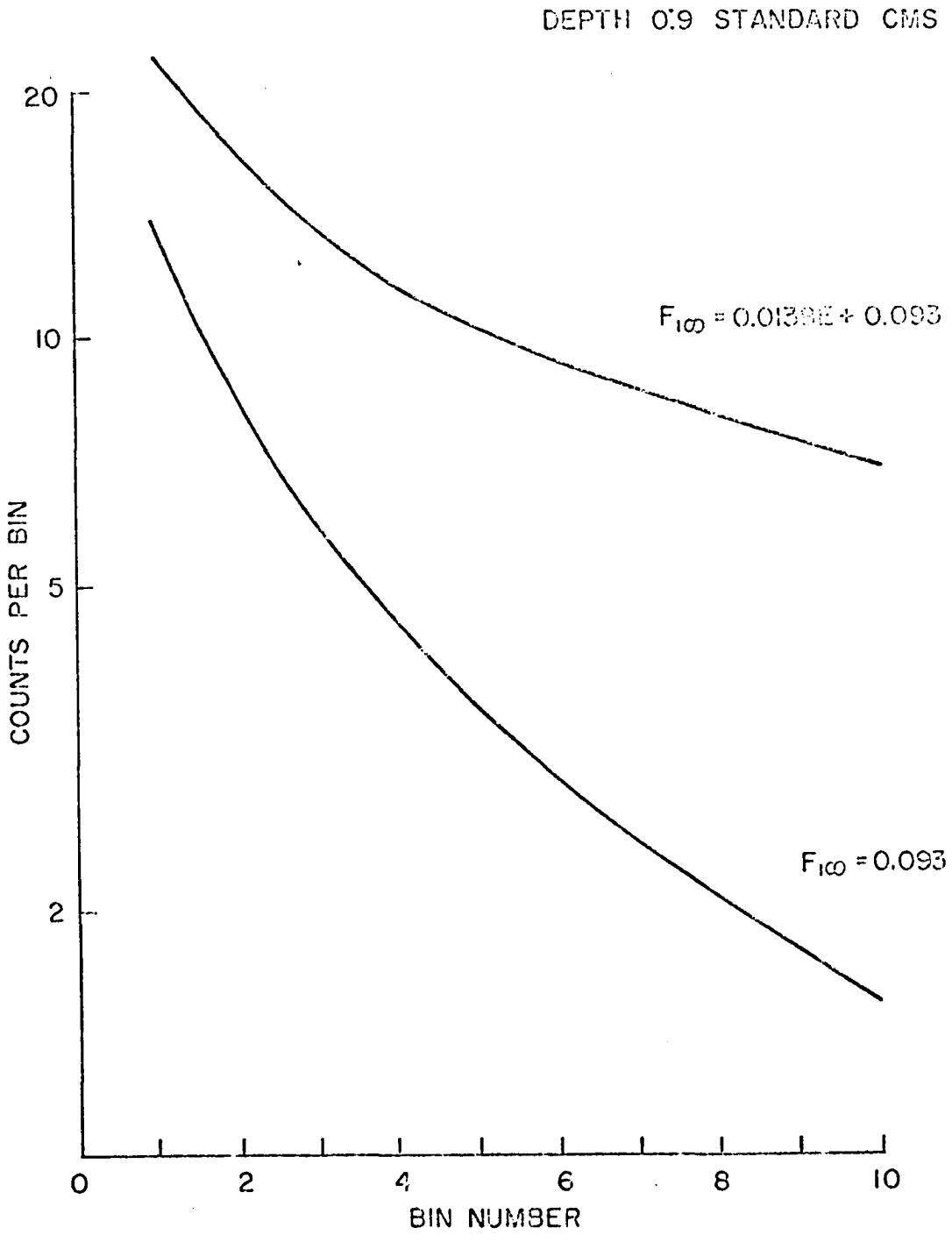

Figure 3.8 Counts per bin for a power law spectrum assuming two different forms for the equilibrium fraction of protons $F_{1\infty}$.

enables interpolation of the exponent between the values at which the computations were carried out. The resultant accuracy is unwarranted because of the uncertainty of the fundamental assumptions in the computation, but the method provides a numerical basis for an otherwise subjective judgement.

The comparisons have been made for data averaged over 10 successive sweeps of the spectrum. The exponents obtained for these 10 sweep intervals throughout the flight are plotted in histogram form in Figure 3.9. There is an altitude variation in the exponent as well as time variations which can be attributed to the time changes shown in Figure 3.1. The depth for which the points are corrected is also shown in Figure 3.9.

There are several possible explanations of the altitude variation

(1) The range-energy relation is incorrect,

(2) The atmospheric model used to make the depth corrections is incorrect,

(3) Pitch angle scattering modifies the effective energy loss rate of the particles with height,

(4) The protons are not in equilibrium,

(5) The spectral exponent increases with increasing primary energy.

The effect of 1, 2, and 3 is to make the actual "depth" of the protons different from the depth for which the correction has been made. However, the spectral exponent increases even if the depth correction is not made, although the correction does enhance the effect.

With regard to 4, it would be surprising if the protons were not in equilibrium at a depth where significant energy loss has been observed.

This leaves as the most likely explanation that the spectral exponent increases with energy. At apogee the detector is measuring particles

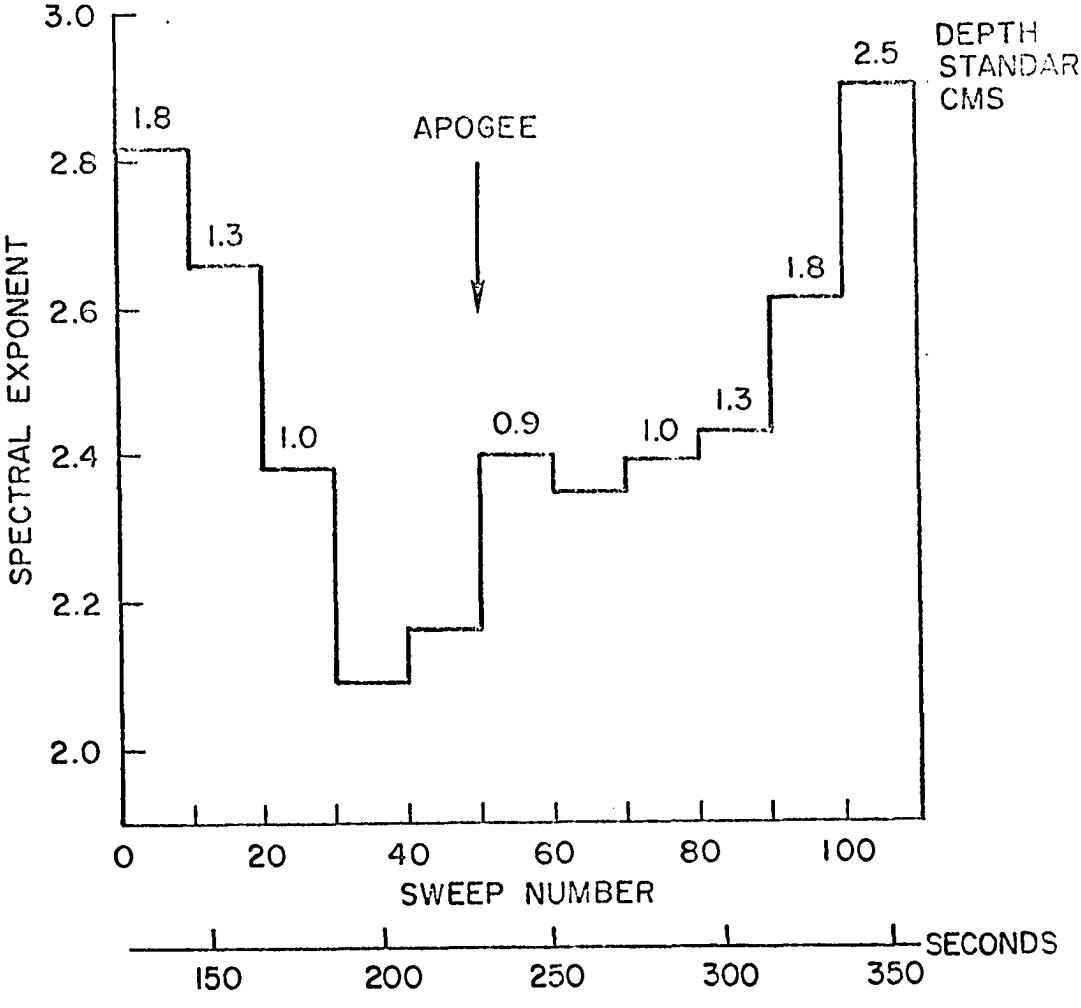

Figure 3.9 The spectral exponent averaged over 10 sweeps throughout the flight. The depth for which the corrections were made is indicated for each point. The altitude variation of the exponent is apparent.

whose primary energies were in the range 4 kev to 26 kev. At 150 kms altitude the corresponding energy range is 10 kev to 35 kev.

The most meaningful measurement of intensity is the local proton intensity, uncorrected for atmospheric absorption or equilibrium fraction and averaged over the local pitch angle distribution. This quantity has been plotted in Figure 3.10 for the lowest energy bin, using 10-sweep totals. Energy bin 1 is the narrowest energy bin, and the implicit assumption of a flat energy spectrum over its width is most nearly justified. The geometric factor of the bin is plotted in Figure 2.9. The relation between the local proton intensities and the primary proton beam intensity cannot be established with any certainty because it depends strongly on pitch angle, range-energy relation, and equilibrium fraction.

3.6 Errors in the Values of the Spectral Parameters

Experimental errors and errors in the fundamental assumptions must be considered. The main sources of experimental error are the statistical fluctuations in the data, the uncertainty in the values of the efficiency of the channel multipliers and the geometric factor of the analyzer. The respective values of the probable errors are estimated to be approximately 10%, 10% and 20%. The last two are systematic errors because they affect all the data uniformly. The combined error is therefore $\pm$ 40% in the local proton intensities. The random error in the spectral exponent is of the order of $\pm$ 0.1 based on visual examination of the fit between data points and theoretical curves. The effect of errors in the fundamental assumptions is harder to assess and depend on the confidence one has in the published experimental data and their extrapolation to the conditions in the upper atmosphere. Based on the calculations performed under different assumptions a limit of $r = -2.4\ ^{+.5}_{-.2}$ is reasonable.

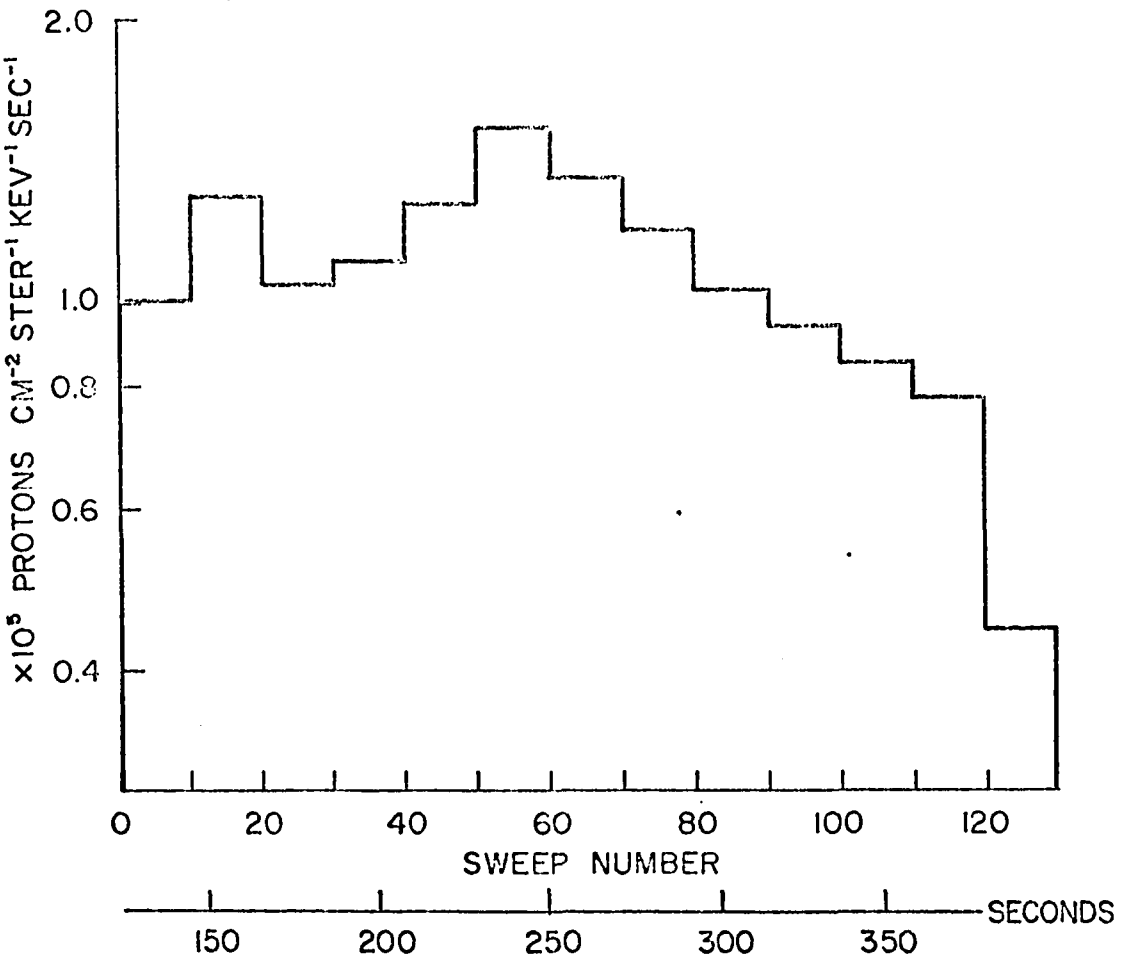

Figure 3.10 The local proton intensity in bin 1 averaged over 10 sweeps throughout the flight.

CHAPTER 4

PITCH ANGLE DISTRIBUTION OF THE PROTONS

It is not possible to find the pitch angle distribution of the protons with any precision because there are too few counts. In the analysis presented here an attempt is made to deduce the qualitative features of the pitch angle distribution; specifically whether it is isotropic or not and, if not, whether the strongest intensities are near 90° or 0°. The pitch angle coverage of the detector is shown in Figure 2.13. It is not a simple function of pitch angle but the diagram shows that the detector covers a wide range of pitch angles from 30° to 100°. The detector samples some particles from more than 85% of the solid angle in the upper hemisphere so that there is some confidence that the data are truly representative of the total flux.

The spin cycle was divided into two equal phases and the counts in each were recorded separately. The relative pitch angle coverage of these two phases is shown in Figure 2.13. The ratio of the counting rates in the two phases is taken as the parameter characterizing the pitch angle distribution. Values of the ratio less than unity indicate pitch angle distributions with greatest intensities near 90°. The value of this ratio is plotted for 5 sweep totals for low energies (bins 1 through 5) and high energies (bin 6 through 10) against altitude in Figure 4.1. At apogee the ratio for high and low energies is significantly less than one. As the altitude decreases the ratio increases as expected because the particles with greater pitch angles are absorbed more readily. It is also obvious from the discussion in section 3.4.1 that even at apogee the value of the ratio is considerably

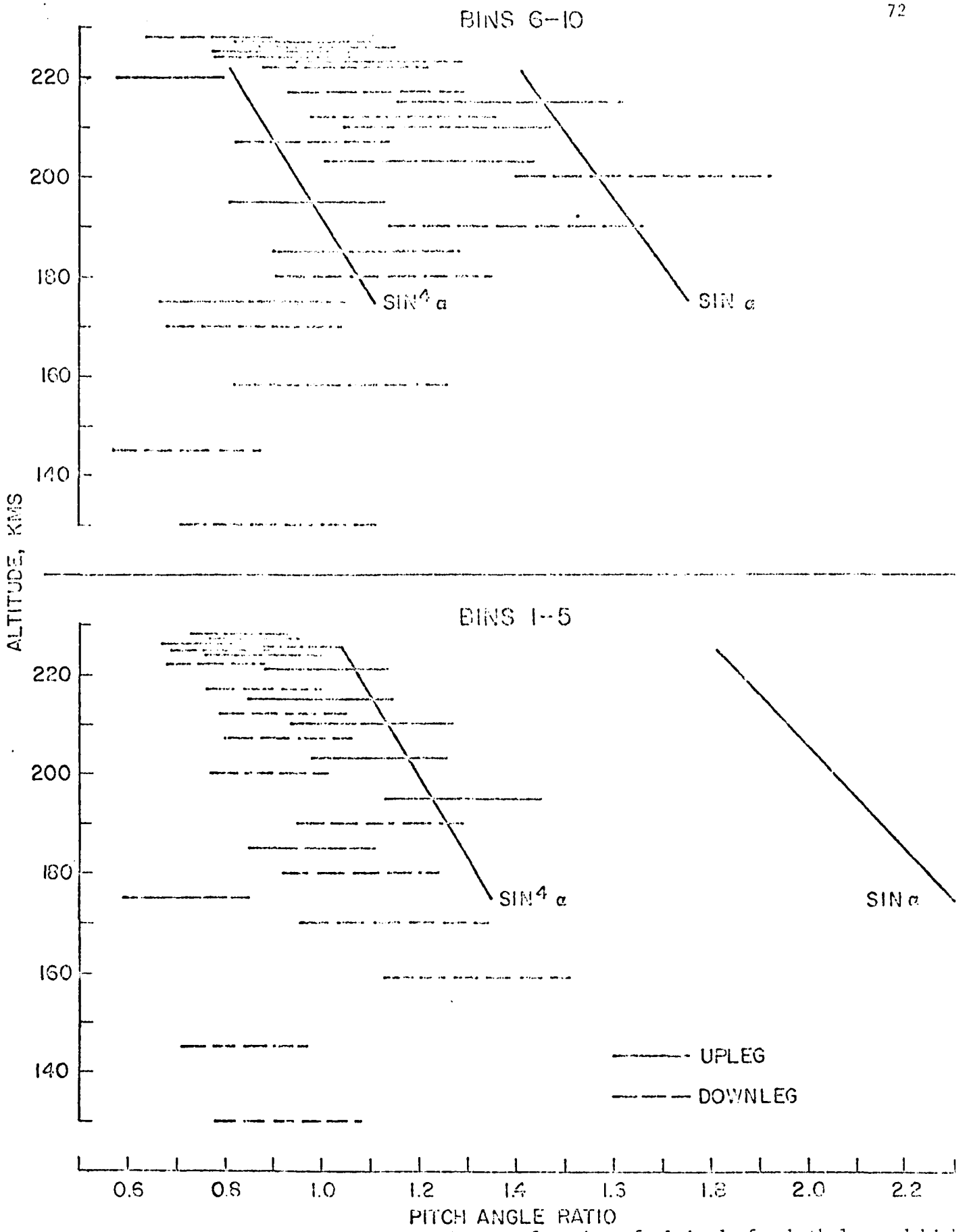

Figure 4.1 The pitch angle ratio as a function of altitude for both low and high energy protons. The length of the lines indicates probable error. Also plotted are the theoretical calculations assuming a primary pitch angle distribution proportional to $\sin\alpha$ and $\sin^4\alpha$.

greater than it would be above the atmosphere. The unexpected feature of the plot is that the ratio reaches a maximum value and then decreases at lower altitudes. Both high and low energy protons show the same effect but the peak in the ratio for the high energy protons is 15 kms higher. The error bars on the points in Figure 4.1 indicate the probable error derived from the number of counts involved in each measurement.

As a check on the significance of this observation the data were reanalyzed, this time splitting the spin modulation into two phases 90° out of phase with the previous ones. The pitch angle coverage of these two phases is identical and the ratio should always be unity unless there is an azimuthal variation in intensity around the rocket. The resultant ratios are plotted against altitude for the same two energy groups. No systematic variation is apparent. The value of the ratio averaged over the whole flight is given in table 4.1.

Table 4.1

"Out-of-Phase" Pitch Angle Ratio

Energy bins	Ratio	Probable Error
1-5	1.05	$\pm$ .029
6-10	1.04	$\pm$ .035

A check on the chart used in the analysis showed that it had a bias that should give an average value of 1.01 for the ratio. The existence of a physically meaningful spin modulation is a further check on the reality of the data (section 2.9).

Some values of the ratio have been calculated issuing the results of the spectrum synthesis calculations. The pitch angle coverage function was approximated in 10° intervals with the values given in Table 4.2. The calculations are unable to predict the intensity at 95° in the lower hemisphere so the intensity was assumed arbitrarily to be the same as at 85°.

Table 4.2

Pitch Angle Coverage

	35	45	55	65	75	85	95
Phase 1	1.4	2.5	3.2	1.8	0.8		
Phase 2			.4	1.4	3.2	3.0	1.7

The ratios for low and high energies were computed for two sample primary pitch angle distributions at two atmospheric depths. The results are tabulated in Table 4.3 and plotted in Figure 4.1.

Table 4.3

Computed Pitch Angle Ratios

Energy Range (bins)	Depth Standard cms	Pitch Angle Distribution	Ratio
1-5	0.9	$\sin \alpha$	1.81
6-10	0.9	$\sin \alpha$	1.42
1-5	1.8	$\sin \alpha$	2.35
6-10	1.8	$\sin \alpha$	1.75
1-5	0.9	$\sin^4 \alpha$	1.04
6-10	0.9	$\sin^4 \alpha$	.81
1-5	1.8	$\sin^4 \alpha$	1.35
6-10	1.8	$\sin^4 \alpha$	1.00

The spectral exponent was -2.3.

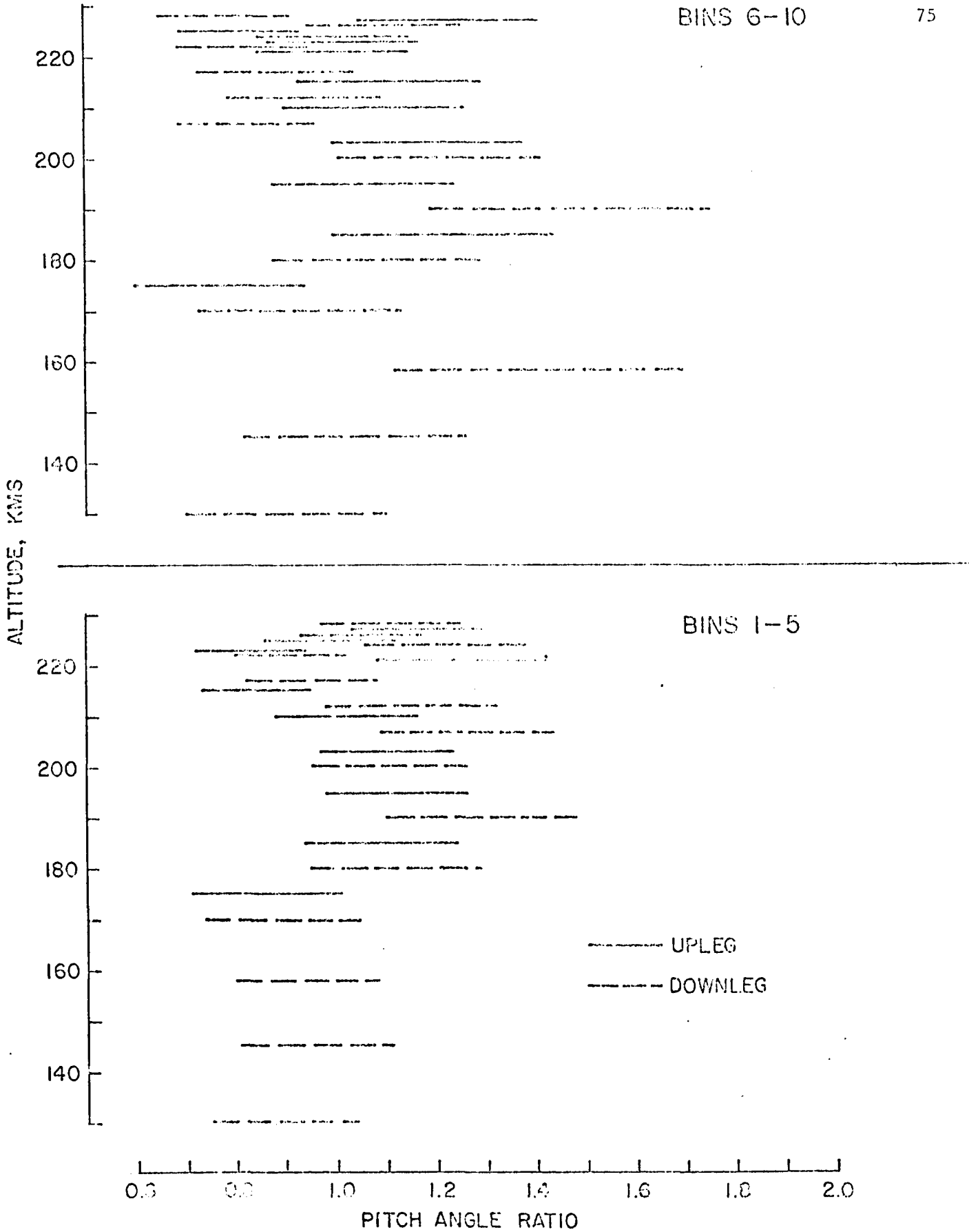

Figure 4.2 The "out-of-phase" ratio as a function of altitude for high and low energy protons.

The rate at which the ratio increases with depth is nearly the same for the calculations and the observed data. This agreement gives added confidence in the pitch angle observations. If a pitch angle distribution of the form $\sin^m\alpha$ is fitted to the data then m is slightly greater than 4 for the low energy protons and less than 4 for high energy protons. The main uncertainty in the value of m lies in the uncertainty of the atmospheric depth of the rocket at apogee. It is obvious that the pitch angle distribution is very "flat". Most of the particles have pitch angles close to 90°.

The decrease in the ratio below 200 kms cannot be explained by absorption alone. Another physical process must also be important. The most likely candidate is pitch angle scattering. The data are consistent with a trend towards isotropy below 200 kms, indicating "strong" scattering. The convergence of the magnetic field lines also increases the pitch angles of all the particles but the magnitude of the effect is so slight as to be negligible. A numerical example shows this. The pitch angle of a particle at 220 kms which mirrors at 100 kms is 87°. The protons spend only about 1/3 of the time with a charge so that the average change in angle is only $1/3 \times 3° \approx 1°$.

Wax and Bernstein (1967) have made measurements of proton scattering in the laboratory which support the hypothesis. They found that the root mean square scattering angle of a proton beam after passing through a carbon foil 2 micrograms cm^{-2} thick is 60/E (kev) degrees for protons in the energy range between 3 kev and 10 kev. This is quite enough to maintain isotropy low in the atmosphere. The thickness of the foil used in the measurement was equivalent to 10 charge-exchange mean free

paths. The atomic number of carbon is close to the atomic numbers of atmospheric constituents so that the experimental data should be relevant.

One feature of the data does not seem to fit the hypothesis. The peak of the ratio for high energy protons is 15 kms higher than that of the low energy protons. The effects of strong scattering are noticed earlier in the high energy protons whereas the scattering angle is iniversely proportional to energy.

The significance of this observation is discussed in section 7.2.

CHAPTER 5

TIME VARIATIONS IN THE PROTON AND ELECTRON FLUXES

5.1 Observations

Proton data for the entire flight have been plotted in Figure 3.1. It shows time variations which cannot be attributed to statistical fluctuations in the count rate although they are not much greater. In particular there are increases in the flux at T + 137, 223 and 243 seconds. The same features are obvious in both the low and the high energy protons. This confirms that there is a change in the particle flux because the two plots are statistically independent. The variations are greater in the low energy proton flux indicating changes in the spectral exponent which have already been noted in Chapter 3. The most striking case was observed at T + 223 seconds. The spectrum averaged over the 10 sweeps preceding this time has an exponent of (-2.1). For the 10 sweeps following the exponent is (-2.5). This represents a considerable softening of the proton spectrum. The total energy precipitated increased.

As far as can be determined with the time resolution available, the changes occur simultaneously in the high and low energy proton fluxes. The high and low energies are observed alternately for 2 seconds each. The changes are always observed in adjacent samples. The maximum time difference between the two energy groups is thus two seconds. If the variation is a temporal variation (section 5.2) limits can be placed on the distance to the source of the modulation. The average energies of the two groups are approximately 8 kev and 19 kev. The maximum time

dispersion Δt is 2 seconds and the maximum distance d to the place where the modulation occurred is

$$d = \Delta t \frac{v_1 v_2}{v_1 - v_2} \approx 7{,}200 \text{ kms.}$$

where v_1 and v_2 are the velocities of the two groups. The distance is measured along the proton trajectory.

There is little evidence for a simultaneous change in the pitch angle distribution. In Figure 5.1 the pitch angle ratio is plotted with the total proton count rate. There is a hint that the ratio increases during the time when the two peaks in the proton flux occur between T + 223 and 250 seconds.

The most interesting feature of the variations is that they correlate with changes in the electron flux. Figure 5.2 shows the 10 kev electron detector counting rate with the low energy proton count rate. There are similar features on both plots although the electrons show much more structure. The 2.5 kev electron detector on the other hand shows none of the variations, and the 5 kev electron detector shows some correlation although weaker than the 10 kev electrons. The event at T + 223 seconds has been analyzed in some detail because the correlation is most striking. It is shown in Figure 5.3. Before the increase the spectrum above 5 kev can be characterized by a power law spectrum with an exponent of -0.9. After the increase in flux the exponent is -0.4, a considerably harder spectrum. At 5 kev there is very little change in the counting rate. In summary, when the electron spectrum hardens the proton spectrum softens. Associated with these spectral changes there is an increase in the precipitated energy of both electrons and protons.

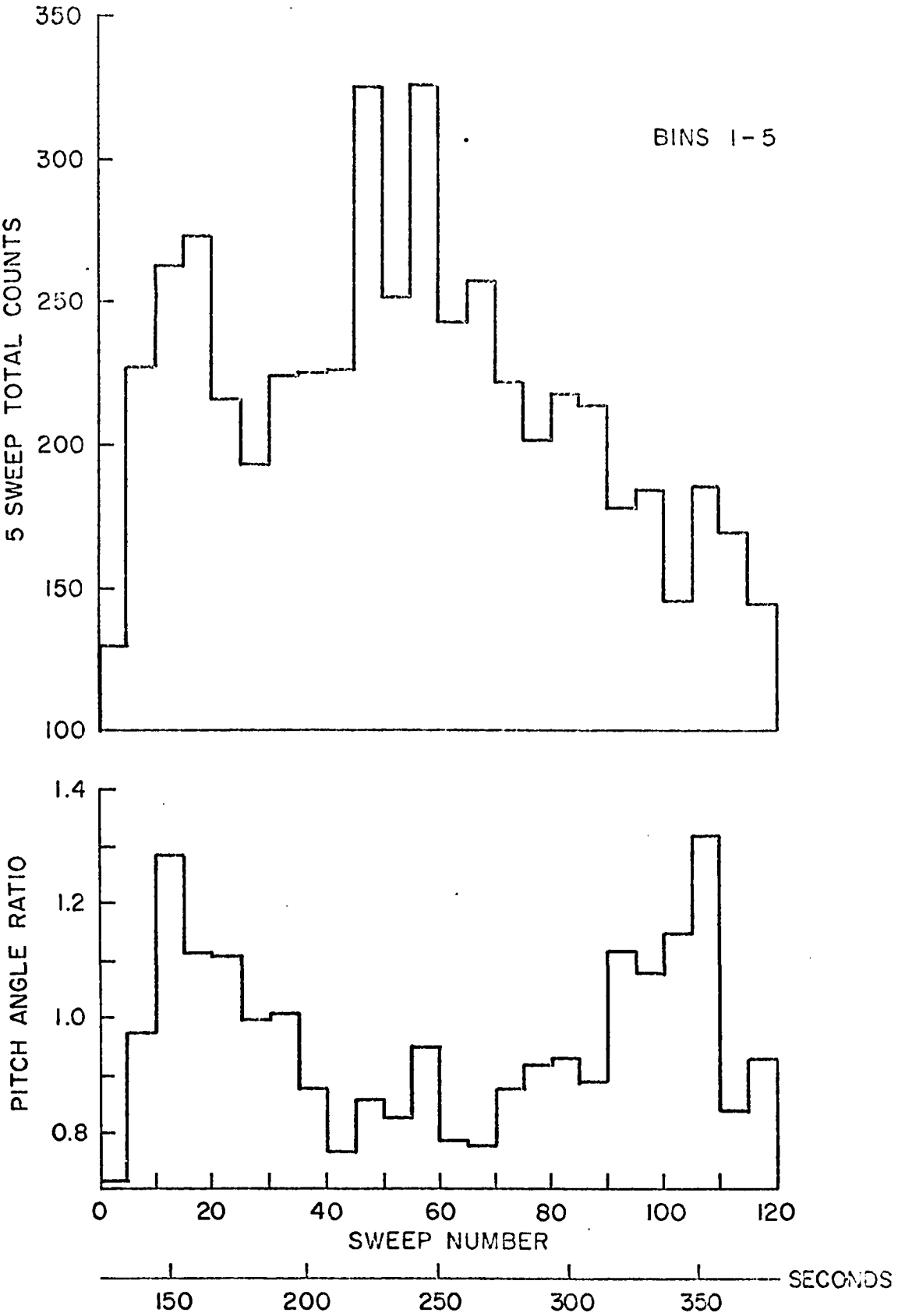

Figure 5.1 The pitch angle ratio and the proton count rate in bins 1 through 5 plotted together. The altitude variation of the pitch angle ratio is apparent in this diagram.

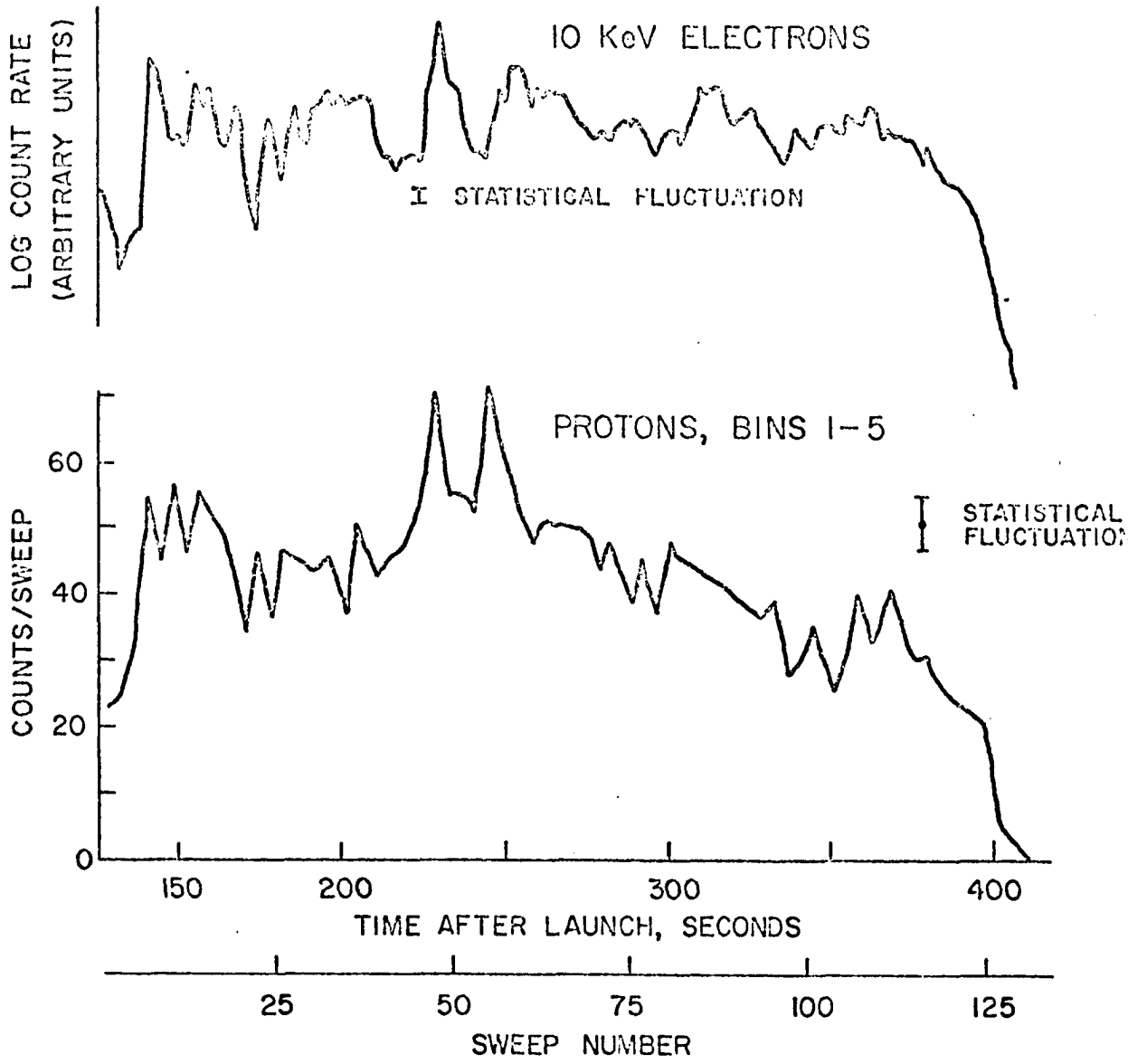

Figure 5.2 The low energy proton counting rate compared with the 10 kev electron counting rate through the flight. Note that the electron ordinate is logarithmic while the proton ordinate is linear.

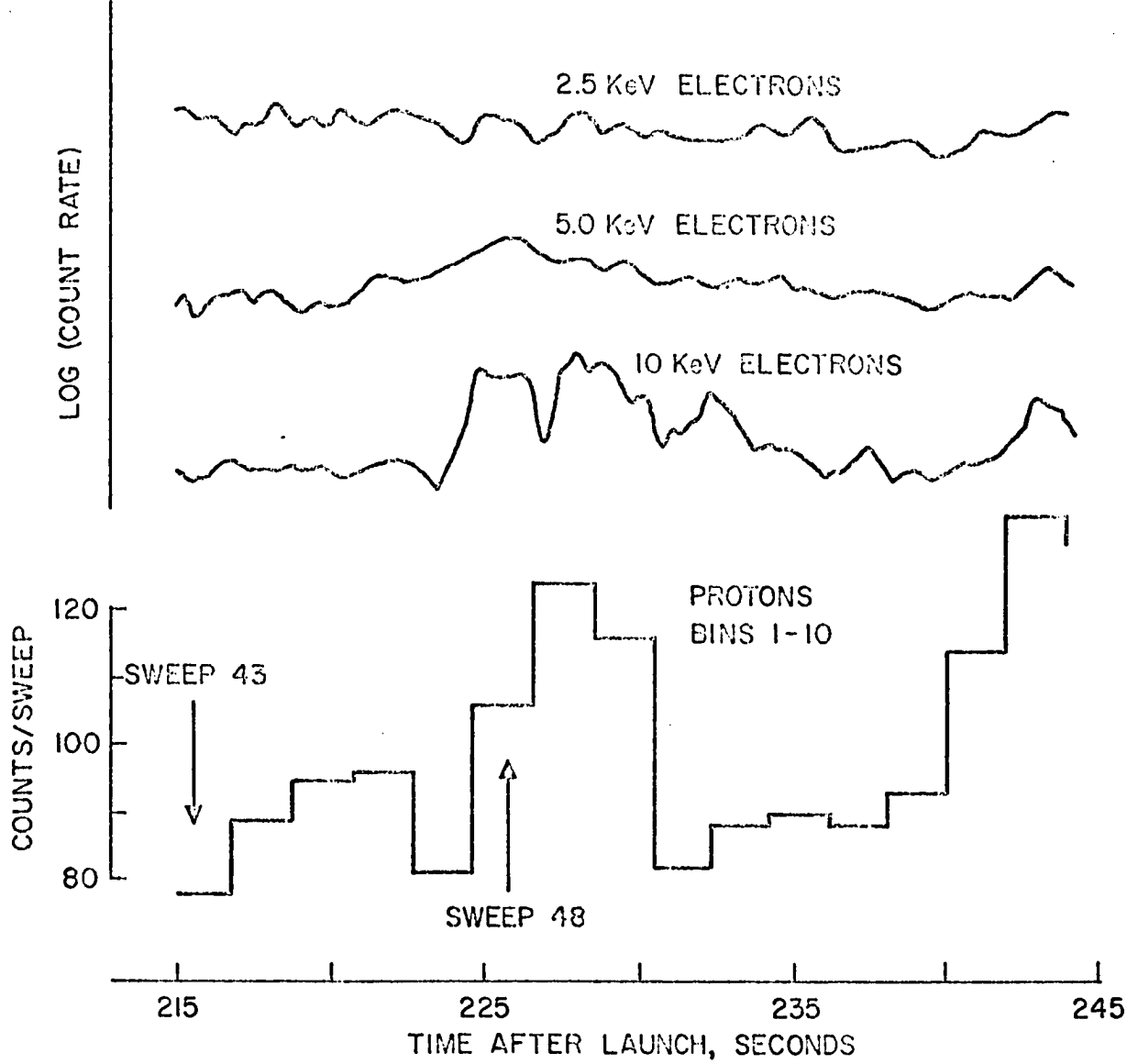

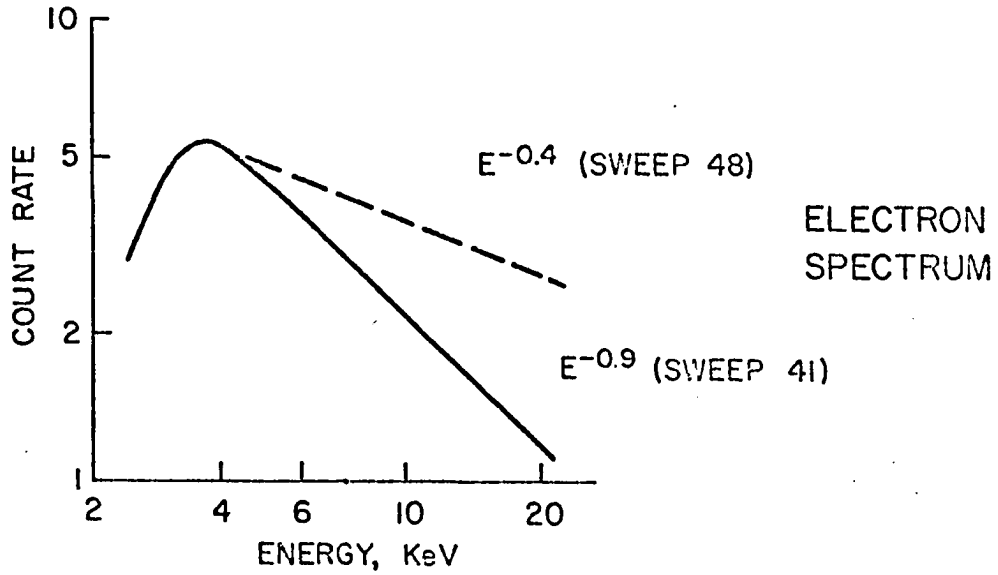

Figure 5.3 The counting rates of the particle detectors during the event which started at T + 223 secs. The electron counting rates are plotted on a logarithmic scale and the proton count rate is plotted linearly. The electron spectra before and during the event are shown.

If the electrons and protons are modulated as part of the same process, the time dispersion between them can also be used to find the source. The dispersion is less than two seconds, setting an upper limit on d of 2500 kms.

5.2 Temporal and Spatial Variation

If the data are going to be interpreted correctly one must know whether the time variation seen by the rocket was a temporal or spatial variation in the aurora. There are three cases to be distinguished.

(1) When there is an increase or decrease in the precipitating flux occurring simultaneously over a region of space occupied by the rocket it is a temporal variation,

(2) When the rocket enters an auroral form which has maintained its brightness and position the variation is spatial,

(3) When a moving auroral form passes the rocket it is not clear whether the variation should be classified as temporal or spatial. If the movement of the form is caused by the convective drift of a tube of force within which the precipitation is occurring, then the effect is essentially spatial. If the movement is caused by the propagation of a precipitating agent, such as an electromagnetic wave, across the magnetic field, then the effect is temporal. In other situations the distinction is not clear. For example, it is not obvious whether small-scale folds and curls (Hallinan and Davis, 1970) are temporal or spatial.

The main interest in knowing whether the variation is temporal or spatial lies in interpreting time shifts between different velocity particles in terms of the distance to the source of the modulation. If this distance is known it may be possible to deduce the mechanism.

In principle the ambiguity can be resolved by making visual observations of the aurora and the rocket. This was done during this flight but the rocket is 100 kms above the aurora and unless both rocket and corresponding aurora are in the magnetic zenith of the observer it is almost impossible to relate the rocket measurements to the auroral observations. This is particularly difficult when the aurora is as widespread and structured as it was during the flight. No structure has been found to relate to the measurements here. A meridian scanning photometer was operated making observations of a number of auroral emissions including the hydrogen beta line. One meridian scan was completed each twenty seconds so that there were not enough data to follow temporal variations. No significant spatial variations were observed in the neighborhood of the rocket. The inherent noise level in the photometer was relatively high because the hydrogen emissions were very weak, so that changes of 50% in brightness over a small region might have been missed.

There is an added interest in resolving the ambiguity for the protons because a narrow proton beam should be spread by the effects of charge-exchange. The neutral hydrogen atoms are not constrained to spiral around lines of force and so may travel large distances across the magnetic field. The particles maintain their pitch angle while neutral hydrogen so that those with large pitch angles may move considerable distances. Davidson (1965) made a calculation of the amount of spreading using the Monte Carlo method. He concluded that a narrow arc-like structure in the primary proton beam would produce a visible form 2° of latitude thick. Thus the edge of any proton structure, when observed low in the atmosphere, should appear to be of the order of

100 kms thick. If the scale size of the observed structures is calculated from the time scale and the horizontal velocity of the rocket, values near 2 kms are obtained. In comparison, the gyroradius of a 10 kev proton with a pitch angle of 90° at auroral altitudes is 270 meters. The observed thickness is about 10 gyroradii. If Davidson's calculations are correct, it is unlikely that the variation was spatial. It can be argued, however, that the atmospheric structure was not the same as in the model used by Davidson. If the atmospheric depth at an altitude of 220 kms is much less than has been estimated, then a significant fraction of the primary protons will not have made a charge-changing collision and will reflect the primary structure. It is not clear from Davidson's calculations how the spreading is affected by different atmospheric structures since only one model atmosphere was used. Additional insight can be gained from an analysis of the spreading of a proton beam to find out how atmospheric structure affects the width of the beam.

5.3 Spreading of a Proton Beam

The path of an alternately neutral and ionized hydrogen atom through the atmosphere consists of straight and spiral segments. Projected in the horizontal plane the segments are randomly oriented with respect to each other. The movement of the particle over the horizontal plane is a random walk. As the particle penetrates deeper into the atmosphere the straight segments become shorter because the mean free path decreases owing to increased density. Each atmospheric scale height that the particle penetrates causes the average length of the segment to decrease by a factor 1/e. The first straight segment, occurring

after the first charge-exchange collision made by the proton, has most effect on the spreading of the beam and will set the scale of the spreading. Subsequent segments increase the total spreading but cannot change the order of magnitude. The distribution of lengths of the first step for all particles is expected to be related to the atmospheric scale height at the altitude where the proton makes its first collision. In the analysis below the relationship is calculated.

Let $P_i(x_1:x_2)$ be the probability that a particle in charge state i goes from x_1 to x_2 without making a charge-exchange collision. The probability it will make a collision in an element of length dx is proportional to ndx., where n is the atmospheric density. In the atmosphere

$$n = n_o e^{-x/L}$$

where L is the atmospheric scale height, assumed here to be a constant. If λ_i is the mean free path between charge-exchange collisions for particles in charge state i at x = 0 then the probability of a collision is

$$\frac{e^{-x/L} dx}{\lambda_i}$$

For a reason that is apparent below, the origin for x is set at a point which the proton has a negligible chance of reaching without a collision. Therefore λ_i is a very small quantity if the origin for x is put at ground level.

If the particle is traveling in the negative x direction

$$P_i(x_1:x_2 + dx) - P_i(x_1:x_2) = P_i(x_1:x_2) \frac{e^{-x_2/L} dx}{\lambda_i}$$

Therefore by integration

$$P_1(\infty:x_1) = e^{-L/\lambda_1 e^{-x_1/L}} \qquad \text{if } P_1 = 1 \text{ when } x = \infty$$

and $$P_o(x_1:x_2) = e^{\frac{L}{\lambda_o}\left(e^{-x_1/L}-e^{-x_2/L}\right)} \qquad \text{if } P_o = 1 \text{ when } x = x_1$$

The probability of a particle starting at infinity making a collision $1 \longrightarrow 0$ in dx_1 and subsequently $0 \longrightarrow 1$ in dx_2 is

$$P_1(\infty:x_1)\ \frac{e^{-x_1/L}}{\lambda_1}\ dx_1\ P_o(x_1:x_2)\ \frac{e^{-x_2/L}}{\lambda_o}\ dx_2$$

Put $x_2 = x_1 - \ell$

$dx_2 = - d\ell$

then the probability of a path length ℓ as a neutral is $p_o(\ell)$. Suppressing the suffix on x and putting

$$A = -\frac{L}{\lambda_o}\left(e^{\ell/L} - 1\right) - \frac{L}{\lambda_1}$$

$$p_o(\ell) = -\frac{e^{\ell/L}}{\lambda_o\lambda_1}\int_{\infty}^{o} e^{-2x/L}\ e^{Ae^{-x/L}}\ dx$$

$$= \frac{e^{\ell/L}}{\lambda_o\lambda_1}\ \frac{L}{A}\left(e^A - \frac{1}{A}\ (e^A - 1)\right)$$

A is always negative and $\lambda_o, \lambda_1 \ll L$ if the origin is sufficiently remote. Therefore e^A is a very small quantity and may be ignored in comparison with 1 or 1/A. Putting $\ell = nL$ to obtain a dimensionless form

$$p_o(n) = \frac{m\, e^n}{(m-1+e^n)^2}$$

where $m = \lambda_o/\lambda_1 = \sigma_{10}/\sigma_{01}$

The only energy dependence of the expression is through the ratio m. At 3 kev $m \gtrsim 9$, at 5 kev $m \gtrsim 5$ and at 25 kev $m \gtrsim 1.5$. Figure 5.4 shows $p_o(n)$ for these three values of m.

The average path length is <n>

$$\langle n \rangle = \frac{m}{m-1} \log_e m$$

which is shown in Figure 5.5 as a function of energy. It is of the order of unity.

For a particle with a pitch angle α, the effective scale height is $L/\cos\alpha$ and the horizontal distance the particle moves is therefore $\langle n \rangle \sin\alpha(L/\cos\alpha) = \langle n \rangle L \tan\alpha$. Some typical values of L are given by Anderson and Francis (1966). At altitudes between 200 kms and 400 kms L ranges from 36 kms to 86 kms depending on time of day and solar activity. The horizontal spread of a proton beam, only a few mean free paths deep in the atmosphere, is of the order of tens of kilometers at least. The spreading is greater for large pitch angles so that measurements on the extreme edge of a proton structure should have a "flatter" pitch angle distribution.

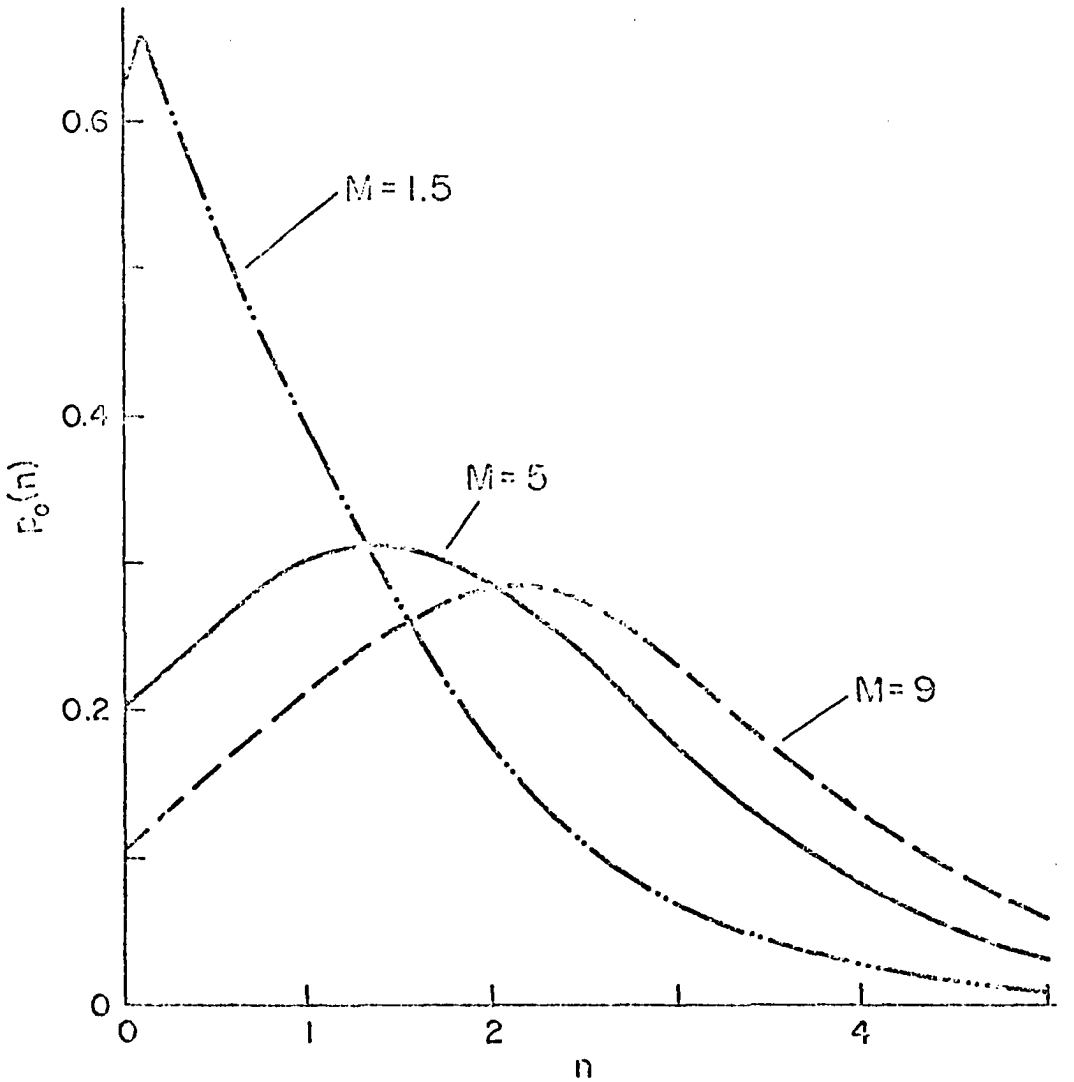

Figure 5.4 The probability $P_o(n)$ that the first neutral hydrogen segment of a proton in the atmosphere will be of length n where n is in units of the local scale height.

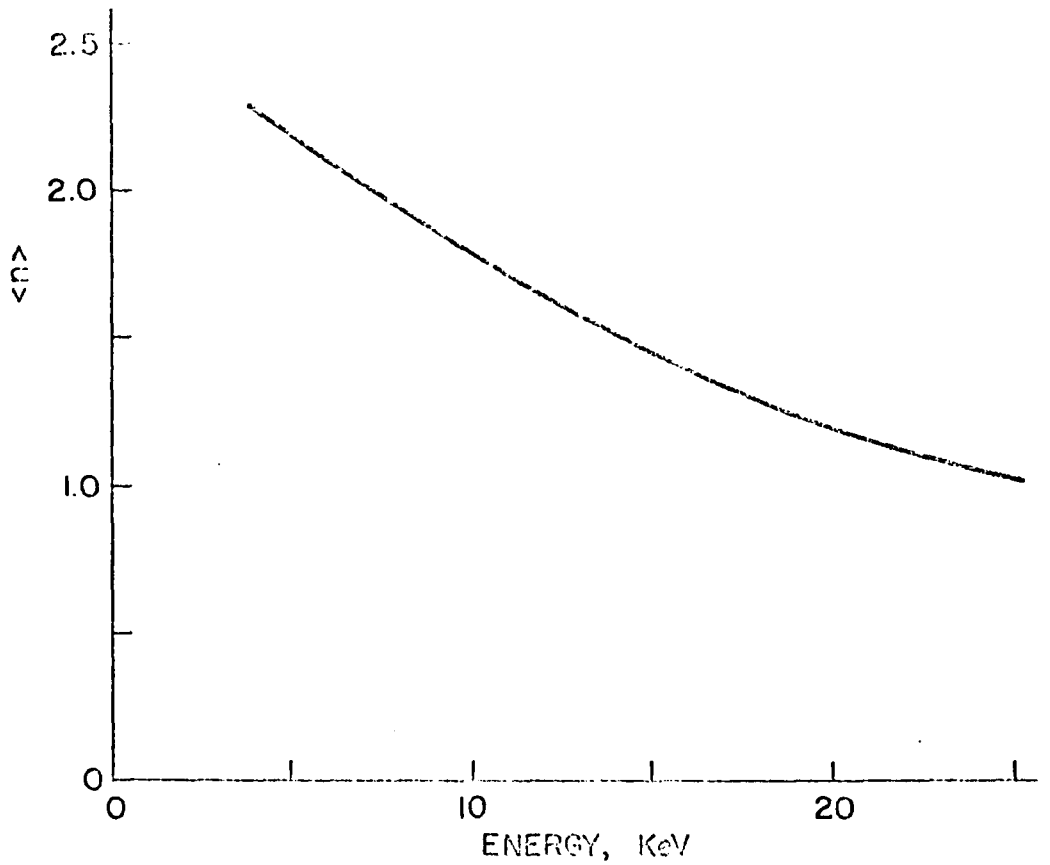

Figure 5.5 The average length of the first neutral hydrogen segment < n > in units of local scale height as a function of proton energy.

5.4 Discussion

The analysis of the preceding section shows clearly that under normal circumstances spatial structure with a scale size of 2 kms will not be observed. There are a few possible explanations of the way a small-scale structure might be generated.

(1) The rocket may have been close to the edge of a much larger change in intensity with a thickness of 50 kms or more. A change like this would have been observed by the scanning photometer, but none was seen. In addition, the pitch angle ratio should decrease in the structure. In fact, if anything the ratio increases.

(2) The rocket may have been high enough to detect protons that had not made any charge-exchange collisions. The rocket would need to be only a few mean free paths deep in the atmosphere. On another occasion a significant flux of neutral hydrogen atoms was observed at 250 kms (Bernstein et al. 1969), which is above the apogee of rocket 18.15. It would be hard to explain the increase at T + 135 on this basis. It occurred at an altitude of 180 kms and it is known from the pitch angle data that significant absorption had occurred above that altitude.

(3) The spatial structure may have been generated close to the rocket in a region where the mean free path is relatively small. The subsequent spreading would have a scale size of the order of the local mean free path. Any electromagnetic mechanism operating at low altitudes like this would be inefficient because only a small fraction of the particles is charged.

Bernstein et al (1969) have also observed a time variation in the neutral hydrogen flux in an aurora. In the example they describe a decrease in the neutral hydrogen and electron fluxes was seen at the time the rocket passed through the boundary of a bright auroral form. It would seem to be spatial structure although the small scale size is difficult to explain.

Although the simple explanations of small-scale structure have been eliminated it is possible that it has a more exotic cause. In this case, however, the evidence is in favor of a temporal variation as the simpler hypothesis. If this interpretation is correct the time variations observed may correspond to pulsating effects observed to be occurring during the flight. Then the particle flux measurements indicate that the protons are also pulsating though with smaller changes in energy flux than the electrons (section 6.1).

CHAPTER 6

ENERGY DISSIPATION IN THE SUBSTORM

6.1 Energy in Particle Precipitation

Particle precipitation is one way in which the substorm energy is dissipated. Another way, not discussed here but equally important, is the Joule heating associated with ionospheric currents. In this section the electron and proton energies are integrated over the spectrum and pitch angle distribution to obtain the energy flux into the atmosphere. Unfortunately the measurements of both the spectrum and pitch angle distribution are incomplete, but they enable a lower limit of the energy flux to be calculated. It is hoped that this represents the greatest portion of the energy flux. Some extrapolations have been made to give more meaningful comparisons, and by comparing the resultant energy fluxes with observations of the emitted light, it is shown that most of the energy has been accounted for.

Most of the pitch angle distribution is covered by the measurements (Chapter 4) but the pitch angle distribution is not accurately known. In the calculations it is assumed that the average intensity measured is representative of the intensity averaged over the pitch angle distribution. The average pitch angle, required to correct the proton intensities, is assumed to be 70°.

The energy flux is not constant so that two calculations are made at times in the flight when the energy flux is a minimum and a maximum, before and after the increase in particle fluxes at T + 223 secs respectively. As this was near apogee the correction to the proton intensity is a minimum.

6.1.1 Precipitated proton energy

The proton spectrum is

$$n(E) = AE^{-r} \qquad 6.1.1$$

The exponent r and the proton intensity in bin 1 are given in Chapter 3. The spectral coefficient A is obtained by the following procedure. The average energy of bin 1 is 4 kev. A 4 kev proton with a pitch angle of 70° at an altitude of 225 kms (depth 0.9 standard cms) had a primary energy of 5 kev. The proton intensity in bin 1 is corrected for the equilibrium fraction at 4 kev and used in equation 6.1.1, with the value of E set at 5 kev.

The energy flux ϕ_p is obtained by integrating the spectrum over energy and pitch angle

$$\phi_p = \int\int 2\pi AE^{-r+1}\sin\alpha\cos\alpha\, d\alpha\, dE = \frac{\pi A}{-r+2}\left|E^{-r+2}\right|_{E_1}^{E_2} \qquad 6.1.2$$

The energy limits, E_1 and E_2, for the energy range measured are 3 kev and 30 kev. It is fairly certain that the proton spectrum extends to lower energies (Bernstein et al 1969) so the energy between 1 kev and 3 kev has been calculated separately by extrapolating the spectrum. The energy flux above 30 kev for the spectrum extrapolated to infinity has also been calculated. The results are shown in Table 6.1. The energy flux above 30 kev is not expected to be different in the two cases because the intensity at 30 kev does not change at T + 223 sec. The lower value of .13 ergs is more likely to be accurate because the spectral exponent decreases at high energies (section 3.5).

Table 6.1

Proton Energy Flux

Time	Spectrum	Energy flux ergs $cm^{-2} sec^{-1}$ 1 kev-3 kev	3 kev-30 kev	Above 30 kev
Sweeps 37-46	$2.5 \times 10^7 E^{-2.1}$	.13	.23	.88
" 48-57	$7.2 \times 10^7 E^{-2.5}$	.31	.29	.13

Figure 6.1 shows a sample of raw data from the scanning photometer which made a south-north scan along the magnetic meridian (approximately the plane of the trajectory) in ten seconds. The hydrogen beta emission is essentially uniform, the only significant variation being caused by the variation of optical path length through the aurora with zenith angle. The intensity is approximately 70 Rayleighs (W. Stringer, private communication). According to these measurements it requires between 8.5 and 10.5 ergs cm^{-2} sec^{-1} of proton energy to produce 1 kiloRayleigh of H_β emission. Eather (1967) has derived a value of 16 ergs cm^{-2} sec^{-1} per kiloRayleigh from experimental cross-section data, suggesting that the proton energy flux has been underestimated slightly here.

6.1.2 Precipitated electron energy. The same normalization procedure has been used to obtain primary electron intensities except, of course, that no correction is necessary for atmospheric absorption or equilibrium fraction. The data show that the intensity decreases rapidly below 3 kev so the spectrum has not been extrapolated below 3 kev. The energy flux above 30 kev has not been calculated either because the extrapolated spectrum diverges at infinity. Other measurements above 30 kev summarized by Whalen and McDiarmid (1969) show that there are relatively few high

energy electrons. They give an average exponent for the spectral data of -8.5 above 30 kev. The electron energy fluxes are tabulated in Table 6.2.

Table 6.2

Electron Energy Flux

Time	Spectrum	Energy Flux (ergs $cm^{-2}sec^{-1}$) 3-30 kev
Sweep 41	$7.7 \times 10^{7} E^{-0.9}$	6.8
Sweep 48	$3.8 \times 10^{7} E^{-0.4}$	13.5

From the scanning photometer data (Figure 6.1) the range of intensity of the 3914Å emission was 5 kiloRayleighs to 10 kiloRayleighs. Dalgarno et al (1965) have calculated the production ratio of this emission line, excited only by particle bombardment, as 1.2 ergs $cm^{-2}sec^{-1}$ per kiloRayleigh.

6.2 Extent of the Precipitation

From all-sky camera and riometer measurements in Alaska during the substorm in which the rocket was launched, it is known that the average electron precipitation was uniform over a region extending from Anchorage in the south to Barter Island in the north and from 300 kms west of Bettles to a point 300 kms east of Tok (Fig. 1.2). The area of this region is of the order of 10^{16} cms^{2}. The substorm started at 12.10 UT and the precipitation continued at the level observed during the flight for about one hour. Thus 3.6×10^{20} ergs were precipitated over Alaska. If it is assumed that the conjugate aurora in the southern auroral zone was equally intense the total precipitated energy was approximately 7×10^{20} ergs.

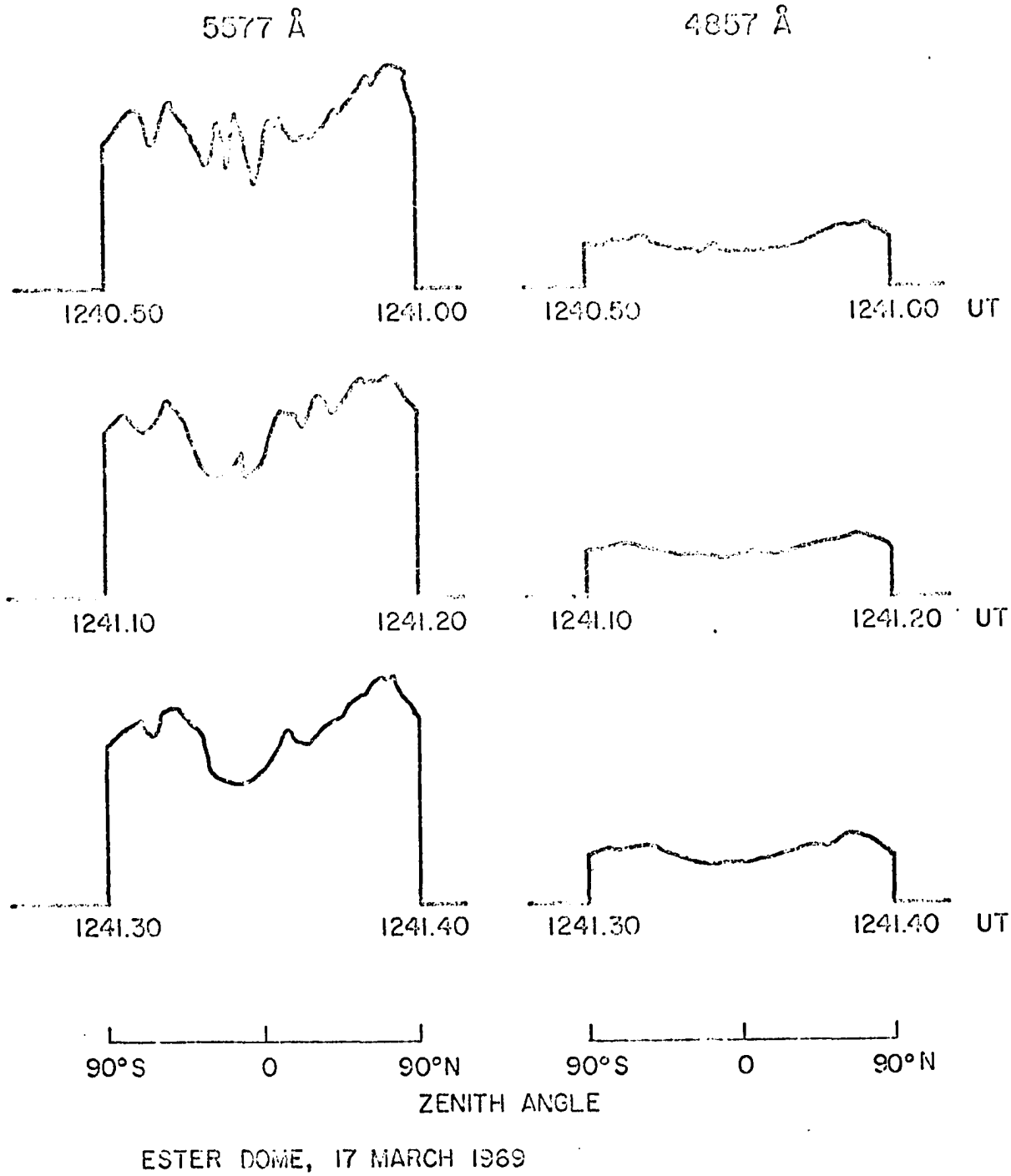

Figure 6.1 Three successive scans of the scanning photometer made at Ester Dome near College. The ordinate is proportional to log (intensity). The two emissions do not have the same ordinate. The 5577Å emission is excited primarily by electron precipitation and the 4857Å emission by proton precipitation alone.

In Figure 6.2 the equatorial magnetic disturbance D_{st} is shown for the March 17, 1969 (K. Kawasaki private communication). During the substorm D_{st} drops from -27 γ to -33 γ. According to the formula given by Sckopki (1966) the ring current energy (mainly protons) has increased from 0.9×10^{22} ergs to 1.1×10^{22} ergs.

During the main phase of the magnetic storm which began with a sudden commencement at 0130 UT D_{st} reaches a maximum negative value of 37 γ making it almost directly comparable with the storm of July 9, 1966 for which Frank (1967) has published measurements of the distribution of ring current protons. They are probably very close to the distributions that existed at the time of the flight of rocket 18.15. At apogee the rocket was at an L value of approximately 6. Allowing for magnetospheric inflation which was nearly the same in both cases, the proton measurements of Frank in the equatorial plane at distances between 6 and 7 R_E (earth radii) should be close to the proton intensities in the tube of force ending at the rocket. According to Frank (1967) the proton intensity at 6 to 7 R_E changes very little during the storm. The increases in trapped particle energy which cause the main phase depression of the magnetic field occur between 3 and 5 R_E. The energy density at 6 to 7 R_E is about 10^{-7} ergs cm^{-3} (Fig. 6.3) which is greater than the equatorial magnetic field energy density at that position.

The volume of an equivalent dipole tube of force with 1 cm^2 cross section at an altitude of 200 kms is 1.4×10^{12} cm^3 (Hanson and Ortenbenger 1961) so that if the energy density is constant throughout the tube there are 140,000 ergs of proton energy trapped in the tube. The trapped electron energy in the tube is about 56,000 ergs. Assuming an

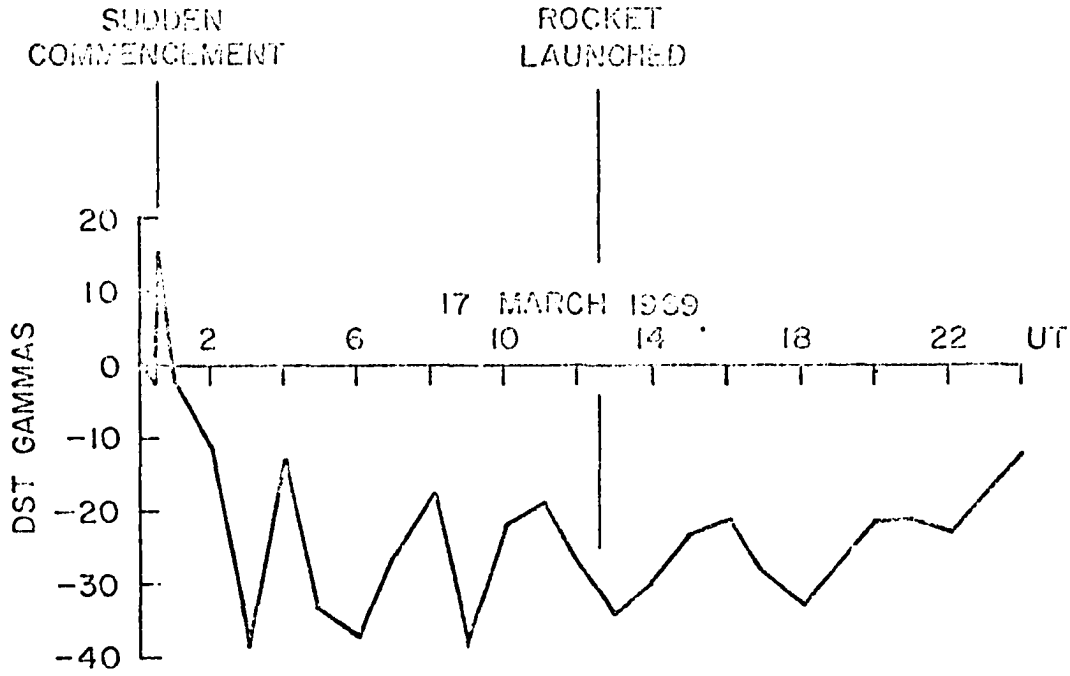

Figure 6.2 The equatorial disturbance in the horizontal component of the Earth's magnetic field, D_{st}, during the magnetic storm beginning at 0030 U.T. March 17, 1969.

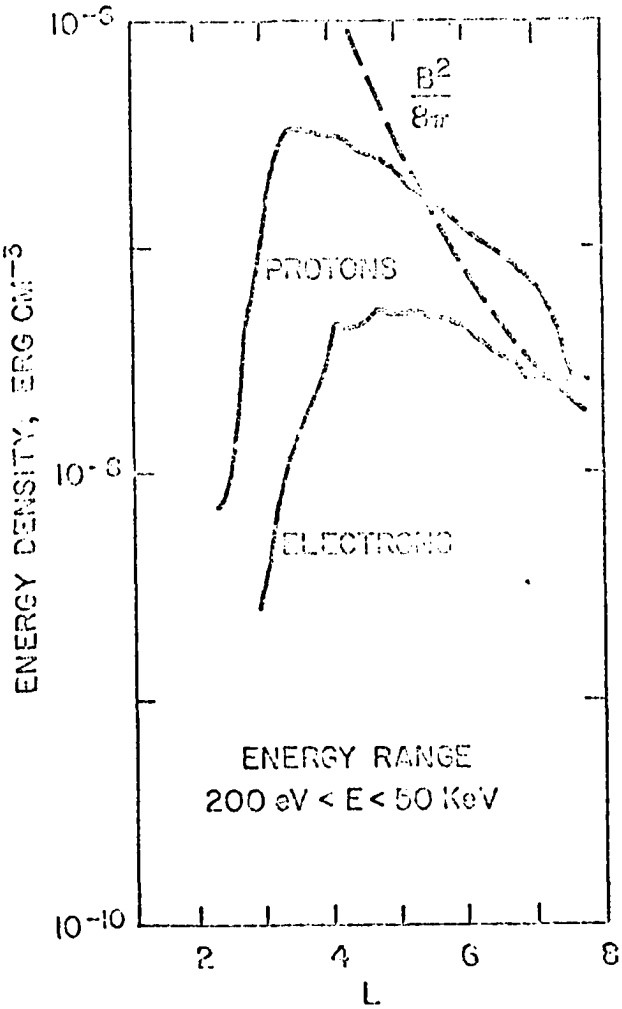

Figure 6.3 The energy density of trapped electrons and protons in the equatorial region during the magnetic sotrm of July 9, 1966. (Frank 1967)

average precipitated energy flux of 10 ergs $cm^{-2}sec^{-1}$ for protons and electrons at each end of the tube 72,000 ergs was lost from the tube during the substorm. Only one tenth of this energy is precipitated as protons. The evidence from Frank's observations is that the intensities in the ring current at 6 R_E change little during the magnetic storm. The conclusion is that there must be a significant injection of particle energy into the tube of force during the substorm, to replace the precipitated energy mostly precipitated as electrons.

CHAPTER 7

SUMMARY AND DISCUSSION

7.1 Summary of Results

7.1.1 The primary proton beam. The primary proton beam has an energy spectrum of the form AE^{-r} with r varying from 2.1 to 2.9. Near apogee the exponent averages 2.4 but it varies from 2.1 to 2.5. At lower altitudes r increases to 2.9, implying that the spectral intensity above 30 kev decreases more rapidly.

The pitch angle distribution is "flat" in the sense that directions near 90° have the highest intensities. If fitted by a $\sin^m \alpha$ form m lies between 3 and 5 for protons less than 13 kev and between 2 and 4 for protons 13 kev < E < 30 kev.

The proton energy flux has a lower limit ranging from 0.6 to 0.7 ergs cm^{-2} sec^{-1}.

7.1.2 Time variations. On a number of occasions in the flight the spectrum softens, in one case r goes from 2.1 to 2.5, and the flux increases for a short period. The changes are correlated with changes in the electron flux. The electron spectrum hardens and the flux increases. There is no time dispersion between different energies or between protons and electrons. If the change is temporal the source must be within 2500 kms. If the change is due to spatial structure its scale size is 2 kms which is much less than the minimum scale size calculated to be 30 kms.

7.1.3 Pitch angle variations. The variation of the pitch angle distribution with height is consistent with increased absorption

of protons near 90° above an altitude of 190 kms. Below this altitude the pitch angle distribution tends to isotropy, probably as a result of strong scattering.

7.1.4 Other measurements. The only measurements of proton spectra below 10 kev in post breakup aurora are those of Bernstein et al. (1969) and Reasoner et al. (1968), all made at Fort Churchill in Canada at L = 8. Bernstein et al. (1969) launched their rocket into the recovery phase of a negative bay with a maximum depression in the horizontal component of the Earth's field of 140 gamma. The proton spectrum, measured at small pitch angles, was power law in form with an exponent r = 3.2 $\pm$ 0.2. The intensities were of the order of 10^8 protons cm^{-2} $ster^{-1}$ kev^{-1} sec^{-1}, and the H beta emission was 300 Rayleighs. It is interesting to note that the proton precipitation in this event was more intense, although the substorm was smaller than the one reported here.

Reasoner et al (1968) observed a relatively flat spectrum between 2 kev and 20 kev but the intensities increased rapidly at lower energies and decreased at higher energies. The measurements of both Bernstein et al. and Reasoner et al show significant fluxes below 2 kev.

7.2 Effects of Pitch Angle Scattering

In calculations of the interaction of a proton beam with the atmosphere it has always been assumed that no pitch angle scattering occurs. Eather (1966) has argued based on wave mechanics that the scattering angle in a single collision will be less than 0.2°. The measurements reported here, and the laboratory measurements of Wax and Bernstein (1967) show clearly that the root mean square scattering angle is greater. In the atmosphere scattering apparently becomes important below 190 kms where the

pitch angle distribution tends to isotropy. This affects calculations of the profile of the H beta emission line (Eather 1966, Veissberg 1966) and the height profile of the H beta emission (Eather and Burrows 1966). Many of the protons are scattered back up the line of force causing a red shift in the line profile of the H beta emission observed in the zenith. The scattering observed during this flight is quite adequate to account for the observed red shifts. Veissberg (1966) commented that his data indicated strong scattering for low energy protons but he could not confirm it. The total effect of the scattering on hydrogen line profiles may be summarized as follows. Whatever the primary pitch angle distribution the profiles will be dominated by the isotropic intensity below 160 kms where most of the energy is lost. Above 190 kms the profile will consist primarily of emission from protons with pitch angles close to 90°. The integrated profile observed at the ground will be a mixture of the two with the lower height range dominating. The height dependence of the line profile will affect measurements of the height profile from a rocket which are usually made (Murcray 1966, Miller and Shepherd 1969, Wax and Bernstein 1970) with a photomultiplier and narrow interference filter. Since the passband is not wide enough to include all the H beta emission a correction based on an assumed line profile is necessary to obtain the total emission. Using a profile independent of altitude may introduce significant errors into the height profile.

Calculations of the height profile of the H beta emission are also affected because the amount of atmosphere traversed by a proton cannot be calculated simply if it is scattered. The calculations may have to be done by a Monte Carlo method as has been done for electrons (Maeda 1965).

7.3 Precipitation Mechanism

One of the questions to be answered in auroral physics is: what makes electrons and protons precipitate into the atmosphere? If they were originally in a trapped orbit, why did they become untrapped and, if they were not, where do they come from and what made them appear in the atmosphere? The features of the precipitated flux, electron and proton, give some clues about the mechanism causing the precipitation. For example, a "flat" pitch angle distribution near the atmosphere is the signature of "weak" pitch angle diffusion (Kennel and Petschek 1966). The diffusion is caused by an interaction between particles and waves and is called "weak" because the precipitation rate is controlled by the wave intensity. The waves may be generated by an instability which depends on pitch angle anisotropy caused by the existence of a loss cone in the pitch angle distribution due to atmospheric absorption. The opposite limit of "strong" diffusion occurs when the wave intensity is strong enough to maintain isotropy in the loss-cone. Then the precipitation is controlled by the size of the loss-cone. In this section the features of the particle precipitation are compared with a particular wave-particle interaction mechanism generated by loss-cone anisotropy which has been described by Swift (1968). The anisotropy in the ring current protons generates a convective electrostatic wave with the real part of the dispersion relation, the propagation characteristics, determined by the "cold" ionospheric background plasma. The phase velocity is close to the speed of the ring current protons and very nearly perpendicular to the magnetic field. As a result the phase velocity parallel to the magnetic field is very much greater, comparable with the parallel velocity of auroral electrons. The

wave frequency is much less than the electron gyrofrequency so that the electrons can only respond to the wave by moving parallel to the magnetic field or by drifting perpendicular to the magnetic field with velocity $|\bar{V}|=|\bar{E}x\bar{B}|$. If the electron velocity parallel to the field is close to the parallel wave phase velocity it can resonate with the wave and be accelerated by it. The group velocity of the wave is nearly parallel to the field and as the wave propagates downwards into "cold" plasma of increasing density the phase normal becomes more nearly perpendicular to the magnetic field, and the parallel phase velocity increases correspondingly. The particle once in resonance with the wave may stay in resonance for a considerable distance and be accelerated by an amount many times greater than would be expected from the electric field amplitude of the wave (Gary, Montgomery and Swift 1968). The amount of acceleration depends on the phase at which the particle encounters the wave and the coherence of the wave (Swift 1970). The growth rate of the wave depends on the pitch angle anisotropy of the protons and is greatest just above the atmosphere where their loss-cone is greatest. The energy acquired by the electrons comes from the protons. The effect on the protons is to increase the pitch angle diffusion. The precipitated flux will have the following features. The electron flux will increase when the proton flux increases. There is an energy below which there is no effect on the electron flux because a minimum parallel energy is needed for resonance. The proton pitch angle distribution is flat and little time dispersion between particles of different velocities would be observed at auroral altitudes. However, the actual time dispersion in this case would have little significance because the particles interact with the wave over a distance comparable with the distance to the observation point.

These features are all observed in the precipitated flux reported here. Many important questions about the mechanism cannot be answered yet. For example, it is of great interest to know the relation between the electron and proton precipitated energy flux. In the observed event much more energy is precipitated by the electrons than the protons. Questions such as this require a non-linear analysis of the mechanism. The answers are needed before a definite identification of the mechanism is made. When operating, the mechanism apparently provides an efficient means for converting trapped proton energy into precipitated electron energy. An increase of 10% to 20% in the precipitated proton energy doubles the precipitated electron energy.

It should be noted that other wave-particle interactions were taking place at the same time and may have contributed to the precipitation. There are many periodic variations in the electron flux, often seen in only one energy channel at a time. In most cases the effect on the total precipitation seems to be small. It is clear that the plasma from which the particles come is highly disturbed with a wide spectrum of waves propagating through it.

7.4 Relationship between Proton Precipitation and the Ring Current

In recent investigations of the ring current a number of interesting morphological features have been revealed.

1. The ring current energy increases during a substorm (Davis and Parthasarathy 1967, Davis 1969, Akasofu 1969). The increase is also apparent in the variation of D_{st} on March 17th.

2. The ring current increases asymmetrically with the greatest injected proton intensities being observed in the evening-midnight sector (Frank 1970).

3. Most of the increase in the trapped proton fluxes is observed at L = 3 to 5. The proton intensity at L = 6 to 7 remains close to the level it has in quiet times (Frank 1967).

4. The ring current has a sharp inner boundary which coincides with the plasmapause (Frank 1967, Russell and Thorne 1970).

5. The spectrum of ring current protons is relatively flat from 5-50 kev and is independent of L (Fig. 7.1 Frank 1967).

When these results are combined with the measurements made by the rocket the following picture of the process develops.

Since the proton intensity is relatively constant at 6 to 7 R_E during quiet and active periods, and the energy density of the protons exceeds the equatorial magnetic energy density of the Earth's field (Fig. 6.3), it seems that the protons have reached the limit of stable trapping described by Kennel and Petschek (1966). Any further injection of energy into the proton distribution leads directly to precipitation and also possibly diffusion inwards. The spectrum of the trapped particles is flat over a wide energy range contrasting strongly with the precipitated proton spectrum which has the greatest intensities at low energies. The trapped spectrum is characteristic of the limiting mechanism and the precipitated spectrum may be characteristic of the injection mechanism. However, because some of the precipitated electron energy comes from the proton energy injection, the later need not be true. Protons are injected into the ring current during a substorm (item 1 above) and proton injection is occurring in the auroral substorm region. This leads to the hypothesis that the proton injection is linked spatially as well as temporally with the auroral substorm. The scanning photometer data (Fig. 6.1) shows then

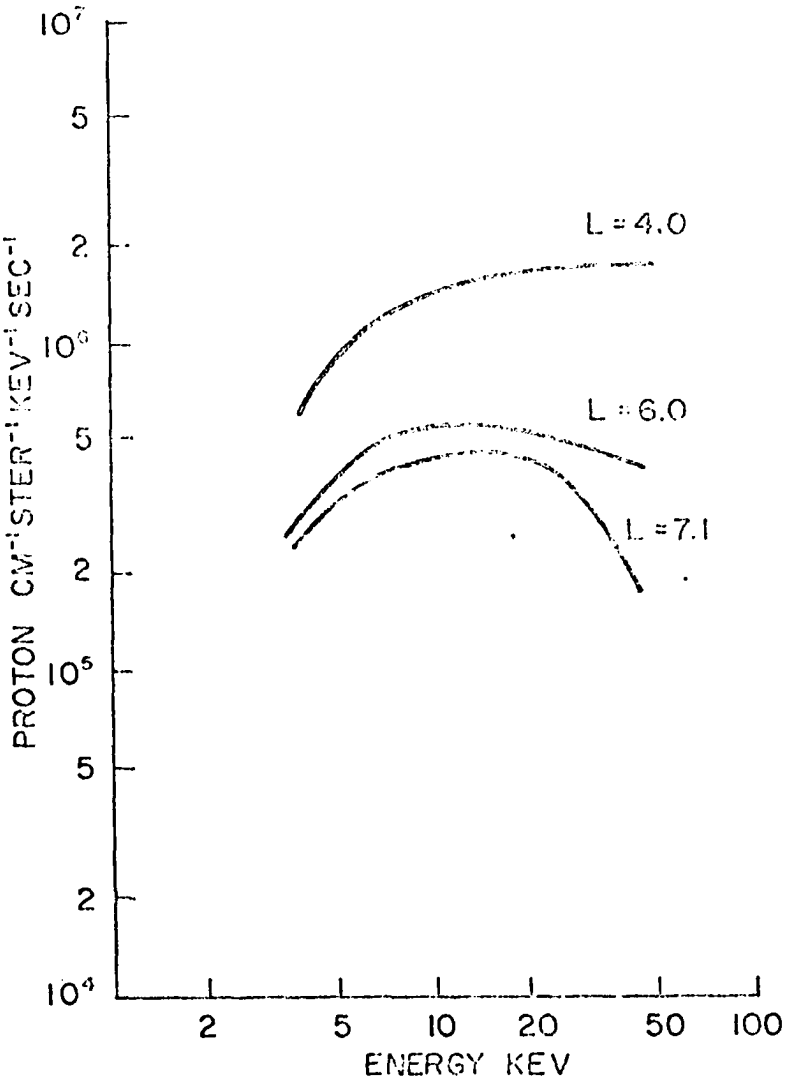

Figure 7.1 The energy spectrum of protons in the equatorial region during a magnetic storm on July 9, 1966 at three different radial distances. (Frank 1967)

that the injection is occurring over a wide range of L values; from L = 4 to L = 8 at least. At the lower L values the intensity can build up, increasing $|D_{st}|$, because the trapping limit has not been reached. The protons drift under the influence of the magnetic field gradients from where injection occurs in the midnight sector towards the evening sector causing the asymmetric portion of the ring current. Simultaneously they diffuse inward and as they cross the plasma pause, Cornwall et al. (1970) point out, the growth rate of ion cyclotron turbulence in the protons increases. They rapidly diffuse into the loss cone and are precipitated into the atmosphere.

It is not clear how the injected energy is split between protons and electrons. If it is mainly in the protons then some mechanism such as that described by Swift (1968) is necessary to extract energy from the protons to precipitate electrons. If it is split equally then the proton energy is trapped more efficiently.

The mystery in the process is the injection mechanism. To suggest that it is intimately connected with the auroral substorm does little to help because it is also a mystery.

7.5 Further Investigations

A number of further investigations are suggested by these results. The observations reported here were exploratory in nature and can be improved considerably now the important parameters are known.

1. The interaction between the proton beam and the atmosphere needs measuring. This involves making measurements of the neutral hydrogen spectrum, the proton spectrum and pitch angle distribution as a function

of height up to at least 400 kms preferably in prebreakup proton aurora which presumably is less active.

2. Some effort should be devoted to recalculation of line profiles of H beta taking into account pitch angle scattering.

3. Accurate measurements of the electron and proton spectra and pitch angle distribution well above atmospheric effects are required to compare with the theoretical precipitation mechanisms.

4. The non-linear aspects of the precipitation mechanism need investigation to obtain the relation between the spectra and pitch angle distributions of the precipitated particles and the energy fluxes of protons and electrons.

LIST OF SYMBOLS AND ABBREVIATIONS

This is not a complete list of all symbols used in the dissertation. Where a symbol has been used only once, and is defined at that place it has not been included in the list.

A - coefficient of differential energy spectrum

B - magnetic field strength

cms - centimeters

cps - counts per sec

D - atmospheric depth

D_{st} - Storm time magnetic disturbance field

E - particle kinetic energy

E_o - kinetic energy of particle in circular orbit in the cylindrical analyser.

E^1 - proton primary energy

E_1 - exponentional spectrum parameter

ev - electron volts

$F_{i\infty}$ - equilibrium fraction of particles in charge state i where i = 1 for protons, 0 for atoms and $\bar{1}$ for negative ions

g(E) - geometric factor of cylindrical analyser

h - optical transmission of wire mesh

Hβ - hydrogen emission line at 4861Å

Hg - mercury

Hz - Herz - one cycle per second

k - coefficient in range energy relation

LIST OF SYMBOLS AND ABBREVIATIONS

(Cont'd)

kev - kilo-electron volts

kms - kilometers

L - atmospheric scale height

L - parameter labelling a magnetic field shell in the magnetosphere Approximately the geocentric distance at which the shell crosses the equator.

m - ratio of cross-sections σ_{10}/σ_{01}

mm - millimeter

mv - milli volts

msec - milliseconds

n - exponent in range-energy relation

n - length in units of scale height

pf - picofarad

r - exponent in power law spectrum

RC - resistance - capacitance

Re - earth radius (unit of distance)

secs - seconds

standard cms - unit of atmospheric depth equivalent to 1 cm in the gas at 1 mm Hg pressure and 15° C

T+ - time since launch of the rocket

UT - Universal time

V - volts

Å - Angstroms

LIST OF SYMBOLS AND ABBREVIATIONS

(Cont'd)

°C - degrees Celsius

α - pitch angle

γ - 10^{-5} gauss (magnetic field strength)

ϵ - channel multiplier efficiency

λ_i - mean free path at zero altitude for particles in charge state i

σ_{ji} - the cross section of charge changing collisions from charge state j to state i

REFERENCES

Adams, J. and B. W. Manley, The mechanism of channel electron multiplication, IEEE Trans. Nucl. Sci. NS-13, 88-99, 1966.

Akasofu, S. I., Magnetospheric substorm, Atmospheric Emissions, Proceedings of NATO Adv. Study Inst. Norway 1968, 267-284, Van Nostrand Reinhold 1969.

Akasofu, S.-I., R. H. Eather and J. N. Bradbury, The absence of the hydrogen emission (H_β) in the westward traveling surge, Planet. Sci. 17, 1409-1412, 1969.

Allison, S. K., Experimental results on charge-changing collisions of hydrogen and helium atoms and ions at kinetic energies above 0.2 kev. Rev. Mod. Phys. 30, 1137-1168, 1958.

Anderson, A. D. and W. E. Francis, The variation of the neutral atmospheric properties with local time and solar activity from 100 to 10,000 km. J. Atmospheric Sci. 23, 110-124, 1966.

Bernstein, W., G. T. Inouye, N. L. Sanders and R. L. Wax, Measurements of precipitated 1-20 kev protons and electrons during a breakup aurora, J. Geophys. Res. 74, 3601-3608, 1969.

Bosqued, J. M., Etude d'un multiplicateur d'electrons sans fenetre, D.S. thesis University of Toulouse, June 1967.

Bryant, D. A. and A. D. Johnstone, Gain of a channel multiplier, Rev. Sci. Inst. 36, 1662, 1965.

Burrous, C. N., A. J. Leiber and V. T. Caviantseff, Detection efficiency of a continuous channel electron multiplier for positive ions, Rev. Sci. Inst. 38, 1477-1481, 1967.

Chamberlain, J. W., Theories of the aurora, Advances in Geophysics, 4, 109-215, 1958.

Chase, L. M., Spectral measurements of auroral zone particles, J. Geophys. Res. 73, 3469-3476, 1968.

Cooke, C. J., E. Jones, and T. Jorgensen, Range-energy relations of 10-250 kev protons and helium ions in various gases, Phys. Rev. 91, 1417-1422, 1953.

Cornwall, J. M., F. V. Coroniti and R. M. Thorne, Turbulent loss of ring current protons, to be published, 1970.

Dalgarno, A., I. D. Latimer and J. W. McConkey, Corpuscular bombardment and N_2^+ radiation, Planet. Space. Sci. 13, 1008-1009, 1965.

Davidson, G. T., Expected spatial distribution of low energy protons precipitated in the auroral zone, J. Geophys. Res. 70, 1061-1068, 1965.

Davis, L. R., O. E. Berg and L. H. Meredith, Direct measurements of particle fluxes in and near auroras, Space Research I, p. 721, North-Holland Amsterdam, 1960.

Davis, T. N., Temporal behavior of energy injection into the geomagnetic ring current, J. Geophys. Res. 74, 6266-6274, 1969.

Davis, T. N. and R. Parthasarathy, The relationship between polar magnetic activity, DP and growth of the geomagnetic ring current, J. Geophys. Res. 72, 5825-5836, 1967.

Eather, R. H., The red shift of auroral hydrogen line profiles, J. Geophys. Res. 71, 5027-5032, 1966.

Eather, R. H., Auroral proton precipitation and hydrogen emissions, Rev. Geophys. 5, 207-285, 1967.

Eather, R. H. and K. M. Burrows, Excitation and ionization by auroral protons, Aust. J. Phys. 19, 309-322, 1966.

Egidi, A, R. Marconero, G. Pizzella and F. Sperli, Channeltron fatigue and efficiency for protons and electrons, Rev. Sci. Inst. 40, 88-91, 1969.

Evans, D. S., Low energy particle detection using the continuous channel electron multiplier, Rev. Sci. Inst. 36, 375-382, 1965.

Evans, J. E., E. G. Joki, R. G. Johnson and R. D. Sharp, Austral and boreal auroral zone precipitation patterns for low energy protons. Space Research VI, p.773, North Holland Amsterdam, 1966.

Frank, L. A., Low energy proton and electron experiment for the orbiting geophysical observatories B and E, U. of Iowa report 65-22, July 1965.

Frank, L. A., On the extra-terrestrial ring current during geomagnetic storms, J. Geophys. Res. 72, 3753-3767, 1967.

Frank, L. A., Direct detection of the asymmetric injection of extra-terrestrial ring current protons into the outer radiation zone, J. Geophys. Res. 75, 1263-1268, 1970.

Frank, L. A., N. K. Henderson and R. L. Swisher, Degradation of continuous channel electron multipliers in a laboratory operating environment, Rev. Sci. Inst. 40, 685-689, 1969.

Gartlein, C. W., Auroral spectra showing broad hydrogen lines, Trans. Am. Geophys. Union, 31, 18-20, 1950.

Gary, S. P., D. C. Montgomery and D. W. Swift, Particle acceleration by electrostatic waves with spatially varying phase velocities, J. Geophys. Res. 73, 7524 - 7525, 1968.

Hallinan, T. J. and T. N. Davis, Small scale auroral distortions, to be published, 1970.

Handbook of Geophysics for Air Force Designers, U.S.A.F. 1957.

Hanson, W. B., I. B. Ortenburger, Coupling between the protonosphere and normal F. region, J. Geophys. Res. 66, 1425-1435, 1961.

Johnstone, A. D., The geometric factor of a cylindrical plate electrostati energy analyzer, to be published, 1970.

Kennel, C. F. and H. E. Petschek, Limit on stably trapped particle fluxes, J. Geophys. Res. 71, 1-28, 1966.

Klettke, B. D., N. D. Krym, and W. G. Wolber, Long term stability characterestics of commonly used channel electron multipliers, IEEE Trans. Nucl. Sci. NS-17, 72-80, 1970.

Maeda, K., Diffusion of auroral electrons in the atmosphere, NASA TN D-2612, February 1965.

McIlwain, C. E., Direct measurement of particles producing visible auroras, J. Geophys. Res. 65, 2727-2747, 1960.

Meinel, A. B., Doppler-shifted auroral hydrogen emission, Astrophys. J. 113, 50-54, 1951.

Miller, J. R. and G. G. Shepherd, Rocket measurements of H-beta production in a hydrogen aurora, J. Geophys. Res. 74, 4987-4997, 1969.

Montbriand, L. E., Morphology of auroral hydrogen emissions during auroral substorms. Ph.D. Thesis, University of Saskatchewan.

Mozer, F. S. and P. Bruston, Observation of the low altitude acceleration of auroral protons, J. Geophys. Res. 71, 2201-2206, 1966.

Murcray, W. B., An observation of the height luminosity distribution of auroral H_β emission, J. Atmospheric, Terrest. Phys. 28, 812-814, 1966.

Reasoner, D. L., R. H. Eather, B. J. O'Brien, Detection of alpha particles in auroral phenomena, J. Geophys. Res. 73, 4185-4198, 1968.

Reed, R. D., E. G. Shelley, J. C. Bakke, T. C. Sanders and J. D. McDaniel, A low energy channel multiplier spectrometer for ATS-E, IEEE Trans. Nucl. Sci. NS-16, 359-370, 1969.

Russell, C. R. and R. M. Thorne, On the structure of the inner magnetosphere to be published in Cosmic Electrodynamics, 1970.

Schmidt, K. C. and C. F. Hendee, IEEE Trans. Nucl. Sci. NS-13, 100-111, 1966, Continuous channel electron multiplier operated in the pulse saturated mode.

Sckopke, N., General relation between the energy of trapped particles and the disturbance field near the earth, J. Geophys. Res. 71, 3125-3130, 1966.

Sharber, J. R., J. D. Winningham and W. R. Sheldon, A directional low energy electron detector employing channel electron multipliers, IEEE Trans. Nucl. Sci. NS-15, 536-540.

Shea, M. F., G. B. Shook, J. B. Reagan, L. F. Smith and T. C. Sanders, Channel multiplier instrumentation for the measurement of low energy auroral particles, IEEE Trans. Nucl. Sci. NS-14, 96-102.

Soraas, F. and B. Trumpy, Rocket measurements of proton energy spectra and pitch angle distributions in the auroral zone, J. Atmospheric Terrest. Phys. 28, 1081-1092, 1966.

Swift, D. W., A new interpretation of VLF Chorus, J. Geophys. Res 73, 7447-7456, 1968.

Swift, D. W., Particle acceleration by electrostatic waves, to be published in J. Geophys. Res. 1970.

Tatry, B., J. M. Bosqued, and H. Reme, Characteristics of electron multipliers used as detectors for low energy protons, Nucl. Inst. and Methods, 69, 254-260, 1969.

Thiokol Chemical Corporation, NASA Nike Tomahawk Handbook.

U.S. Standard Atmospnere, 1962, U.S. Gov't. Printing Office.

Veissberg, O. L., Pitch angle distribution of auroral protons, Geomagnetism and Aeronomy, 6, 101-103, 1966.

Wax, R. L. and W. Bernstein, Energy independent detector for total hydrogen fluxes in the range 1-10 kev for space and laboratory applications, Rev. Sci. Inst. 38, 1612-1615, 1967.

Wax, R. L. and W. Bernstein, Rocket-borne measurements of H_β emissions and energetic hydrogen fluxes during and auroral breakup. J. Geophys. Res. 75, 783-787, 1970.

Whalen, B. A. and I. B. McDiarmid, Summary of rocket measurements of auroral particle precipitation in Atmospheric Emissions - Proceedings of NATO Adv. Study Inst. Norway 1968, 93-106, VanNostrand Reinhold, 1969.

Whalen, B. A., I. B. McDiarmid and E. E. Budzinski, Rocket measurements in proton aurora, Can. J. Phys. 45, 3247-3255, 1967.

Wolber, W. G., B. D. Klettke, J. S. Miller and K. C. Schmidt, Pulse pair resolution in a pulse-saturated channeltron electron multiplier, Appl. Phys. Lett. 15, 47-48, 1969.